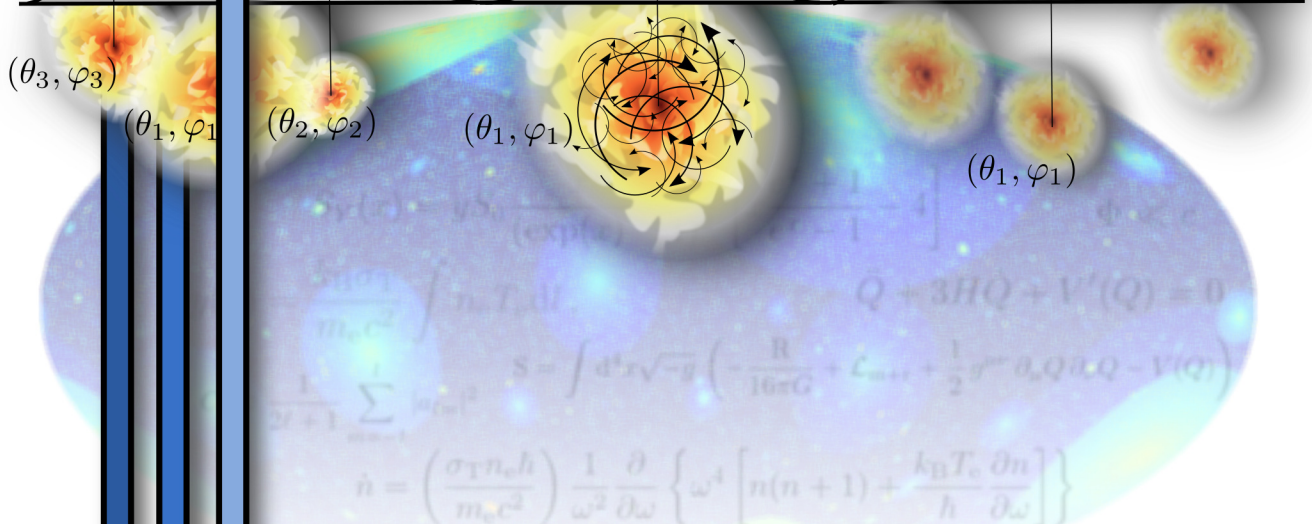
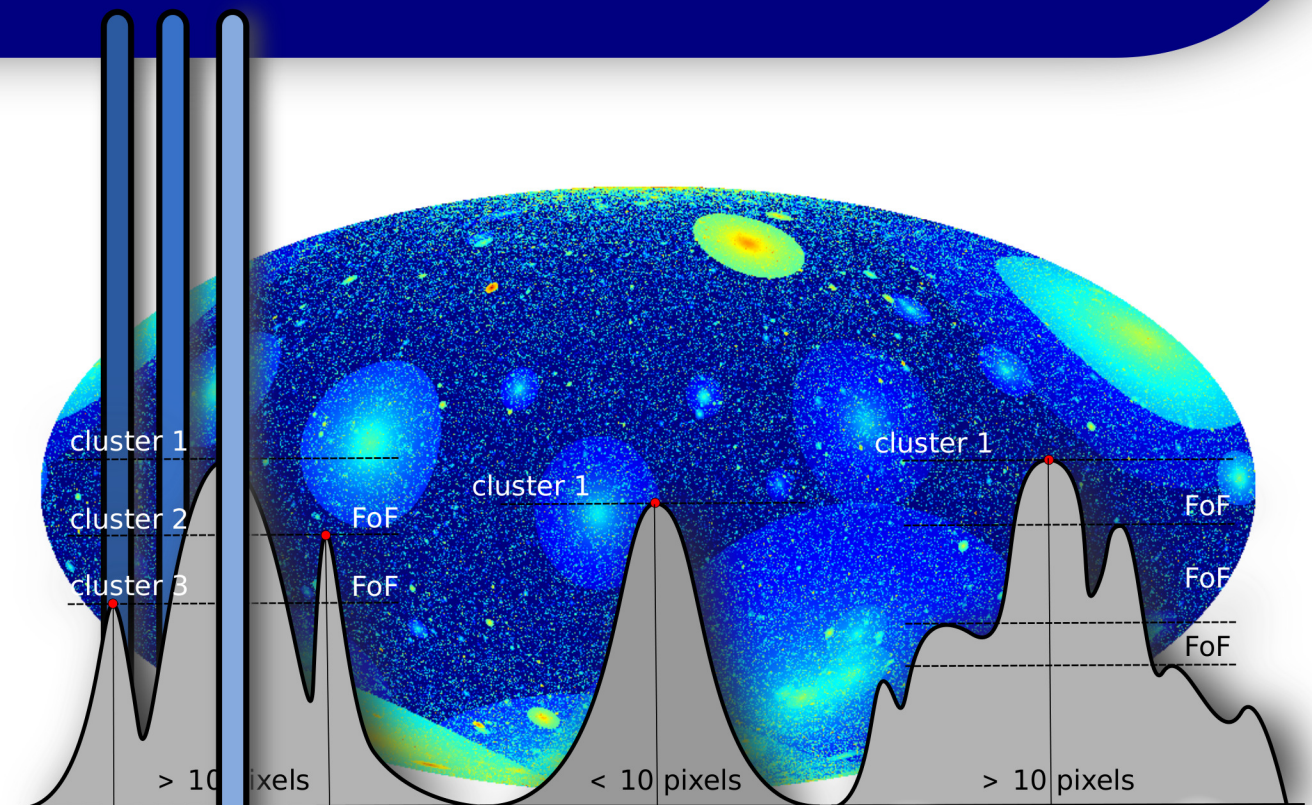


On finding galaxy clusters with *PLANCK* and the spherical collapse model in different Dark Energy cosmologies



Dissertation
submitted to the
Combined Faculties for the Natural Sciences and for
Mathematics
of the Ruperto-Carola University of Heidelberg, Germany
for the degree of
Doctor of Natural Sciences

Put forward by
Jean-Claude Waizmann
born in: Mannheim, Germany
Oral examination: November 24, 2010

**ON FINDING GALAXY CLUSTERS WITH *PLANCK*
AND
THE SPHERICAL COLLAPSE MODEL
IN
DARK ENERGY COSMOLOGIES**

**Referees: Prof. Dr. Matthias Bartelmann
Prof. Dr. Luca Amendola**

Über das Detektieren von Galaxienhaufen mit *PLANCK* und das sphärische Kollapsmodell in Modellen mit Dunkler Energie

Zusammenfassung: Eines der Hauptziele der *PLANCK* Mission ist die Durchführung einer Himmelsdurchmusterung von Galaxienhaufen mittels des Sunyaev-Zel'dovich (SZ) Effektes, was unmittelbar die Frage aufwirft, inwiefern eine solche Durchmusterung sensitiv für verschiedene kosmologische Modelle wäre. Um diese Frage zu beantworten habe ich eine schnelle semi-analytische Methode entwickelt um Himmelskarten des Compton- y Parameters für beliebige Kosmologien zu erstellen, die sofort in die *PLANCK* Simulations Pipeline eingefügt werden können. Zusätzlich habe ich Filter- und Detektionsmodule implementiert, die es erlauben den zu erwartenden Haufenkatalog zu charakterisieren. Dabei trat zu Tage, dass für realistische Fälle ein solcher Katalog für geringe Kontaminationsraten nur etwa ~ 1000 Haufen umfasst, wesentlich weniger als ursprünglich bei der Projektierung der Mission erwartet worden war.

Aufgrund fehlerbehafteter Vorhersagen des Effektes von Modellen mit früher dunkler Energie auf die kosmische Strukturbildung, haben wir sphärische Kollapsmodelle für verschiedene Kosmologien untersucht. Mit dem Ergebnis, dass Modelle mit zeitabhängiger Zustandsgleichung nur einen vernachlässigbaren Einfluss auf die Strukturbildung haben. Dennoch können solche Modelle wegen ihrer unterschiedlichen Expansionsgeschichte mittels des Volumeneffektes, z.B. durch Abzählen von Haufen in einem festen Volumen, unterschieden werden. Ferner stellte sich heraus, dass das Winkelleistungsspektrum des SZ-Effektes sich ebenfalls hervorragend dazu eignet, alternative kosmologische Modelle auszuschliessen.

On finding galaxy clusters with *PLANCK* and the spherical collapse model in dark energy cosmologies

Abstract: One of the main objectives of the *PLANCK* mission is to perform a full-sky cluster survey based on the Sunyaev-Zel'dovich (SZ) effect, which leads to the question of how such a survey would be affected by cosmological models with a different history of structure formation than Λ CDM. To answer this question, I developed a fast semi-analytic approach for simulating full-sky maps of the Compton- y parameter, ready to be fed into a realistic simulation pipeline. I also implemented a filter and detection pipeline based on spherical multi-frequency matched filters, that was used to study the expected SZ cluster sample of *PLANCK*. It turned out that realistic samples will comprise 1000 clusters at low rate of contamination, significantly lower than originally anticipated.

Driven by wrong estimates of the impact of early dark energy models on structure formation, we studied the spherical collapse model in dark energy model, finding that models with varying equation-of-state have a negligible impact on the structure formation. Yet, the different expansion history for the different models can be detected via volume effects, when counting objects in a known volume. Furthermore, it turned out that the different expansion history strongly affects the angular SZ power spectra for the various models, making them an interesting tool to distinguish and constrain alternative cosmologies.

”Twenty years from now you will be more disappointed by the things that you didn’t do than by the ones you did do. So throw off the bowlines. Sail away from the safe harbor. Catch the trade winds in your sails. Explore. Dream. Discover.”

Mark Twain (1835-1910)

Contents

Abstract	i
Table of contents	v
List of figures	vii
List of tables	xi
Introduction	1
1 Cosmology and cosmic structure formation	3
1.1 Friedmann-Lemaître-Walker cosmology	3
1.1.1 The cosmological principle	3
1.1.2 Understanding the cosmo-dynamics	4
1.1.3 Cosmic distances	7
1.1.4 Horizon size	8
1.2 Structure formation	8
1.2.1 General remarks	8
1.2.2 Linear growth	10
1.2.3 Suppression of growth	10
1.2.4 The power spectrum	11
1.3 Cosmic microwave background	13
1.3.1 Overview	13
1.3.2 Statistical description	14
2 Galaxy clusters	17
2.1 Formation and abundance	17
2.1.1 Spherical collapse	17
2.1.2 Halo density profiles	19
2.1.3 The mass function	20
2.2 Observational properties of galaxy clusters	21
2.2.1 Optical	22
2.2.2 X-rays	23
2.2.3 Microwaves	26
3 The zoo - Cosmological models	31
3.1 Λ CDM - The cosmological standard model	31
3.2 Quintessence models	32
3.2.1 Classification of the used models	33
3.2.2 Parametrisation of the models	34
3.2.3 Early dark energy models	36
3.3 Chaplygin gas and Casimir effect	38
3.4 Phantom models and topological defects	40

Contents

4	The <i>PLANCK</i> mission	41
4.1	Introduction	41
4.2	Mission objectives	42
4.3	The instrument	43
5	Semi-analytic mapmaking of full-sky SZ maps for <i>PLANCK</i>	47
5.1	The general idea	47
5.2	Mass & redshift distribution of the cluster sample	47
5.3	Modelling the SZ signal of the individual clusters	48
5.4	How to tessellate a sphere - HEALPix	51
5.5	Placing the clusters on the sky	52
6	Simulating <i>PLANCK</i> observations	57
6.1	Foreground components - Galactic emission	57
6.1.1	Galactic dust emission	58
6.1.2	Galactic synchrotron emission	59
6.1.3	Galactic free-free emission	60
6.2	Foreground components - extra-Galactic emission	61
6.2.1	Infra-red galaxies	62
6.2.2	Radio point sources	62
6.3	Instrumental effects	62
6.3.1	Instrumental beams	62
6.3.2	Instrumental noise	63
6.3.3	Impact of scan strategy	63
6.3.4	$1/f$ -noise	64
6.3.5	Exposure	64
6.4	The simulation pipeline	64
7	Studying SZ cluster with <i>PLANCK</i>	69
7.1	Introducing multi-frequency filtering on spherical domains	69
7.1.1	Filtering - the general idea	69
7.1.2	Filtering - mathematical description	70
7.2	Finding clusters in the filtered maps	74
7.3	The impact of foregrounds on the filter performance	76
7.3.1	Number of detections, contamination and completeness	76
7.3.2	Spatial distribution of the detections	79
7.3.3	The selection function	81
7.3.4	The physical properties of the detected cluster sample	84
7.4	Perspectives	85
8	Spherical collapse in DE cosmologies	89
8.1	Newtonian hydrodynamics of a relativistic fluid	89
8.2	Spherical collapse - Linear vs. non-linear evolution	92
8.3	Results for the collapse parameters	94

8.4	Volume effects	96
8.5	Conclusions	98
9	SZ power spectra in dark energy cosmologies	101
9.1	Computing the SZ angular power spectrum	101
9.2	Choice of the 3D Compton- y radial profile	102
9.3	Predictions for the angular SZ power spectra in DE cosmologies .	103
9.4	Expansion history vs. structure formation	105
10	Conclusions	109
A	Studying the SZ cluster sample for a hypothetical cosmology	113
A.1	Studying the impact on <i>PLANCK</i> 's cluster sample	113
A.2	Impact of noise levels to the filter performance	118
A.3	Constraining EDE parameters with cluster counts	118
A.3.1	Fisher analysis	118
A.3.2	Results	120
	Acknowledgements	123
	Bibliography	125
	Index	133

List of Figures

1.1	Evolution of the different density parameters	5
1.2	The Mészáros effect	11
1.3	CMB power spectrum and the dominant physical effects	13
1.4	Scheme of the CMB	15
2.1	Spherical collapse, schematic drawing	18
2.2	Differential comoving mass function	21
2.3	Optical image of Abell 2218	22
2.4	Emission of Bremsstrahlung in galaxy clusters	24
2.5	Frequency dependence of the SZ effect	26
2.6	The thermal SZ-effect	28
3.1	Schematic for a scalar field slowly rolling down the potential	32
3.2	Time evolution of the equation-of-state parameter	35
3.3	Properties of the considered EDE cosmologies	36
3.4	Time evolution of the equation-of-state parameter	38
4.1	Artists impression of the <i>PLANCK</i> satellite	41
4.2	<i>PLANCK</i> 's first one-year all-sky map	42
4.3	Frequency dependence of the SZ effect	44
5.1	Flowchart for the creation of full-sky Compton- γ maps	49
5.2	Redshift evolution of the cluster properties	50
5.3	HEALPix tessellation scheme	51
5.4	Cluster angular power spectrum assuming top-hat window function	53
5.5	Distribution of clusters among the HEALPix pixels	54
5.6	Simulated full-sky SZ-map for the EDE 4 model	55
6.1	Spectra of sources in <i>PLANCK</i> 's frequency range	58
6.2	Sky template map for the Galactic dust emission	59
6.3	Sky template map for the Galactic synchrotron emission	60
6.4	Sky template map for the Galactic free-free emission	61
6.5	Exposure map of the ecliptic North Pole for <i>PLANCK</i>	63
6.6	Flowchart for the <i>PLANCK</i> Level1S pipeline	66
7.1	Flowchart for the cluster detection routines	71
7.2	Comparison of unfiltered with filtered field	72
7.3	Testmap for the development of the <code>clustFind_cxx</code> algorithm	74
7.4	Cluster identification with <code>clustFind_cxx</code>	75
7.5	Limiting survey mass as a function of redshift	76
7.6	Impact of the single foregrounds on the filter performance	79
7.7	Impact of added foregrounds on the filter performance	80
7.8	Effect of long wavelength modes on cluster detectability	81

List of Figures

7.9	Spatial distribution of false detections	82
7.10	Spatial distribution of true detections	83
7.11	Selection functions with respect to redshift z	84
7.12	Selection functions with respect to cluster mass	85
7.13	$M - z$ relation for the detected cluster sample	86
7.14	Relation between Y_{recov} and Y_{input}	86
7.15	$Y - M$ relations for the input and the recovered Y	87
8.1	Linear and non-linear evolution of the overdensity parameter	93
8.2	Time evolution of the linear and virial overdensity	95
8.3	Volume effects on halo number counts	97
9.1	Equation-of-state $w(a)$ for different DE models	103
9.2	SZ power spectra for different DE models	104
9.3	Redshift distribution of the C_ℓ 's for different DE models	105
9.4	Angular diameter distance D_A for different DE models	106
A.1	Number of confirmed detections in bins of S/N	115
A.2	Number of detections in redshift bins for EDE and Λ CDM	117
A.3	SZ angular power spectra and redshift distribution of C_ℓ for EDE	118
A.4	Contamination and completeness as function of the scaled CMB	119
A.5	Parameter degeneracies for <i>PLANCK</i> vs. SPT	120
A.6	Parameter degeneracies for SPT vs. eROSITA	121
A.7	Parameter degeneracies for two planned eROSITA surveys	121

List of Tables

1.1	Cosmological parameters from WMAP5	6
1.2	Strategy for the treatment of perturbations in cosmology	9
3.1	Potentials $V(Q)$ for the different quintessence models	33
3.2	Parameter values for used quintessence models	34
3.3	Key cosmological parameters of the used EDE models	37
4.1	Characteristics of the <i>PLANCK</i> channel design	45
5.1	Properties and angular resolution of HEALPix tessellations	52
A.1	Properties of the simulated maps	113
A.2	Properties of the detected cluster sample for EDE	116

*What is a scientist after all?
It is a curious man looking
through a keyhole, the key-
hole of nature, trying to know
what's going on.*

Jacques Yves Cousteau
(1910-1997)

Introduction

The origins of astronomy, the oldest natural science, date back to the ancient civilisations of Babylonia, Egypt, China, India and the Maya. The celestial objects, observed by these cultures, were interpreted as divinities and their movements as expression of their divine will. On the other hand, the astronomical observations served as well more profane purposes, like establishing a reliable measurement of time and calendars. Remarkable contributions to the astronomical knowledge, initially based on the Babylonian observations and analyses, were made by the ancient Greeks. Some of the ideas formulated by e.g. Thales of Miletus, Aristarchus of Samos, Democritus and Eratosthenes, like the spherical nature of our Earth (including an estimate of Earth's diameter), the heliocentric theory of our Solar System and the infinite extent of our Universe, sound from a nowadays perspective, especially in view of the dark medieval times, as concepts being far ahead their times. Observing celestial objects always means to characterise, classify and compile lists and catalogues. The oldest known catalogue of celestial objects (stars), whose original version is unfortunately lost and is only known because it entered in copy the *Almagest* by Ptolemeaeus, was compiled by Hipparch around 150 BC. This star catalogue, being unmatched in its quality till the sixteenth century, can be considered as the very first astronomical survey. Since then, many surveys have been compiled, of which, especially from the point of view of extra-Galactic objects, the catalogue of nebulae by Charles Messier (1730-1817) should be mentioned.

In modern astronomy, we survey nowadays for a plethora of different celestial objects like stars, extra-Solar planets, galaxies and galaxy clusters, but also for fingerprints of astrophysical processes on cosmic scales, such as the cosmic microwave background and, in the future, primordial gravitational waves. Due to the progress in science and technology, the survey for these different objects in all accessible frequency bands is leading to an historically unmatched knowledge and physical understanding. Nevertheless, it lies in the nature of science that, with its progress, new fields of research open and new questions have to be answered. Whether this development, with regard to the sheer size and complexity of our Universe, will ever stop is highly questionable.

In the last two decades, the interplay of technical progress and astrophysical discoveries revolutionised our current view and understanding of the Universe and created a strong demand and will in the societies to support and fund research with a cosmological scope. In order to address the questions about the nature of our Universe, about its constituents of known and unknown kind like dark matter and dark energy, and its past evolution, many observational probes are already working or are projected for the future. Also the work I conducted during my PhD project falls into this broad picture. From the list of astronomical objects we nowadays survey for, I worked on galaxy clusters and their detectability via the thermal Sunyaev-Zel'dovich (SZ) effect in the framework of the ongoing space-based *PLANCK* mission. Initially, my main objective was to find out if and how this mission could distinguish alternative models of dark energy from the currently

Introduction

favoured Λ CDM cosmology by means of a SZ cluster survey. But in order to answer these questions, one automatically deals with the general detectability of clusters by this mission, that was also extensively studied in the *PLANCK* Cluster Challenge organised by the working group WG 5 of the *PLANCK* collaboration. Furthermore, this research led back to the study of some of the underlying physical models for the formation of galaxy clusters themselves, namely the spherical collapse model in a number of different dark energy models.

In the following lines I briefly summarise the structure of my thesis. First, I introduce the cosmological and astrophysical framework in which the work I conducted is set. Therefore, I start in Chapter 1 with the basics of cosmology and structure formation and a brief recapitulation of the cosmic microwave background. In Chapter 2, I summarise the most relevant theoretical and observational aspects about galaxy clusters. The following chapter, Chapter 3, reviews the different dark energy models used for this work and is followed by a short description of the *PLANCK* mission in Chapter 4. After this prelude, I continue in Chapter 5 to introduce the full-sky SZ map-making technique that I developed. In the subsequent Chapter 6, I present the techniques and requirements for simulating realistic *PLANCK* observations. In Chapter 7, the performance of the filtering and cluster detection and the physical properties of the resulting cluster sample are discussed. The results of the work conducted in collaboration with Francesco Pace about the spherical collapse for different models of dark energy are presented in Chapter 8. In the last Chapter 9, I discuss the impact of different dark energy models on the Sunyaev Zeldovich power spectra. After the conclusions presented in Chapter 10, I added Appendix A summarising the results of my initial work, which was based on erroneous early dark energy models.

Some of the results presented in this thesis have been submitted to a referred journal and accepted for publication¹ :

- Waizmann, J.-C. & Bartelmann, M., *Impact of early dark energy on the Planck SZ cluster sample*, A&A, 2009, 493, 859-870
- Pace, F., Waizmann, J.-C. & Bartelmann, M., *Spherical collapse model in dark energy cosmologies* MNRAS, 2010, 1011

¹The results presented in Chap. 7 and 9 are in preparation for submission to a refereed journal

*In all chaos there is a cosmos,
in all disorder a secret order.*
Carl Gustav Jung (1875-1961)



Cosmology and cosmic structure formation

Within living memory, cosmology, the science of the Universe as a whole and, by extension, humanity's place in it puzzle the mind of men. In a continuous coming and going of ideas, cosmology became in modern times a reputable science based on fundamental physical theories and a plethora of observations. This chapter summarises the key concepts of modern cosmology, as they are relevant for this work, dividing them into three sections of which the first (Sect. 1.1) introduces the Friedmann-Lemaître-Robertson-Walker models (Friedmann 1922, 1924; Lemaître 1927; Robertson 1935; Walker 1937), the second one (Sect. 1.2) presents the theory of the formation of structure in the Universe and the third (Sect.1.3) briefly outlines the cosmic microwave background.

1.1 Friedmann-Lemaître-Walker cosmology

On cosmic length scales, gravity is the dominating force among the four known fundamental interactions, therefore a description of the Universe has to be based on general relativity. In order to treat mathematically the Universe as a whole, simplifying assumptions, also known as the cosmological principle, have to be made.

1.1.1 The cosmological principle

The fundamental postulate of standard cosmology is that the Universe is homogeneous and isotropic:

- When averaged over sufficiently large scales, there exists a mean motion of matter and radiation such that with respect to this motion the observable properties of the Universe are isotropic, i.e. independent of direction.
- All fundamental observers following this mean motion, will observe the same cosmic history and measure the same averaged observables. Thus any position in the Universe is by no means preferred to any other.

The cosmological principle with its zero-th order approximation of homogeneity and isotropy simplifies the general space time metric $ds^2 = g_{\mu\nu}dx^\mu dx^\nu$, where $g_{\mu\nu}$

Chapter 1. Cosmology and cosmic structure formation

denotes the metric tensor, to the well known Robertson-Walker metric. In spherical coordinates $\mathbf{r} = (w, \theta, \phi)$ the line element is given by

$$ds^2 = -c^2 dt^2 + a^2(t) [dw^2 + f_K^2(w) (d\theta^2 + \sin^2(\theta)d\phi^2)], \quad (1.1)$$

where $a(t)$ denotes the scale factor, which stretches isotropically the 3d spatial sections of the 4d space-time. It is common to normalise $a = 1$ at present time. The radial function f_K is given by

$$f_K^2(w) = \begin{cases} \frac{1}{\sqrt{K}} \sin(\sqrt{K}w) & (K > 0), \text{ spherical,} \\ w & (K = 0), \text{ flat,} \\ \frac{1}{\sqrt{|K|}} \sin(\sqrt{|K|}w) & (K < 0), \text{ hyperbolic,} \end{cases} \quad (1.2)$$

and K denotes the curvature parameter, which can be either positive, negative or zero with the dimension of an inverse square length. An immediate consequence of the changing scale of the Universe is the cosmological redshift z , which is the Doppler shift due to emitter's recession with the Hubble flow and is therefore related to the scale factors at the time of emission a and observation a_0 :

$$z \equiv \frac{\lambda_0}{\lambda} - 1 = \frac{a_0}{a} - 1, \quad (1.3)$$

giving for a present time observer ($a_0 = 1$)

$$a = \frac{1}{1+z} \quad (1.4)$$

the important relation for converting between redshift and scale factor.

1.1.2 Understanding the cosmo-dynamics

Having specified the Friedmann-Robertson-Walker metric for homogeneous and isotropic space times, one can derive the equations governing the dynamical evolution of the Universe as a whole by inserting the metric into Einstein's field equations (Einstein 1916) given by:

$$R_{\mu\nu} - \frac{1}{2}Rg_{\mu\nu} = \frac{8\pi G}{c^4}T_{\mu\nu} + \Lambda g_{\mu\nu}, \quad (1.5)$$

where $R_{\mu\nu}$ is the Ricci tensor, R the Ricci scalar, Λ is the cosmological constant and $T_{\mu\nu}$ the energy-momentum tensor. By inserting the metric Eq. 1.1 and the energy-momentum tensor $T_{\mu\nu} = (\rho + p/c^2)u_\mu u_\nu + Pg_{\mu\nu}$ of the perfect fluid, where u_μ is the 4-velocity of matter, ρ denotes the mean energy density and P is the mean pressure, into Einstein's equations above, one obtains the following two ordinary differential equations (Friedmann 1922, 1924):

$$\left(\frac{\dot{a}}{a}\right)^2 = \frac{8\pi G}{3}\rho - \frac{Kc^2}{a^2} + \frac{\Lambda}{3}, \quad (1.6)$$

$$\frac{\ddot{a}}{a} = -\frac{4\pi G}{3}\left(\rho + \frac{3P}{c^2}\right) + \frac{\Lambda}{3}, \quad (1.7)$$

1.1. Friedmann-Lemaître-Walker cosmology

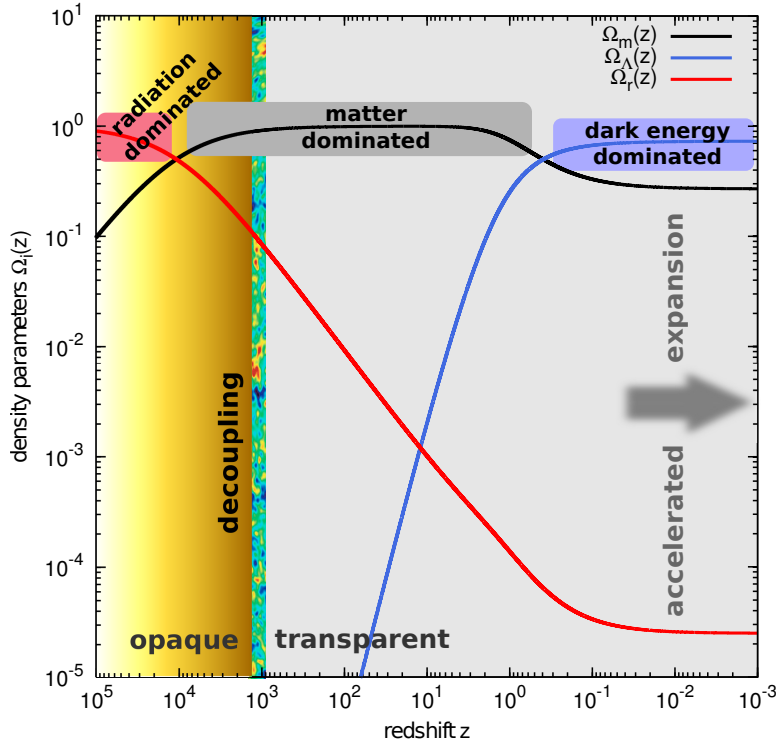


Figure 1.1: Evolution of the different density parameters Ω_i with redshift z for the flat Λ CDM cosmology. Due to their different scaling behaviour, the density parameters for matter (black line), radiation (red line) and the cosmological constant (blue line) change significantly with time, resulting in three epochs individually dominated by each of them. For better orientation in the time line of cosmic history, the last-scattering surface at the era of decoupling has been added.

for the three independent functions $a(t)$, $\rho(t)$ and $P(t)$. The two Friedmann equations 1.6 can be combined to obtain the adiabatic equation

$$\frac{d}{dt} [\rho(t)c^2 a^3(t)] + P \frac{d}{dt} a^3 = 0, \quad (1.8)$$

stating that the change of energy in a fixed comoving volume equals the pressure times the change in proper volume. Thus, it is the first law of thermodynamics in a cosmological context. From Eq. 1.8 one can infer the evolution of $\rho(a)$ once the pressure P as a function of ρ is known.

In practice, one recasts the Friedmann equation in a more convenient form by introducing the Hubble function $H(a)$, being \dot{a}/a the relative expansion rate:

$$H^2(a) = H_0^2 (\Omega_{r0} a^{-4} + \Omega_{m0} a^{-3} + \Omega_K a^{-2} + \Omega_\Lambda), \quad (1.9)$$

$$= H_0^2 E^2(a), \quad (1.10)$$

Chapter 1. Cosmology and cosmic structure formation

Table 1.1: Cosmological parameters obtained from the 5-year data release of WMAP (Komatsu et al. 2009), without and with the additional constraints imposed by baryonic acoustic oscillations (BAOs) and supernovae SNe. The normalisation parameter σ_8 and the spectral index n_s are both defined in Subsect. 1.2.4. Note that, apart from the first two rows, spatial flatness ($K = 0$) was assumed in deriving the given parameter values. T_{CMB} has been taken from Fixsen et al. (1996). The table has been adopted from Bartelmann (2010).

parameter	symbol	WMAP-5			
		alone	+ BAO + SNe (reference)		
CMB temperature	T_{CMB}	2.728	\pm	0.004 K	–
total energy density	Ω_{tot}	1.099	\pm	$\frac{0.100}{0.085}$	1.0052 \pm 0.0064
matter density	$\Omega_{\text{m}0}$	0.258	\pm	0.03	0.279 \pm 0.015
baryon density	$\Omega_{\text{b}0}$	0.0441	\pm	0.0030	0.0462 \pm 0.0015
cosmological constant	$\Omega_{\Lambda 0}$	0.742	\pm	0.03	0.721 \pm 0.015
Hubble constant	h	0.719	\pm	$\frac{0.026}{0.027}$	0.701 \pm 0.013
power-spectrum normalisation	σ_8	0.796	\pm	0.036	0.817 \pm 0.026
age of the Universe in Gyr	t_0	13.69	\pm	0.13	13.73 \pm 0.12
decoupling redshift	z_{dec}	1087.9	\pm	1.2	1088.2 \pm 1.1
reionisation optical depth	τ	0.087	\pm	0.017	0.084 \pm 0.016
spectral index	n_s	0.963	\pm	$\frac{0.014}{0.015}$	0.960 \pm $\frac{0.014}{0.013}$

where $H(z=0) \equiv H_0$ is the Hubble constant, which is often expressed in dimensionless form as

$$h \equiv \frac{H_0}{100 \text{ km s}^{-1} \text{ Mpc}^{-1}} \simeq 0.7, \quad (1.11)$$

and the four dimensionless density parameters $\Omega_{\text{r}0}$, $\Omega_{\text{m}0}$, Ω_{Λ} , Ω_{K} describe the matter energy content in the Universe in units of the critical density ρ_{crit}

$$\rho_{\text{crit}} \equiv \frac{3H_0^2}{8\pi G}. \quad (1.12)$$

If, in a given cosmological model, all densities add up to ρ_{crit} , then all spatial hypersurfaces are flat and therefore the curvature K vanishes. These models are usually referred to as *flat* models. Due to the fact that the critical density as well as the densities themselves evolve with time, so do the density parameters. In Fig. 1.1 the evolution of $\Omega_{\text{r}0}$, $\Omega_{\text{m}0}$ and Ω_{Λ} is shown throughout the cosmic history. Immediately one identifies three epochs, namely the present epoch of Λ or dark energy (DE) domination (see also chapter 3 for more details) with its accelerated expansion of the Universe, followed by the matter-dominated era and finally the radiation dominated epoch. For reference the most important cosmological parameters are summarised in Tab. 1.1, adopted from the WMAP5 results (Komatsu et al. 2009). They represent the standard Λ CDM cosmology assumed in this work, unless stated otherwise.

1.1. Friedmann-Lemaître-Walker cosmology

1.1.3 Cosmic distances

A very important aspect of cosmology, even if, in comparison to Euclidean space, not evident at first sight, is the definition of distance measures, which in curved and non-stationary space-time are no longer unique for different measurement prescriptions, leading to different distances (Bartelmann & Schneider 2001; Hogg 1999). In the following, we define four different distance measures: the proper distance, the comoving distance, the angular-diameter distance and the luminosity distance.

Proper distance The proper distance D_P is the distance measured by the light-travel time, thus

$$dD_P = c dt \quad \Rightarrow \quad D_P = \frac{c}{H_0} \int \frac{da}{aE(a)}, \quad (1.13)$$

where the integral has to be evaluated between the scale factors of emission and observation of the light signal.

Comoving distance The comoving radial coordinate w is the comoving distance D_C measured along a radial light ray. Since light rays propagate with zero proper time, $ds = 0$, this gives

$$dw = \frac{cdt}{a} \quad \Rightarrow \quad D_C(a) = c \int \frac{da}{a\dot{a}} = \frac{c}{H_0} \int \frac{da}{a^2 E(a)}, \quad (1.14)$$

which is commonly used e.g. in gravitational lensing and simulations of structure formation.

Angular-diameter distance The angular-diameter distance D_A is defined such that the same relation as in Euclidean space holds between the physical size of an object and its angular size. It becomes

$$D_A(a) = a f_K[D_C(a)], \quad (1.15)$$

with $f_K(w)$ given by Eq. 1.2.

Luminosity distance Analogously to the Euclidean relation between the bolometric luminosity of an object and its observed flux, the luminosity distance D_L turns out to be

$$D_L(a) = \frac{D_A(a)}{a^2} = \frac{f_K[w(a)]}{a}, \quad (1.16)$$

being proportional to the angular-diameter distance.

Of all four distance measures, only D_P , D_C and D_L are monotonic in a , whereas D_A features a maximum around a redshift of $z \approx 1$, which means that more distant objects with $z \gtrsim 1$ exhibit a growing angular size. Furthermore, it should be noted that only D_P and D_C are additive.

1.1.4 Horizon size

The finiteness of the speed of light raises the question about the size of the causally connected regions in the Universe. Usually this size is referred to as *horizon size* and is given by the distance a photon can travel in the time t since the Big Bang. The natural time scale of the Universe is given by the inverse Hubble parameter $H^{-1}(a)$, thus the horizon size is $d_H' = cH^{-1}(a)$ and the comoving horizon size is

$$d_H = \frac{c}{aH(a)}. \quad (1.17)$$

Inserting present time values, it yields the *Hubble radius* $r_H = cH_0^{-1} \approx 3 \text{ Gpch}^{-1}$, which defines the observable Universe. The horizon size

$$d_H(a_{\text{eq}}) = \frac{1}{\sqrt{2}} \frac{c}{H_0} \left(\frac{a_{\text{eq}}}{\Omega_{\text{m}0}} \right)^{1/2} \approx 12(\Omega_{\text{m}0}h^2)^{-1} \text{ Mpc} \quad (1.18)$$

at the scale factor of matter-radiation equality a_{eq} (see also Fig. 1.1) plays an important role in structure formation as discussed in the following section.

1.2 Structure formation

The assumption of homogeneity and isotropy, as it is outlined in the previous Sect. 1.1, can not be valid on all scales given the large variety of structures, such as stars, galaxies and galaxy clusters, we observe in the Universe. However it turns out that, when averaged over sufficiently large scales ($> 100 h^{-1} \text{ Mpc}$), it is justified to treat the Universe as consisting of a uniform smooth background (as described Sect. 1.1) with inhomogeneities superimposed on it. In the following section, I will briefly summarize the theory of structure formation as it is relevant for the scopes of this work.

1.2.1 General remarks

The basic paradigm of structure formation assumes that at early times small fluctuations of quantum origin existed, which grew by gravitational instability. In the study of the growth of these fluctuations, one distinguishes two regimes:

Linear regime As long as the inhomogeneities are small, their growth can be described by linear perturbations to the otherwise smooth background. This approach is very powerful in the early stages of clustering, thanks to its mathematical simplicity.

Non-Linear regime Once the deviations from the background become large, linear perturbation theory breaks down and the system enters the stage of non-linear evolution. Usually the non-linear regime is mainly studied in numerical simulations.

1.2. Structure formation

Table 1.2: Strategy for the treatment of perturbations in cosmology for the different possible cases, where λ denotes the wavelength of the perturbation, $d_H(a)$ is the Hubble radius and a_{eq} is the scale factor at matter-radiation equality.

<i>Regime</i>	<i>Treatment</i>	<i>Era</i>	<i>Processes</i>
$\lambda > d_H(a), a < a_{\text{eq}}$	general relativistic	radiation-dominated	linear
$\lambda < d_H(a), a < a_{\text{eq}}$	Newtonian	radiation-dominated	linear
$\lambda < d_H(a), a > a_{\text{eq}}$	Newtonian	matter-dominated	linear + non-linear

When applying general relativity, one assumes that averaging the matter density and solving the Einstein equations with the smooth density distribution will lead to results comparable to those obtained by averaging the exact solutions based on an inhomogeneous matter distribution. Unfortunately, the exact solutions are not known with any degree of confidence. Up to now there is no observational evidence that a correction to this assumption is needed.

In the general relativistic treatment, one considers perturbations of the metric $g_{\mu\nu}$ and the stress-energy tensor $T_{\mu\nu}$, which may be defined as $\bar{g}_{\mu\nu} = g_{\mu\nu} + \delta g_{\mu\nu}$ and $\bar{T}_{\mu\nu} = T_{\mu\nu} + \delta T_{\mu\nu}$, where the bar denotes background plus perturbations. In case the perturbations ($\delta g_{\mu\nu}, \delta T_{\mu\nu}$) are small compared to the smooth background ($g_{\mu\nu}, T_{\mu\nu}$), one can linearise Einstein's equations to obtain a second order differential equation. In general, the metric perturbation $\delta g_{\mu\nu}$ and matter perturbation $\delta T_{\mu\nu}$ can be decomposed into three types of perturbations:

- **scalar-type:** This category is very important for structure formation, since ordinary density fluctuations belong to this type of perturbations.
- **vector-type:** Describing vortical modes that are quickly damped away by cosmic expansion and are therefore negligible for structure formation applications.
- **tensor-type:** Including primordial gravitational waves that may be detected by CMB polarisation probes in the form of B-modes.

It is possible to assign to every perturbation a comoving wavelength λ that has to be compared to the horizon size $d_H(a)$ at a given time, since d_H is comparable to the space-time curvature. This means that, for perturbations that are comparable or larger than the horizon, the Newtonian theory can no longer be applied. When going back to sufficiently early times, this will happen to all perturbations. Yet for many applications, Newtonian theory is still applicable (see Tab. 1.2) and the main features can nevertheless be understood by a relatively simple reasoning.

1.2.2 Linear growth

The perturbations in the dark matter density field $\rho(\mathbf{x}, t)$ can be characterised by the density contrast

$$\delta(\mathbf{x}, t) \equiv \frac{\rho(\mathbf{x}, t) - \bar{\rho}(t)}{\bar{\rho}(t)}, \quad (1.19)$$

where $\bar{\rho}(a) = \Omega_{m0}\rho_{\text{crit}}a^{-3}$ is the mean cosmic density and \mathbf{x} are comoving coordinates. By means of relativistic and non-relativistic perturbation theory, in the linear regime $|\delta| \ll 1$ one can show that perturbations grow differently during the epochs of matter- and radiation domination

$$\delta(a) = \begin{cases} a^2 & , a < a_{\text{eq}}, \text{ radiation-dominated era} \\ a & , a > a_{\text{eq}}, \text{ matter-dominated era} \end{cases} \quad (1.20)$$

as long as the Einstein-de Sitter limit $\Omega_m \approx 1$ holds. At late time when matter ceases to dominate and the cosmological constant takes over (see Fig. 1.1), this is no longer fulfilled and the linear growth of density perturbations can be obtained from

$$\ddot{\delta} + 2H\dot{\delta} - 4\pi G\bar{\rho}\delta = 0. \quad (1.21)$$

Neglecting the decaying mode, one is left with the growing solution which is usually written as δ_0 by $\delta(a) = \delta_0 D_+(a)$, introducing the density contrast today δ_0 and the growth factor

$$D_+(a) \equiv \frac{\delta(a)}{\delta(1)} = \frac{G(a)}{G(1)}, \quad (1.22)$$

for which the growth function $G(a)$ is accurately fit by Carroll et al. (1992)

$$G(a) \equiv a\Omega_m(a) \left[\Omega_m^{4/7}(a) - \Omega_\Lambda(a) + \left(1 + \frac{\Omega_m(a)}{2}\right) \left(1 + \frac{\Omega_\Lambda(a)}{70}\right) \right]^{-1}. \quad (1.23)$$

Eq. 1.23 deviates from the accurate solution by $\leq 0.2\%$ for $a \in [0.01, 1]$ for a standard cosmological model.

1.2.3 Suppression of growth

Another important aspect of structure growth is that it can be shown that perturbations that enter the horizon in the radiation dominated phase grow only logarithmically, whereas super-horizon modes, entering the horizon later, grow $\propto a^2$ for $a < a_{\text{eq}}$ and during matter-domination $\propto a$. The difference during radiation domination stems from the fact that the expansion time scale t_{Hubble} , determined by the radiation density ρ_r , is smaller than the collapse time scale of the dark matter t_{DM}

$$t_{\text{Hubble}} \propto \frac{1}{\sqrt{G\rho_r}} < \frac{1}{\sqrt{G\rho_{\text{DM}}}} \propto t_{\text{DM}}. \quad (1.24)$$

Therefore the horizon size Eq. 1.18 defines a very important length scale in structure formation since, during radiation domination, scales smaller than $d_H(a_{\text{eq}})$ are

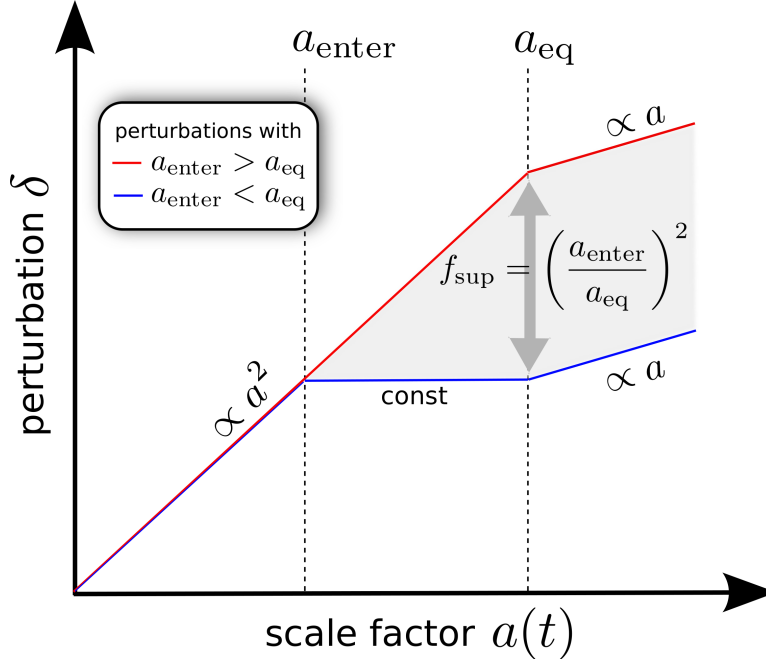


Figure 1.2: The evolution of the dark matter density contrast δ is schematically shown, with the scale factor $a(t)$, for perturbations that enter the horizon before matter-radiation equality (blue line) and perturbations that enter at or after it (red line). The grey shaded region depicts the suppression of growth for the small scale perturbations (Mészáros effect).

suppressed with respect to larger scales. This effect is also known as Mészáros effect (Mészáros 1975, 1974). From Fig. 1.2 it can directly be inferred that these perturbations are suppressed by a factor of

$$f_{\text{sup}} = \left(\frac{a_{\text{enter}}}{a_{\text{eq}}} \right)^2. \quad (1.25)$$

This suppression plays an important role for the determination of the shape of the dark matter power spectrum as discussed in the following subsection.

1.2.4 The power spectrum

As a consequence of the central limit theorem, the density fluctuations $\delta(\mathbf{x})$ are assumed to be Gaussian, meaning that the probability to find a density contrast between δ and $\delta + d\delta$ is given by a Gaussian distribution. Since, according to Eq. 1.19, the mean vanishes by construction, the density field is solely defined by the variance. Usually, one uses the power spectrum $P_\delta(\mathbf{k})$, which is defined by

$$\langle \hat{\delta}(\mathbf{k}) \hat{\delta}^*(\mathbf{k}') \rangle \equiv (2\pi)^3 \delta_{\mathbf{D}}(\mathbf{k} - \mathbf{k}') P_\delta(k), \quad (1.26)$$

Chapter 1. Cosmology and cosmic structure formation

with the Fourier transform $\delta(\mathbf{k}) = \int d^3x \delta(\mathbf{x}) \exp(-i\mathbf{k}\mathbf{x})$ and δ_D is the Dirac function, ensuring that modes with different wave vectors are independent. The density field grows homogeneously according to linear perturbation theory, therefore we expect the individual Fourier modes to grow independently

$$\delta(\mathbf{x}, a) = D_+(a) \delta(\mathbf{x}, 1) \rightarrow \delta(\mathbf{k}, a) = D_+(a) \delta(\mathbf{k}, 1), \quad (1.27)$$

as long as the perturbations can be considered as being small compared to the comoving horizon size.

The power spectrum $P_\delta(k)$ is considered to be scale invariant on large scales, $P_\delta(k) \propto k^{n_s}$, with the spectral index $n_s \simeq 1$ (Harrison 1970; Peebles & Yu 1970; Zel'dovich 1972). On small scales, however, the suppression of growth during the era of radiation domination has to be taken into account and the horizon size $d_H(a_{\text{eq}})$ given by Eq. 1.18 imprints therefore a scale $k_{\text{eq}} = 2\pi/d_H(a_{\text{eq}}) \simeq 0.01 \text{ Mpc}^{-1}$ to the power spectrum above which $P_\delta(k) \propto k^{n_s-4}$. This stems from the fact that the suppression of the power spectrum for small scales is $\propto f_{\text{sup}}^2 \propto k^{-4}$. Having the asymptotic behaviour

$$P_\delta(k) \propto \begin{cases} k^{n_s} & (k \ll k_{\text{eq}}) \\ k^{n_s-4} & (k \gg k_{\text{eq}}) \end{cases}, \quad (1.28)$$

the remaining task for a full description of $P_\delta(k)$ is to link smoothly the two asymptotic regimes, by means of solving the full structure evolution equations with Boltzmann codes. Bardeen et al. (1986) introduced a fit that is, apart from baryonic effects, particularly accurate till today

$$P_\delta(k, z) = A k^{n_s} T^2(k) D_+^2(z) \quad (1.29)$$

with the transfer function

$$T(q) = \frac{\ln(1 + 2.34q)}{2.34q} [1 + 3.89q + (16.1q)^2 + (5.46q)^3 + (6.71q)^4]^{-1/4}, \quad (1.30)$$

where q is defined to be

$$q = \frac{k/(\text{Mpc}^{-1} h)}{\Gamma}, \quad \text{with } \Gamma = \Omega_{\text{m}0} h \exp \left[-\Omega_{\text{b}0} \left(1 + \frac{\sqrt{2}h}{\Omega_{\text{m}0}} \right) \right], \quad (1.31)$$

and Γ is the *shape parameter* (Efstathiou et al. 1992; Sugiyama 1995). The normalisation factor A in Eq. 1.29 is usually defined via the parameter σ_8 , being defined as the variance of the density fluctuations on scales of 8 Mpc:

$$\sigma_8^2 = \int \frac{d^3k}{(2\pi)^3} |\tilde{W}_R(k)|^2 P_\delta(k), \quad (1.32)$$

1.3. Cosmic microwave background

requiring a window function W_R , whose Fourier transform in the case of a top-hat and a Gaussian smoothing respectively given by

$$\tilde{W}_R(k) = 3 \frac{\sin(kR) - kR \cos(kR)}{(kR)^3} \quad \text{and} \quad \tilde{W}_R(k) = \exp\left[-\frac{(kR)^2}{2}\right]. \quad (1.33)$$

According to Tab: 1.1 we have currently $\sigma_8 = 0.817$ in the standard Λ CDM framework.

1.3 Cosmic microwave background

The cosmic microwave background (CMB) will occur in several places throughout this work, therefore this section is meant as a short reminder about the main features of the CMB, which is one of the pillars on which the notion of Big Bang cosmology is built upon. For more detailed information the reader is referred to the book by Durrer (2008).

1.3.1 Overview

The existence of the CMB was predicted in 1948 by Gamow (1948) and by Alpher & Herman (1948), who estimated, for one of the scenarios they considered, the CMB temperature to be of the order of ~ 5 K, remarkably close to the nowadays measured $T_{\text{CMB}} = 2.725$ K (Fixsen et al. 1996). The CMB originates in the early hot phase of the Universe, when photons and electromagnetically interacting particles were in thermal equilibrium with each other (Dicke et al. 1965). However this state holds only temporarily, since the expanding Universe cools adiabatically, reaching sufficiently low temperatures such that the photons drop out of equilibrium and therefore electrons combine with protons and α -particles to hydrogen and helium. In this way, the rapid drop in the abundance of charged particles results in the Universe becoming transparent around $z_{\text{dec}} \simeq 10^3$ and thus the photons can travel freely as depicted in Fig. 1.4, maintaining the Planckian spectrum they had acquired when they were in thermal equilibrium with the electron-positron plasma. The temperature of the CMB photons drops proportionally to the scale factor, leading to the aforementioned value that is observed nowadays. Surprisingly, it took

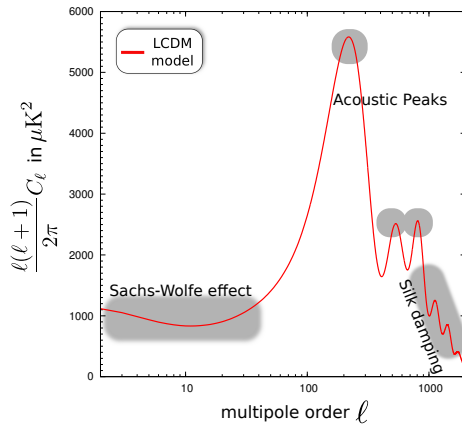


Figure 1.3: Schematic of the CMB power spectrum and the dominant physical effects leading to its distinct shape for the standard Λ CDM cosmology, computed with *CMBEASY*.

Chapter 1. Cosmology and cosmic structure formation

another seventeen years until the relic radiation was serendipitously discovered by Penzias & Wilson (1965).

When taking into account the considerations about the formation of structures in Sect. 1.2, one expects to find in the CMB seed fluctuations of the rich structures we see today. And indeed observational probes like BOOMERANG, MAXIMA, COBE and WMAP, culminating in the ongoing *PLANCK* mission introduced in Chap. 4, found tiny anisotropies of the order of $\Delta T/T \simeq 10^{-5}$. Those tiny temperature perturbations were imprinted on the CMB by density perturbations present at the time of decoupling by means of various mechanisms (see also Fig. 1.3), arising from the interplay of gravity and the radiation pressure:

Sachs-Wolfe effect Photons released in overdense regions are redshifted since they have to climb out the potential wells and thus they are cooler than the average CMB temperature. This effect is dominant on scales larger than the sound horizon (Sachs & Wolfe 1967).

Acoustic oscillations On scales smaller or comparable to the sound horizon, the radiation pressure can counterbalance the pull of gravity, leading to oscillations in the plasma-photon fluid. Due to the fact that these oscillations are coherent at a fixed physical scale, they can be observed as distinct peaks in the CMB power spectrum, like shown in Fig. 1.3.

Silk damping On small scales the radiation pressure can exceed self gravity, so that the density perturbations are destroyed by baryons leaving the overdense regions along with the photons and thus reducing the anisotropies on small scales (Silk 1968).

Apart from the primary CMB anisotropies as briefly introduced above, structure growth itself imprints a plethora of secondary anisotropies, either by the interaction of CMB photons with electrons (Sunyaev-Zel'dovich effects, Ostriker-Vishniac effect), or by gravitational interaction (integrated Sachs-Wolfe effect, Rees-Sciama effect, CMB Lensing). In this thesis, the focus is mainly directed on the Sunyaev-Zel'dovich effect covered in more detail in Sect. 2.2.3.

1.3.2 Statistical description

The CMB fluctuations are assumed, according to our notion of inflation, to be a Gaussian random field, that we describe by its value $a(\theta)$ in the direction $\theta = (\theta, \varphi)$ on the sky. This field can be decomposed into spherical harmonics $Y_{\ell m}(\theta, \varphi)$, forming a functional basis in spherical coordinates

$$a_{\ell m} = \int_{4\pi} d\Omega a(\theta) Y_{\ell m}^*(\theta) \text{ and } a(\theta) = \sum_{\ell=0}^{\infty} \sum_{m=-\ell}^{+\ell} a_{\ell m} Y_{\ell m}(\theta). \quad (1.34)$$

1.3. Cosmic microwave background

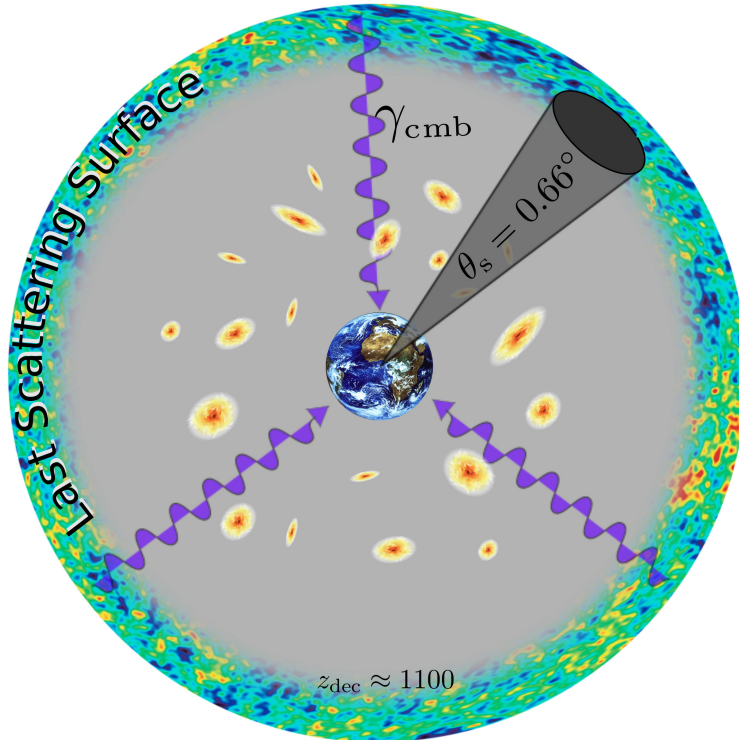


Figure 1.4: Scheme of the CMB, assuming that the peculiar velocity with respect to the CMB restframe has been subtracted. The dark grey cone depicts the causally connected patches at the redshift of decoupling z_{dec} , defined by angular scale θ_s of the sound horizon $w_s = 163.3 \text{ Mpc}$. The photons γ_{cmb} carrying the information from the primary anisotropies have to pass the gravitational potential wells (being time dependent in case of $\Omega_\Lambda \neq 0$) giving rise to signatures of ISW, RS and CMB lensing. Furthermore the photons interact with the hot gas (electrons) in those potential wells causing observable features from the Sunyaev-Zel'dovich and Ostriker-Vishniac effects.

From the spherical harmonic coefficients $a_{\ell m}$, one can obtain the angular power spectrum $C(\ell)$ by averaging over all $2\ell + 1$ values of m at a given multipole ℓ

$$C_\ell \equiv \frac{1}{2\ell + 1} \sum_{m=-\ell}^{\ell} |a_{\ell m}|^2, \quad (1.35)$$

reflecting the expectation of statistical isotropy. By the assumption of Gaussianity, all statistical information is contained in the power spectrum, analogously to what was said in Subsect. 1.2.4.

Fig: 1.3 shows C_ℓ for the standard ΛCDM model computed with the Boltzmann code *CMBEASY* (Doran 2005). In general, the power spectrum C_ℓ is a powerful tool for the estimation of cosmological parameters, as listed in Tab. 1.1, by fitting

Chapter 1. Cosmology and cosmic structure formation

the theoretical to the observed power spectrum.

Whenever anyone says, 'theoretically,' they really mean, 'not really.'

Dave Parnas (1941-)

2

Galaxy clusters

Being the most massive gravitationally bound systems in the Universe, galaxy clusters are the biggest items in the cosmic warehouse that can be studied nowadays. In the hierarchical picture of structure formation, clusters are the largest objects that had time to collapse under the influence of their own gravity and principally reach virial equilibrium through relaxation processes. The study of galaxy clusters is worthwhile for two reasons. First, clusters probe the amount of structures at the high-mass end of $10^{14} - 10^{15} M_{\odot}$ at low redshifts. By comparison with probes of structures at higher redshifts, we can infer the rate of structure growth, containing information about the cosmic evolution. Second, clusters can be considered as highly interesting closed astrophysical laboratories in which the gaseous matter can be studied, thanks to the deepness of their gravitational potential well. In clusters we observe galaxy formation, ram-pressure stripping as well as feedback processes stemming from SNe and AGNs.

2.1 Formation and abundance

The formation of dark matter haloes is central to the hierarchical build-up of structures in the Universe, where larger structures are formed through merging and accretion of smaller objects. Modelling the abundance of these collapsed systems is one of the interesting challenges in modern cosmology.

2.1.1 Spherical collapse

Haloes, assumed to be spherical overdense clouds of dark matter, can principally reach highly non-linear densities in their centres, hardening their analytic treatment. However, an approximative understanding of the properties of such haloes can be achieved by investigating the evolution of a homogeneous overdense sphere, the so called spherical collapse or *top-hat* model, embedded in the evolving background cosmology.

In a matter-dominated Universe, the equation of motion $\ddot{r} = -GM/r^2$ for a shell of

Chapter 2. Galaxy clusters

radius $r(t)$ of a spherical top-hat, encompassing a mass M , is solved by

$$r(\theta) = A(1 - \cos \theta), \quad (2.1)$$

$$t(\theta) = B(\theta - \sin \theta), \quad (2.2)$$

with $A^3 = GMB^2$ and the phase angle θ . As depicted in Fig. 2.1, the spherical overdensity will grow and at a certain point decouple from the cosmic background evolution, reaching a maximum radius $\theta = \pi, t = \pi B$ and finally collapsing to a point at $\theta = 2\pi$. Extrapolating the linear theory leads to the linear critical density contrast $\delta_c = 1.69$. A more sophisticated treatment of the spherical collapse is given in Chapter 8.

Under the assumption of exact symmetry, a spherical top-hat overdensity would collapse to a single point. In reality however, even the slightest deviation from this symmetry prevents the collapse to a point. Instead the halo reaches a state of virial equilibrium by *violent relaxation* (phase mixing). One considers the total energy $E_{\text{ta}} = -(3/5)GM^2/r_{\text{ta}}$ at turnaround to be the starting point for quantifying the state of the virialised halo, in case that no kinetic energy is present and no mass loss is expected afterwards. When the halo is virialised, one has $E_{\text{ta}} = U_{\text{vir}} + K_{\text{vir}}$, which can be recast by using the virial theorem $U = -2K$ to give

$$E_{\text{ta}} = \frac{1}{2}U_{\text{vir}} = -\frac{1}{2}\frac{3GM^2}{5r_{\text{vir}}}, \quad (2.3)$$

from which $r_{\text{vir}} = (1/2)r_{\text{ta}}$ can be inferred. By assuming that virialisation happens at collapse time $t_{\text{coll}} \simeq 2\pi B$, one can estimate the final overdensity after collapse to be $\Delta_V = 18\pi^2 \approx 178$ which is often approximated by $\Delta_V = 18\pi^2 \approx 178$. The parameters Δ_V and δ_c , as derived from relatively simple reasoning turn out to be great of importance for the characterisation of dark matter haloes and will reoccur at many places throughout this work.

By means of the virial radius, further characterising quantities like the radial velocity v_{rot} and the virial temperature T_{vir} can be derived and are given by

$$v_{\text{rot}} = \sqrt{\frac{GM}{r_{\text{vir}}}}, \quad \text{and} \quad T_{\text{vir}} = \frac{\mu m_p v_{\text{rot}}^2}{2k_b}. \quad (2.4)$$

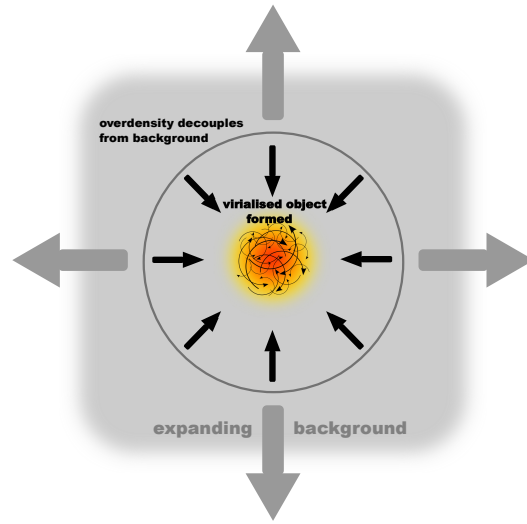


Figure 2.1: Schematic for the idea of the spherical collapse.

2.1. Formation and abundance

Here μ is the mean molecular weight, depending on the ionisation fraction and composition of the gas, and m_p is the proton mass.

The rather simple notion of the spherical collapse model is of high value for the understanding of halo formation. However for more detailed studies including particularly the non-linear evolution, either more sophisticated calculations, or more commonly numerical simulations have to be performed.

2.1.2 Halo density profiles

The internal structure of dark matter haloes, namely their density and mass profiles, are still theoretically and observationally not well understood. According to the virial theorem, total energy is minus half its potential energy and thus, any inevitable energy loss makes the potential energy become more negative, making haloes more tightly bound, which in turn increases their energy loss. Therefore, any system of self-gravitating particles does not have an equilibrium state, so that any density profile must reflect a potentially long-lived, but transient state.

Isothermal profile

The simple analytic model of the isothermal sphere is based on a spherically-symmetric, self gravitating system of non-interacting particles, whose kinetic energy is characterized by a constant temperature T . The system is described by the Euler equations of hydrostatic equilibrium and the equation-of-state for the ideal gas

$$\frac{dp}{dr} = -\frac{GM(r)}{r^2}\rho, \quad \text{and} \quad p = \frac{\rho}{m}kT, \quad (2.5)$$

where m is the mass of the particles constituting the sphere. By combining these two equations and by replacing the mass by the integral over the density, one can derive a second-order differential equation

$$\frac{d}{dr} \left(r^2 \frac{d \ln \rho}{dr} \right) = -\frac{4\pi Gm}{kT} r^2 \rho, \quad (2.6)$$

having two solutions. First, a singular one given by

$$\rho_1(r) = \frac{\sigma^2}{2\pi G r^2}, \quad \text{with} \quad \sigma^2 := \frac{kT}{m}, \quad (2.7)$$

where σ is the (radially constant) velocity dispersion of the particles. And second, a non-singular one that can be approximately expressed by

$$\rho_2(r) = \rho_0 \left[1 + \left(\frac{r}{r_0} \right)^2 \right]^{-1}, \quad (2.8)$$

where ρ_0 and the core radius r_0 are constants. Both isothermal sphere solutions are able to reproduce flat rotation curves of galaxies. One of the drawbacks however is that a stable "gas" sphere can not have a constant temperature, because particles would evaporate from it.

The NFW profile

Numerical N-body simulations show that the density profiles of haloes are not well described by the isothermal sphere. However, Navarro et al. (1996, 1997) showed that there seems to exist a universal density profile, nowadays known as *NFW-profile*, with rather gently changing logarithmic slopes. The NFW-type profiles are based on the following formula

$$\frac{\rho(r)}{\rho_{\text{crit}}} = \frac{\delta_{\text{char}}}{x(1+x)^2}, \quad \text{with } x = r/r_s \quad (2.9)$$

where $r_s = r_{\text{vir}}/c_\Delta$ is the scale radius, c_Δ is the halo concentration and δ_{char} is the characteristic density. The characteristic density δ_{char} can be written in terms of the halo concentration c_Δ , by using the definition of a virialised region. According to the considerations in Sect. 2.1, a virialised region of size r_{vir} is 200 times denser than the background, such that one can relate δ_{char} and c_Δ , using $M_{200} = 200(4\pi/3)\rho_{\text{crit}}r_{200}^3$, where on the left hand side one has to integrate over the NFW-profile. Solving for δ_{char} yields

$$\delta_{\text{char}} = \frac{200}{3} \frac{c_\Delta^3}{\ln(1+c_\Delta) - c_\Delta/(1+c_\Delta)}. \quad (2.10)$$

The halo concentration c_Δ itself depends on the halo mass, redshift and the cosmological parameters. In general, c_Δ is the higher the earlier the haloes are formed, because the haloes “recall” the surrounding density present at their formation time. From Eq. 2.9 it is evident that, in the inner parts, the profile drops with $\propto x^{-1}$ and the outer regions $\propto x^{-3}$. The obvious divergence for large radii is usually not a fundamental problem, since any density profile must become invalid as soon as $\rho(r)$ drops to the cosmic background density.

2.1.3 The mass function

Apart from understanding the internal structure of haloes, the abundance of haloes of a given mass is a crucial quantity for characterising and understanding the structures we observe in the Universe. Based on the crucial assumption that mass in all volume elements, where the linear density contrast threshold $\delta_c \approx 1.686$ from Sect. 2.1 is exceeded, is part of collapsed haloes Press & Schechter (1974) derived a theoretical model for the mass function

$$\frac{dn}{dM}(M, z) = \sqrt{\frac{2}{\pi}} \frac{\rho_0 \delta_c}{\sigma_R D_+(z) M^2} \frac{d \ln \sigma_R}{d \ln M} \exp\left(-\frac{\delta_c^2}{2\sigma_R^2 D_+^2(z)}\right), \quad (2.11)$$

which gives the number density n , of haloes in $[M, M + dM]$ at a given redshift z , where ρ_0 is the present matter density, σ_R from Eq. 1.32 is the variance of the mass fluctuations and $D_+(z)$ is the growth factor from Eq. 1.22.

2.2. Observational properties of galaxy clusters

The original work by Press & Schechter (1974) has been put onto solid mathematical grounds by Bond et al. (1991), by solving the cloud-in-cloud problem. Numerical simulations (Springel et al. 2005) have confirmed with remarkable success the improved variants of the Press-Schechter mass function (Jenkins et al. 2001; Sheth et al. 2001).

The mass functions show an exponential cut-off close to the non-linear mass scale M_* , which is the mass contained in a sphere of radius R such that $\sigma_R = 1$. Nowadays $M_* \approx 10^{13} M_\odot$ and thus the exponential cut-off in the halo mass can not be observed in the galaxy mass function, but with help of the cluster population (Rosati et al. 2002). The exponential cut-off of the cluster population offers a lever arm on constraining cosmological parameters, particularly σ_8 .

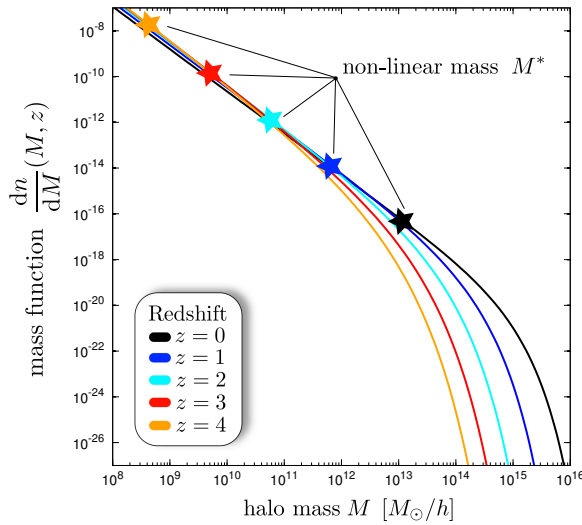


Figure 2.2: Differential comoving mass function and the respective non-linear masses (stars) for five different redshifts

2.2 Observational properties of galaxy clusters

The fact that galaxies are not uniformly distributed on the sky, but that they are clustered has already been recognised at the end of the eighteenth century by the observations of Charles Messier (1784) and William Herschel (1785). The associations formed by galaxies range from pairs and small groups till several thousands of galaxies for very big systems, and yet, if men would have not started to observe in the optical, but e.g. in the X-ray or microwave regime, they would have probably been entitled differently. In fact, clusters contain substantially more mass in the form of hot gas than in stars. Hot gas is heated up in their deep potential wells to temperatures of $10^7 - 10^8$ K causing the emission of Bremsstrahlung in the X-ray bands. At the massive end, clusters can reach masses up $10^{15} M_\odot$, massive enough to cause distortions of the background galaxies, a phenomenon known as gravitational lensing. Comparison of the mass estimates stemming from the velocity dispersion of the member galaxies and by summing up the masses of the individual galaxies show strong discrepancies leading to the conclusion that clusters are clearly dark matter dominated structures (Zwicky 1933, 1937).

Clusters can be considered as laboratories for a wealth of astrophysical processes ranging from the interplay between dark matter dynamics and gas physics to the

Chapter 2. Galaxy clusters

evolution of galaxies in the cluster environment and their interaction with the intra-cluster medium through feedback processes.

In this section, I will briefly summarise the observational properties of galaxy clusters that played an important role in the elaboration of my work by dividing them into the three different observing windows, optical, X-ray and microwave.

2.2.1 Optical

Not being in the main focus of this work, I shortly recapitulate the detection and observing methods in the optical bands.

Optical selection

The most influential work in optical cluster detection has been done by George Abell and collaborators who compiled the Abell catalogue of galaxy clusters (Abell 1958; Abell et al. 1989), comprising 4073 entries. The detection criteria required the clusters to have more than 30 members, having a nominal redshift $z \leq 0.2$ and falling within the magnitude range m_2 and $m_3 + 2$ (where m_3 is the magnitude of the third brightest member galaxy).

Though, at higher redshifts the contrast of clusters against the background galaxy counts decreases, requiring improved criteria. One widely used criterion involves the usage of colour information. Many cluster galaxies show the tendency to be significantly redder, due to the lack of ongoing star formation. In a colour vs. magnitude diagram those galaxies can be found in a distinct and narrow locus, commonly known as the *red sequence*. Furthermore, one observes also that the ratio of elliptical to spiral galaxies is inverted in clusters relative to the field,

due to strong interactions between the members in the dense environment. The HST image shown in Fig. 2.2.1 pictures the cluster Abell 2218, which can clearly be identified by eye and shows in addition strong lensing features.

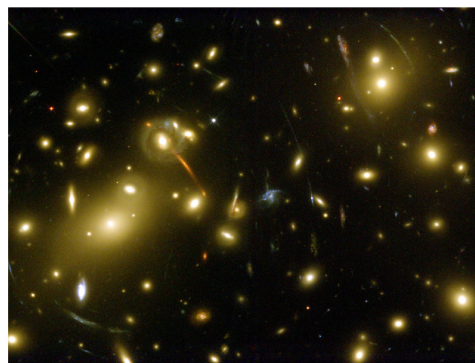


Figure 2.3: Abell 2218, strong lensing features (NASA HST Archive)

Gravitational lensing

The foundations of gravitational light deflection have been laid by Einstein (1916, 1911, 1936) and for the first time confirmed by Dyson et al. (1920) during a solar eclipse observed simultaneously from the cities of Sobral, Ceará, Brazil and in São Tomé and Príncipe on the west coast of Africa. Nowadays, gravitational lensing

2.2. Observational properties of galaxy clusters

is an essential part of the observational toolbox in astronomy and cosmology. For a sound introduction to the topic of lensing, the reader is referred to Narayan & Bartelmann (1996); Bartelmann & Schneider (2001); Bartelmann (2003). In the case of galaxy clusters, two distinct types of lensing phenomena can be observed:

Strong lensing Giant arcs, as visible in Fig. 2.2.1, are produced by rich centrally condensed clusters occasionally when a background galaxy happens to be aligned with one of the cluster caustics. In the case of strong lensing, one usually utilises a parametrised lens model optimised in order to obtain a good fit to the observed image.

Weak lensing In contrast to the strong lensing case, every cluster produces weakly distorted images of large numbers of background galaxies. Usually, these images are referred to as arclets and the phenomenon itself is called weak lensing. The application of the Kaiser & Squires (1993) algorithm and its variants (Bartelmann et al. 1996; Bradač et al. 2005; Cacciato et al. 2006; Merten et al. 2009) allows us to use weak lensing to reconstruct parameter-free two-dimensional mass maps of the lensing clusters.

The cluster mass estimates that can be obtained from a lensing analysis confirm in general the estimates that can be derived from X-ray emission or from galaxy kinematics and, therefore, they can be assumed to be on equal grounds with the ones obtained by other methods. Unfortunately, all mass estimates incorporate rather strong assumptions about the mass distribution, questioning their credibility particularly for non-relaxed systems.

2.2.2 X-rays

Clusters of galaxies are known to be strong emitters of X-ray radiation, a phenomenon that can be explained by the fact that the process of galaxy formation is highly inefficient. Galaxy formation converts about a tenth of the cosmic baryon budget in a cluster into stars in galaxies. The remainder is left adrift in the intergalactic space, where it would be extremely hard to be observed if the cluster would not possess a deep gravitational potential well, compressing the associated baryonic gas and heating it to X-ray emitting temperatures of $T \simeq 10^7 \text{ K} \dots 10^8 \text{ K}$, as depicted in Fig. 2.4. The emitting plasma, situated in the core, is relatively dilute with number densities of $n = 10^2 \text{ m}^{-3} \dots 10^3 \text{ m}^{-3}$ and yet the X-ray luminosities reach values up to $L_X = 10^{45} \text{ erg/s}$. In addition to the Bremsstrahlung, X-ray observatories have as well detected line emission from the atomic lines of highly ionised metals like Fe^{26+} .

In the case of a relaxed cluster, the hot plasma is in equilibrium with the dark matter and thus the ratio

$$\beta = \frac{\mu m_{\text{H}} \sigma_{\text{vec}}^2}{3k_{\text{B}}T} \simeq 1 \quad (2.12)$$

of the specific kinetic energy $\sigma_{\text{vec}}^2/2$ stored in random motion of the dark matter particles (being traced by galaxies) and the thermal energy of the gas $3k_{\text{B}}T/(2\mu m_{\text{H}})$

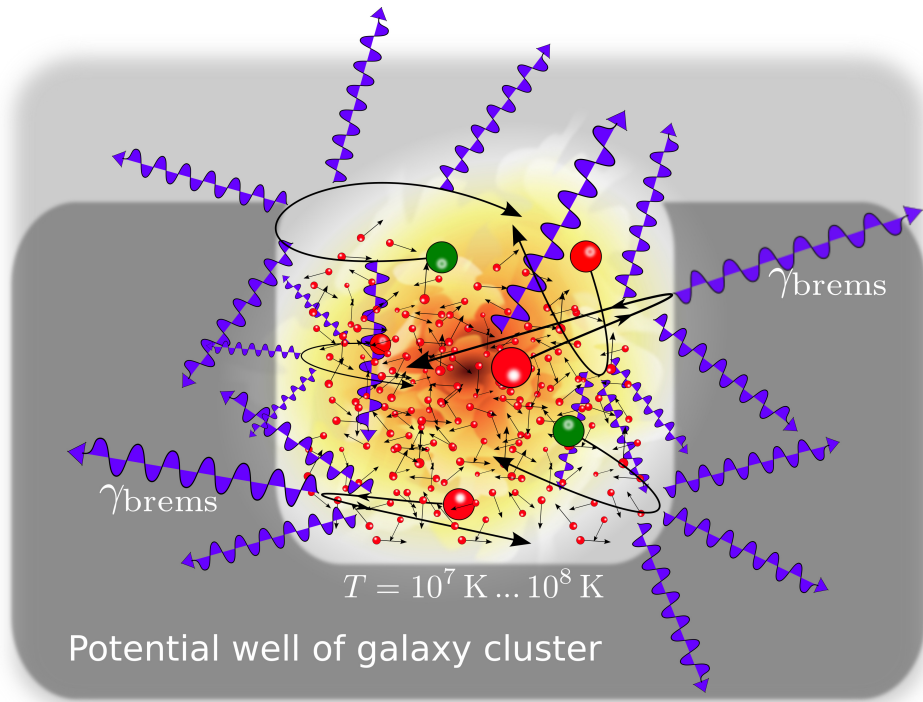


Figure 2.4: The emission of Bremsstrahlung in galaxy clusters

is of order unity. In Eq. 2.12, m_{H} denotes the mass of the hydrogen atom, $\mu \approx 0.6$ is the mean atomic weight of the gas and k_{B} denotes the Boltzmann constant. From $\beta \simeq 1$ one infers that a velocity dispersion of $\sigma_{\text{vec}} = 10^6 \text{ m/s}$ corresponds to a temperature of $T = 10^8 \text{ K}$.

For a more quantitative understanding of the diffuse thermal X-ray emission of galaxy clusters, it is necessary to study the emission of Bremsstrahlung in further detail. A general starting point is the bolometric volume emissivity given in cgs units by

$$j_{\text{X}} = g_{\text{ff}} Z^2 C_{\text{X}} n^2 \sqrt{T}, \quad (2.13)$$

where g_{ff} is the Gaunt factor, Z is the ion charge, n is the ion number density, T is the gas temperature, and

$$C_{\text{X}} = 2.68 \times 10^{-24}, \quad (2.14)$$

in cgs units, if T is measured in keV. Having introduced these basic relations, the remaining task is to specify a model for the gas density which could either stem from theoretical considerations or from measurements. A rather simple, commonly used, axisymmetric model for the gas-density distribution in clusters is

$$n(x) = \frac{n_0}{(1+x^2)^{3\beta/2}}, \quad x \equiv \frac{r}{r_{\text{c}}} = \frac{\theta}{\theta_{\text{c}}}, \quad (2.15)$$

2.2. Observational properties of galaxy clusters

where r_c and θ_c are the physical and angular core radii, preventing the density profile to become singular at the origin. Projecting the X-ray emissivity from Eq. 2.13 along the line-of-sight results in the X-ray surface brightness S_X as a function of the angular radius θ ,

$$S_X(\theta) = \int_{-\infty}^{\infty} j_X dz = \frac{\sqrt{\pi}\Gamma(3\beta - 1/2)}{\Gamma(3\beta)} \frac{Z^2 g_{\text{ff}} C_X r_c n_0^2 \sqrt{T}}{[1+x^2]^{3\beta-1/2}}. \quad (2.16)$$

In the derivation of the above relation, Eq. 2.13 and 2.15 have been combined under usage of the assumption of isothermality (T does not change with radius) of the cluster. By measuring the surface-brightness profile, one can infer the best-fit parameters for the density profile 2.15, namely the slope β and the (angular) core radius θ_c . In general, models of the type 2.15, also known as *beta models*, describe the observed surface-brightness profiles of clusters quite well in the radial range of $\sim [r_c, 3r_c]$ with $\beta_{\text{fit}} \approx 2/3$. For low mass clusters, it has been reported that lower values of β are preferred (Finoguenov et al. 2001; Sanderson et al. 2003).

In order to determine the missing normalisation constant n_0 in Eq. 2.15, one uses the X-ray luminosity given by

$$L_X = 4\pi \int_0^{\infty} j_X r^2 dr = 4\pi r_c^3 Z^2 g_{\text{ff}} C_X \sqrt{T} n_0^2 \frac{\sqrt{\pi}\Gamma(3\beta - 3/2)}{4\Gamma(3\beta)}, \quad (2.17)$$

together with a spectral determination of the temperature T . By integrating the density profile, one obtains the total mass M_X of the X-ray gas enclosed in spheres of radius R

$$M_X(R) = 4\pi\mu m_p \int_0^R n(r)r^2 dr, \quad (2.18)$$

which is a rather complicated function for general β , unless the commonly used and measured value $\beta = 2/3$ is used. In this case, a simple analytic solution which can be written as

$$M_X(R) = 4\pi r_c^3 \mu m_p n_0 \left(\frac{R}{r_c} - \arctan \frac{R}{r_c} \right). \quad (2.19)$$

Due to the fact that the density falls off $\propto r^{-2}$ for $\beta = 2/3$ and $r \rightarrow \infty$, this relation formally diverges for $R \rightarrow \infty$, introducing the need of a cut-off radius for the mass integration.

An alternative way for mass estimates from X-ray observations is to use directly the relations from Eq. 2.5 and to combine them with the density profile introduced above. Under the assumption of isothermality, one arrives then at

$$M(r) = \frac{3\beta r k_B T}{G\mu m_p} \frac{x^2}{1+x^2}. \quad (2.20)$$

Chapter 2. Galaxy clusters

such that the cluster mass is determined from the logarithmic density slope of the X-ray surface brightness

$$\frac{d \ln \rho}{d \ln r} = \frac{d \ln n}{d \ln r} = -3\beta \frac{x^2}{1+x^2}, \quad (2.21)$$

and the cluster temperature T .

Even though, in reality, clusters are rarely observed to be in hydrostatic equilibrium, exhibiting features like cool cores, cold fronts and X-ray cavities, the above considerations revealed themselves as useful working hypothesis to gain deeper insights into cluster physics.

2.2.3 Microwaves

Apart from observing clusters in the optical and X-ray bands, there is a third frequency regime, namely the microwaves, where galaxy clusters can be observed. The physical effect that allows this is based on fact that CMB electrons passing the hot ionised intra-cluster medium (ICM) will experience inverse Compton collision with hot electrons, as it is shown in Fig. 2.6, causing distortions in the observed spectra of the emergent radiation. First calculations towards this direction were done by Weymann (1965, 1966), but the first application to clusters and the derivation of the spectral shape of the distortions have been done by Sunyaev & Zeldovich (1972, 1980) some years later. One thus currently refers to this effect as the (thermal) *Sunyaev-Zel'dovich (SZ) effect*.

The physical origin of this effect is accessible by rather simple reasoning, starting from the notion that Compton scattering couples two energy reservoirs. On one side, there is the thermal energy stored in the ICM and on the other hand there is the rather cold CMB. Due to the weakness of the Compton interaction and the diluteness of the ICM, both reservoirs can not be in thermal equilibrium, since the relaxation time for reaching the same temperatures is by far longer than a Hubble time. We therefore expect a net energy transfer from the hot ICM to the cold CMB, and in fact one observes variations of the order of 10^{-4} towards the direction of clusters. The peculiar spectral

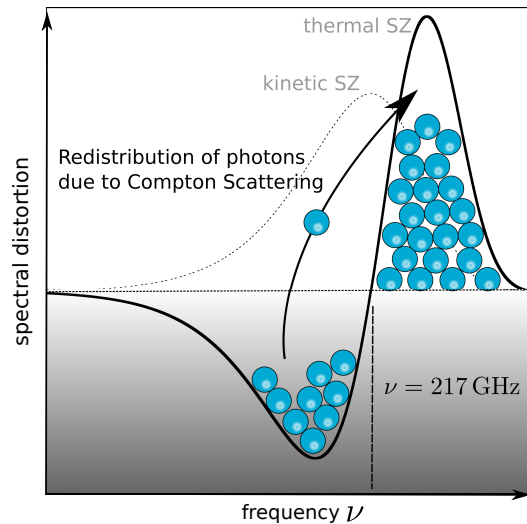


Figure 2.5: Frequency dependence of the SZ effect, both thermal and kinetic, and schematic redistribution of CMB photons (blue balls) due to Compton scattering

2.2. Observational properties of galaxy clusters

signature, as shown by the solid black curve in Fig. 2.5, is caused by removing low energy photons from the line-of-sight and scattering-in of high energy photons into it. Interestingly this particular spectral shape, is independent of the redshift of the galaxy cluster, as discussed further below.

For a more quantitative analysis, the effect of Compton scattering on the photon spectrum has to be calculated, leading to the *Kompaneets equation* (Kompaneets 1957), which is a quantum mechanical extension of the Fokker-Planck equation. It connects the phase space occupation number $n(\omega)$ with the photon energy $\hbar\omega \equiv h\nu$ and turns out to be

$$\dot{n} = \left(\frac{\sigma_T n_e \hbar}{m_e c^2} \right) \frac{1}{\omega^2} \frac{\partial}{\partial \omega} \left\{ \omega^4 \left[n(n+1) + \frac{k_B T_e}{\hbar} \frac{\partial n}{\partial \omega} \right] \right\}. \quad (2.22)$$

Here m_e , T_e and n_e denote respectively the mass, temperature and density of the electrons and σ_T is the Thompson cross section. Using the fact that the ICM is so dilute that for each photon only one scattering event will take place at most, the Kompaneets equation yields a linear change in the phase space occupation number $n(\omega)$, given by

$$\Delta n = y \frac{1}{v^2} \frac{\partial}{\partial v} \left(v^4 \frac{\partial n}{\partial v} \right), \quad (2.23)$$

where y is the *Compton-y parameter*

$$y(\theta) = \frac{k_B \sigma_T}{m_e c^2} \int n_e T_e dl, \quad (2.24)$$

being the line-of-sight integral of the product of the electron density n_e and the electron temperature T_e , i.e. the electron pressure. Since the CMB can be considered to have a perfect black-body spectrum (Mather et al. 1990), the best one we observe in nature, one inserts a Planckian spectral distribution for the CMB $S(x) = S_0 x^3 / (\exp(x) - 1)$ with the flux density $S_0 = 22.9 \text{ Jy/arcmin}^2$ resulting in the flux change $S_Y/S_0 = \Delta n/n$

$$S_Y(x) = y S_0 \frac{x^4 \exp}{(\exp(x) - 1)^2} \left[x \frac{e^x + 1}{e^x - 1} - 4 \right], \quad (2.25)$$

given as a function of the dimensionless frequency $x = h\nu / (k_B T_{\text{CMB}})$. As mentioned before, the SZ-effect redistributes photons from the Rayleigh-Jeans part of the Planck spectrum to the Wien regime, giving rise to the unique spectral signature shown in Fig. 2.5. For frequencies below $x = 3.83 \rightarrow \nu = 217 \text{ GHz}$, clusters are observed, with respect to the CMB, as shadows and above this frequency as emitting sources. The relative change in temperature $\Delta T/T$ is accordingly given by

$$\frac{\Delta T}{T}(\theta) = y(\theta) \left(x \frac{e^x + 1}{e^x - 1} - 4 \right), \quad (2.26)$$

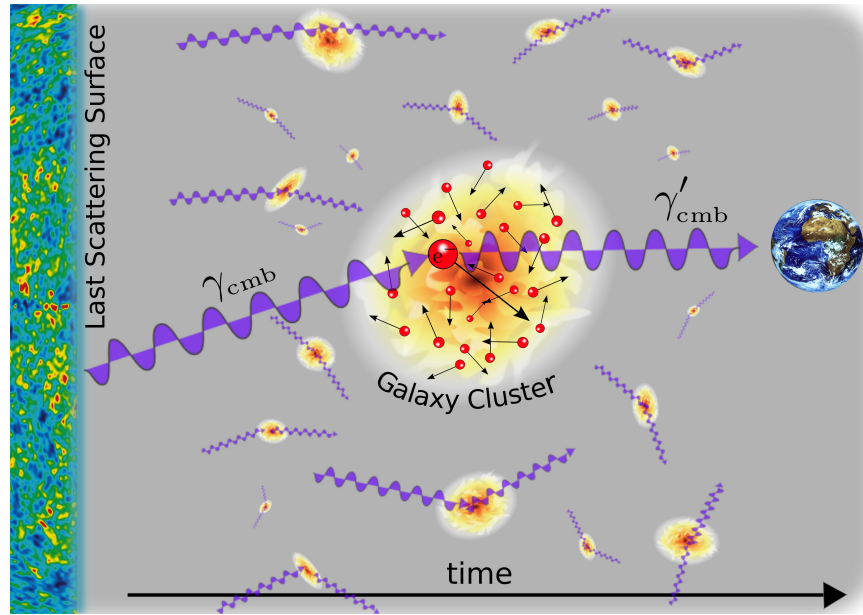


Figure 2.6: The thermal SZ-effect

that together, with its unique spectral signature, the SZ-effect is determined by the Compton- y parameter. However, in applications one is often more interested in the total Comptonisation Y , where y is integrated over the observed cluster surface

$$Y = \int d\Omega y(\theta) \quad (2.27)$$

$$= D_A^{-2}(z) \frac{k_B \sigma_T}{m_e c^2} \int dV n_e T_e, \quad (2.28)$$

which can also be rewritten as an integral over the cluster volume, where D_A denotes the angular diameter distance of the observed cluster at given redshift z . For the case of isothermality, the integrated Comptonisation is given by

$$Y = \frac{k_B T_e}{m_e c^2} \frac{\sigma_T}{D_A^2} N_e, \quad (2.29)$$

where N_e denotes the total number of thermal electrons within the cluster, being fully determined by the cluster mass M_{cl} via

$$N_e = \left(\frac{1 + f_H}{2m_p} \right) f_{gas} M_{cl} \quad (2.30)$$

for a known baryonic gas mass fraction f_{gas} and hydrogen fraction f_H , where m_p stands for the proton mass. For the first we assume throughout this work the cosmic value $f_{gas} = 0.168$ and for f_H the generic value $f_H = 0.76$.

2.2. Observational properties of galaxy clusters

In the considerations done so far, it was always assumed that we are dealing with unordered thermal motion within the ICM and bulk flows or peculiar velocities of the cluster with respect to the CMB were neglected. In the case of a moving cluster, an observer in the cluster rest-frame would observe a bipolar pattern in the CMB and thus the direction dependence of the Compton scattering would cause an energy transfer from the kinetic energy of the cluster to the CMB photons. This effect is usually referred to as *kinetic Sunyaev Zel'dovich effect* and the flux change is given by

$$S_W(x) = wS_0 \frac{x^4 \exp}{(\exp(x) - 1)^2} \quad \text{with} \quad w = \frac{\sigma_T}{c} \int dz n_e v_r, \quad (2.31)$$

where v_r is the radial component of the cluster velocity with respect to the CMB frame. Analogously to Eq. 2.27, one can define $W = \int d\Omega w$ for the kinetic effect. In Fig. 2.5 the dashed line shows the spectral shape of the kinetic effect.

In recent years, the SZ effect gained growing popularity as a potentially sound tool for the detection of galaxy clusters. A very appealing feature is that the effect is redshift independent, since in the dimensionless frequency $x = h\nu/(k_B T_{\text{CMB}})$, T_{CMB} and the frequency ν drop with $\propto 1/a$ so that the spectral shape is preserved for all redshifts. Due to this unique shape, multi-band observations should be ideally tailored to find large amounts of galaxy clusters. In Chap. 7, the validity of this hypothesis will be studied in further detail.

Zoo: *An excellent place to study the habits of human beings.*

Evan Esar (1899-1995)

3

The zoo - Cosmological models

Cosmology became in the last decade a flourishing branch of astrophysics, with growing observational efforts which provided the scientists with overwhelming amounts of data about the structure of our Universe, data supporting the theory that our Universe is recently undergoing an accelerated expansion. Nonetheless, up to this moment we cannot rule out a plethora of phenomenological or ad-hoc models alternative to the simplest one, namely the standard Λ CDM cosmology. The models discussed in this work try to explain the late-time acceleration by the presence of a smooth and slowly varying component, known as dark energy, which can be quantified by an equation-of-state parameter, $w(a)$, and formulated in the framework of general relativity. In the course of my thesis, I will discuss what observational signatures some of these models could leave behind in the process of the formation of structure. Therefore I briefly introduce in this chapter “the zoo” of models I dealt with and refer to them as it becomes necessary in what comes later. The selection of the models is mainly based on works by Szydlowski et al. (2006) and Jennings et al. (2010).

3.1 Λ CDM - The cosmological standard model

Introduced already in the beginning of this work (see Sect. 1.1), the simplest model consistent with the observed data explaining the late-time accelerated expansion of the Universe (Riess et al. 1998; Perlmutter et al. 1999) has a cosmological constant, with equation-of-state parameter $w = -1$ independent of time. Due to the constancy, the contribution of the cosmological constant starts dominating only recently and becomes rapidly negligible towards higher redshifts, as depicted in Fig. 1.1. Thus, at high redshifts, the Universe behaves as a matter-dominated Einstein-de Sitter (EdS) Universe. Despite conceptual problems associated with it, it is currently the simplest model fitting virtually all available observational data. We shall thus assume a spatially flat Λ CDM model as a reference model, since observations suggest negligible spatial curvature. However, we will also consider finite curvature, even if this parameter, according to the current limits, is quite small.

3.2 Quintessence models

The ancient Greeks believed that, in addition to the known four elements (earth, air, fire and water), the Universe beyond Earth is permeated by a pure “fifth element” (called *quinta essentia* in Latin), accounting for the motion of the celestial objects.

In analogy to this quintessence, in modern cosmology a fifth dynamical component, in addition to baryons, leptons, photons and dark matter, is needed to describe the evolution of our Universe. Further details can be found e.g. in Ratra & Peebles (1988); Wetterich (1988); Ferreira & Joyce (1998); Copeland et al. (2006) and Linder (2008). This fifth component is associated with a scalar field Q rolling down a potential $V(Q)$ where the action, including radiation and pressureless matter, is given by

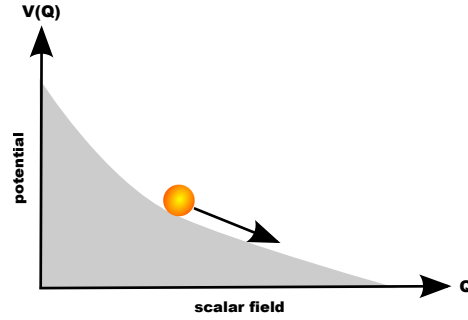


Figure 3.1: Schematic for a scalar field Q slowly rolling down the potential $V(Q)$.

$$S = \int d^4x \sqrt{-g} \left(-\frac{R}{16\pi G} + \mathcal{L}_{m+r} + \frac{1}{2} g^{\mu\nu} \partial_\mu Q \partial_\nu Q - V(Q) \right), \quad (3.1)$$

where g is the determinant of a spatially flat Friedmann-Lemaître-Robertson-Walker (FLRW) metric tensor $g_{\mu\nu}$, R is the Ricci scalar and \mathcal{L}_{m+r} is the Lagrangian density of matter and radiation. Minimising the action with respect to the scalar field Q yields the equation of motion

$$\ddot{Q} + 3H\dot{Q} + V'(Q) = 0 \quad (3.2)$$

where the prime denotes the derivative with respect to Q . By choosing the appropriate potential $V(Q)$, one can evolve the equations and obtain the pressure and the energy density and therefore the equation-of-state

$$w \equiv \frac{P}{\rho} = \frac{\frac{1}{2}\dot{Q}^2 - V(Q)}{\frac{1}{2}\dot{Q}^2 + V(Q)}. \quad (3.3)$$

From the numerator it can be easily seen that if the field is rolling slowly enough, meaning that the kinetic term is smaller than the potential one, one obtains a negative pressure and therefore a negative equation-of-state. In fact it can be shown that $w < -1/3$ is needed for an accelerated expansion.

The motivation to extend the standard cosmology with a dynamical, self-interacting scalar component is mainly to address the “coincidence problem”. Due to the fact that quintessence can couple to other forms of energy, models can always be constructed such that the quintessence component adjusts itself to be comparable to the matter component today. Even though there is currently no evidence for it,

3.2. Quintessence models

Table 3.1: Potentials $V(Q)$ for the different quintessence models. For the details of the individual potentials, the reader is referred to the original works cited in the third column.

Model	Potential	Authors
INV1	$V(Q) = \Lambda^{\alpha+4}/Q^\alpha$	Corasaniti & Copeland (2003)
INV2	$V(Q) = \Lambda^{\alpha+4}/Q^\alpha$	Sanchez et al. (2009)
SUGRA	$V(Q) = \Lambda^{\alpha+4}/Q^\alpha e^{\kappa/2Q^2}$	Brax & Martin (1999)
CNR	$V(Q) = M^4 e^{\alpha(\kappa Q)^\beta}$ $M = \Lambda^{5+\beta} \kappa^{1+\beta} (\beta^2 - 3)/2$	Copeland et al. (2000)
2EXP	$V(Q) = M_{\text{Pl}}(e^{\alpha\kappa(Q-A)} + e^{\beta\kappa(Q-B)})$	Barreiro et al. (2000)
AS	$V(Q) = V_p e^{-\lambda Q}$ $V_p = (Q-B)^\alpha + B$	Albrecht & Skordis (2000)

quintessence might fit the observational data better than the cosmological constant, rendering our view of cosmic history new.

Another important aspect that should be mentioned is that naturally quintessence has to be, by general covariance, spatially inhomogeneous due to the fact that it is time-evolving. However, if the equation-of-state is slowly varying, it can be shown (see e.g. Caldwell (2000)) that the Compton wavelength of the quintessence field is comparable to the Hubble horizon, implying that fluctuations on sub-horizon scales are damped away. This is the case for all models considered in this work, such that in the following, dark energy will be considered to be a smooth non-clustering component, with the sound speed given by $c_s = \sqrt{w}c$.

3.2.1 Classification of the used models

In this work, six different quintessence models were studied, following the selection by Jennings et al. (2010) to which the reader is referred for further details. In general, all these models can be divided in two broad subclasses:

Tracking scalar fields Tracker fields (Steinhardt et al. 1999) avoid fine-tuning of the initial conditions of the scalar field to ensure a given energy density and equation-of-state at present time. They are characterised by a scalar field Q rolling down its potential $V(Q)$, as depicted in Fig. 3.1, reaching an attractor solution. An interesting feature is that the scalar field tracks the dominant component of the cosmic fluid.

Scaling fields This class of fields (Halliwell 1987; Wands et al. 1993; Wetterich 1995) instead keeps the ratio between the density of the scalar field and that of the background constant. Scaling fields can suffer from problems to match simultaneously observational constraints at early times and produce acceleration at late time.

Excluding the models with early dark energy, four models studied in this work fall into the first classification, starting from the inverse power-law potential models

Chapter 3. The zoo - Cosmological models

INV1 and INV2 (Corasaniti & Copeland 2003; Sanchez et al. 2009; Corasaniti 2004), to the supergravity inspired model SUGRA (Brax & Martin 1999) and the CNR model introduced by Copeland et al. (2000), who included supergravity corrections to quintessence. In addition to these, two models belonging to the second category of scaling fields have been added as well, namely the exponential potential model 2EXP by Barreiro et al. (2000), and the AS model introduced by Albrecht & Skordis (2000). The actual form of $V(Q)$ for these models is given in Tab. 3.2. For further details about the individual models, the reader is referred to the papers cited in the third column.

3.2.2 Parametrisation of the models

Having classified the quintessence models, it is necessary to parametrise them in a common way so that they can be easily used in a cosmological analysis. The starting point of these considerations is the continuity equation

$$\dot{\rho} + 3H \left(\rho + \frac{P}{c^2} \right) = \dot{\rho} + 3H(1+w)\rho = 0, \quad (3.4)$$

which is solved by

$$\rho = \rho_0 e^{-3 \int_1^a [1+w(a')] d \ln a'}. \quad (3.5)$$

and therefore the expansion function reads

$$E(a) = \sqrt{\frac{\Omega_{m,0}}{a^3} + \frac{\Omega_{K,0}}{a^2} + \Omega_{Q,0} \exp \left(-3 \int_1^a \frac{1+w(a')}{a'} da' \right)}. \quad (3.6)$$

The remaining task is to find a common description of the equation-of-state parameter without specifying the individual potential $V(Q)$ directly. One parametrisation having this feature has been proposed by Corasaniti & Copeland (2003), based on the notion that $w(a)$ can be described by its value during the different cosmic epochs, namely radiation-dominated w_r , matter-dominated w_m and dark energy domination w_0 , corresponding to the present-day value, and in addition to this by the width of transition $\Delta_{r,m}$ between the different regimes and the scale factor $a_{r,m}$ they occur at. Specifying for the matter-dominated era, Corasaniti & Copeland (2003) have shown that

Table 3.2: Parameter values for the quintessence models.

Model	w_0	w_m	a_m	Δ_m
INV1	-0.4	-0.27	0.18	0.5
INV2	-0.79	-0.67	0.29	0.4
SUGRA	-0.82	-0.18	0.1	0.7
CNR	-1.0	0.1	0.15	0.016
2EXP	-1.0	0.01	0.19	0.043
AS	-0.96	-0.01	0.53	0.13

$$w(a) = w_0 + (w_m - w_0) \frac{1 + e^{\frac{a_m}{\Delta_m}}}{1 + e^{-\frac{a-a_m}{\Delta_m}}} \frac{1 - e^{-\frac{a-1}{\Delta_m}}}{1 - e^{\frac{1}{\Delta_m}}} \quad (3.7)$$

3.2. Quintessence models

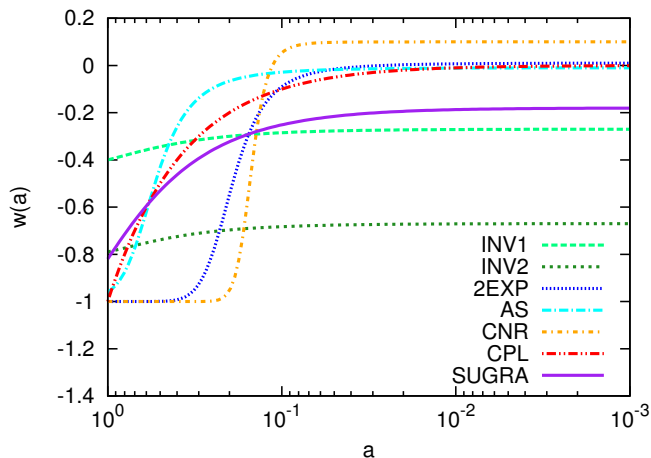


Figure 3.2: Time evolution of the equation-of-state parameter as a function of the scale factor a for the different quintessence models studied in this work. The light-green dashed and the dark-green, short-dashed curves represent the INV1 and INV2 models, respectively; the blue, dotted curve the 2EXP model, the cyan, dot-dashed curve the AS model, the orange, dot-short-dashed and red, dot-dot-dashed curves the CNR and the CPL models, while the solid, violet curve represents the SUGRA model.

provides an excellent match to the exact equation-of-state. This parametrisation will be of great value when it comes to studying the spherical collapse and it will be extensively used in Chap. 8. Table 3.2 gives the values of the parameters a_m , Δ_m , w_m and w_0 as used in this work for the models introduced above. And in Fig. 3.2, the equation-of-state is shown as a function of the scale factor a for the studied quintessence models, including the CPL model (Chevallier & Polarski 2001; Linder 2003) based on an a phenomenological fit of $w(z)$ given by

$$w(z) = -1 + \frac{z}{1+z}, \quad (3.8)$$

as a function of redshift from which it is evident that it mimics a cosmological constant at low redshift, whereas at early times $w(z)$ grows up to zero. The colour-coding of the line-styles for the individual models is given in Fig. 3.2 itself. For the inverse power-law potentials INV1 and INV2, we have w_0 -values of -0.4 and -0.79 respectively, where the former is used in illustrative way and the latter is better in agreement with observational constraints from CMB, SNe and large-scale structure data (Sanchez et al. 2009). Both models show a gentle decrease of $w(a)$, being almost constant, except at late times. The other models instead show a very large change in w at late times, reaching a constant value quite soon in cosmic history. Furthermore, the values of the equation-of-state parameter at $a = 1$ cover a broad range, from $w = -0.4$ for the INV1 model till $w = -1$ for essentially all others.

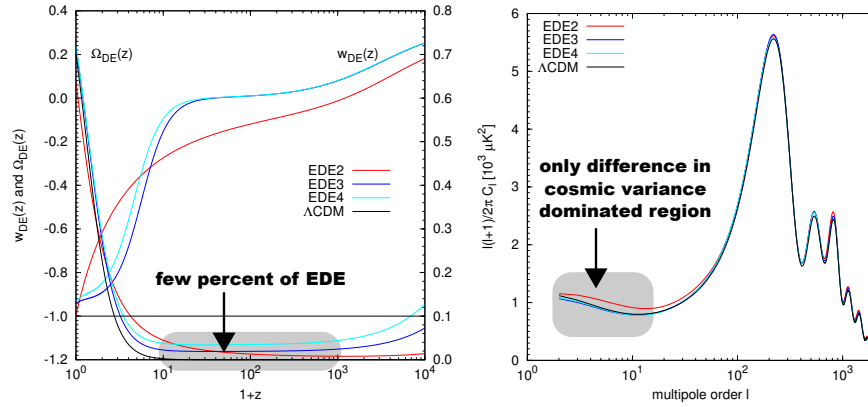


Figure 3.3: Collection of some properties of the considered EDE cosmologies. The first panel on the left shows the redshift evolution of the equation-of-state parameter $w(z)$ (left axis) and of the dark energy density $\Omega_{\text{DE}}(z)$ (right axis). The panel on the right shows the CMB power spectra as computed with CMBEASY (Doran 2005). As a reference the standard ΛCDM models has been added to both figures.

3.2.3 Early dark energy models

This subsection is devoted to introduce a particular class of dark energy models, for which the amount of dark energy does not vanish at early times but keeps a constant level of a few percent, and which are therefore referred to as early dark energy (EDE) models. These models, for which simple parametrisations have been introduced by Wetterich (2004) and by Doran & Robbers (2006), are of special interest, since my thesis was supposed to study in detail their effects on the formation of structure and their observability.

General features

For the simple parametrisation of EDE models mentioned above, three cosmological quantities are sufficient to determine fully the model: the present dark energy density $\Omega_{\text{DE},0}$, the present equation-of-state parameter $w_{\text{DE},0}$ and the averaged value of the dark energy density during the era of structure formation,

$$\bar{\Omega}_{\text{DE},\text{sf}} \equiv -(\ln a_{\text{eq}})^{-1} \int_{\ln a_{\text{eq}}}^0 \Omega_{\text{DE}}(a) d \ln a, \quad (3.9)$$

where a_{eq} denotes the scale factor at matter-radiation equality. Following Doran & Robbers (2006), the equation-of-state parameter, assuming a flat Universe, is implicitly given by

$$\left[3w_{\text{DE}}(a) - \frac{a_{\text{eq}}}{a + a_{\text{eq}}} \right] \Omega_{\text{DE}}(a)(1 - \Omega_{\text{DE}}(a)) = -\frac{d\Omega_{\text{DE}}(a)}{d \ln a}, \quad (3.10)$$

3.2. Quintessence models

Table 3.3: Key cosmological parameters of the used EDE models, as obtained from a MCMC analysis by Georg Robbers.

Parameter	EDE2	EDE3	EDE4
$\Omega_{m,0}$	0.364	0.284	0.282
$\Omega_{DE,0}$	0.636	0.716	0.718
$\bar{\Omega}_{DE,sf}$	0.04	0.033	0.048
h	0.62	0.686	0.684
σ_8	0.78	0.715	0.655
n_s	0.99	0.978	0.976
w_0	-0.99	-0.942	0.934

where $\Omega_{DE}(a)$ is the time evolution of the dark energy component

$$\Omega_{DE}(a) = \frac{\Omega_{DE,0} - \bar{\Omega}_{DE,sf}(1 - a^{-3w_0})^\gamma}{\Omega_{DE,0} + \Omega_{m,0}^{3w_0}} + \bar{\Omega}_{DE,sf}(1 - a^{-3w_0})^\gamma. \quad (3.11)$$

Here γ is a shape parameter controlling the importance of the terms containing the averaged value of the dark energy density during the era of structure formation $\bar{\Omega}_{DE,sf}$. In this work $\gamma = 1$ was always assumed. The resulting evolution of the equation-of-state and the dark energy fraction are shown in the left panel of Fig. 3.3 for three models considered, for which the parameters are given in Tab. 3.3. The models were obtained from a MCMC analysis performed by Georg Robbers, such that they would be in agreement with observations from CMB, large-scale structure and supernovae, despite having different parameters than the concordance model. A non-vanishing dark energy density $\Omega_{DE}(z)$ through long periods of the cosmic evolution can be achieved by allowing that $w_{DE}(z)$ rises above zero, which is a common feature of all models depicted in Fig. 3.3. In the left panel, the grey shaded area has been added to depict the period of the presence of EDE, where the energy densities for the EDE models do not vanish and are almost constant at $z > 10$, whereas for Λ CDM almost no contribution is left. Additionally, it is clearly evident that all of the three models of EDE belong to the class of tracking models, as $w_{DE}(z)$ follows the dominant component during cosmic evolution, first radiation, then matter and finally a cosmological constant. This is more pronounced for the EDE 3 and 4 cases and less for the EDE 2 model.

Current observational constraints from SN Ia, LSS and CMB data allow for a $\bar{\Omega}_{DE,sf}$ on the percent level (Doran et al. 2005, 2007). The panel on the right-hand side of Fig. 3.3 presents the CMB power spectra as computed with CMBEASY (Doran 2005) for all models, showing a surprisingly good agreement with Λ CDM. Only for low multipoles the EDE models differ from the Λ CDM case. This region (see grey shaded area) however is dominated by cosmic variance, such that these deviations are not observable.

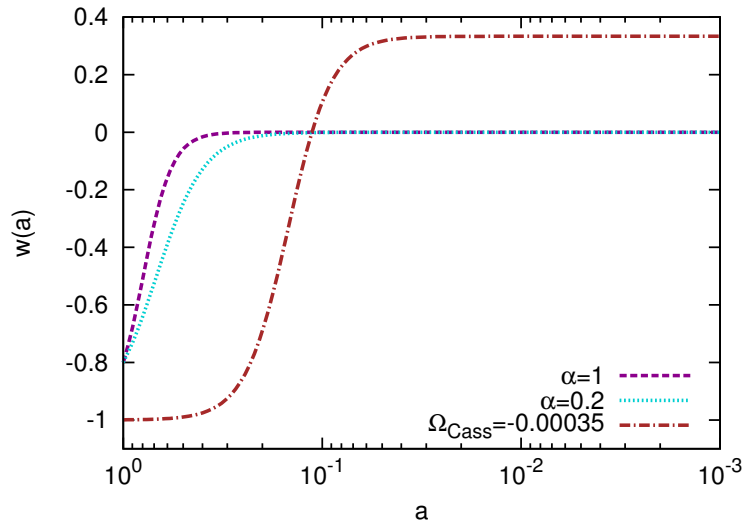


Figure 3.4: Time evolution of the equation-of-state parameter. The (turquoise dotted) magenta dashed curve shows the (generalised) Chaplygin gas while the brown dot-dashed curve represents the model based on the Casimir effect.

Structure formation

The study of structure formation in presence of dark energy has been subject of many studies (Wang & Steinhardt 1998; Doran et al. 2001; Linder & Jenkins 2003; Mota & van de Bruck 2004; Horellou & Berge 2005), and in the case of EDE the non-linear part has been analysed by Bartelmann et al. (2006), who showed that at the high mass end a significant enhancement of the number of clusters at redshifts $z \sim 1$ can be expected. This result has been questioned by different authors (Francis et al. 2009b,a; Grossi & Springel 2009), who did not find such an effect in numerical simulations. Motivated by these findings, the work presented in Chapter 8 has been done, in which the spherical collapse in dark energy cosmologies has been revisited. We found that indeed the collapse and therefore structure formation itself is barely altered in alternative dark energy models. In order of not anticipating the results I will therefore not go into further detail at this point but refer the reader to Chap. 8.

3.3 Chaplygin gas and Casimir effect

An alternative to scalar fields for explaining the current acceleration proceeds by specifying an exotic equation-of-state satisfying the condition for acceleration, $w < -1/3$. One example is provided by the Chaplygin gas, first proposed in aerodynamics and subsequently derived from the action in string theory (Ogawa 2000). It was used in cosmology as a possible alternative to dark energy models by Kamenshchik et al. (2001); Fabris et al. (2002); Szydlowski & Czaja (2004). The

3.3. Chaplygin gas and Casimir effect

equation-of-state of the generalised Chaplygin gas assumes the form

$$P = -\frac{A}{\rho^\alpha}, \quad (3.12)$$

where $A > 0$ and α are constants. The classical Chaplygin gas is recovered for $\alpha = 1$. Using the continuity equation for the generalised Chaplygin gas, one obtains the dependence of the density on the scale factor

$$\rho = \left[A + \frac{B}{a^{3(\alpha+1)}} \right]^{1/(1+\alpha)}, \quad (3.13)$$

where B is an integration constant. The equation-of-state parameter can be written in the form

$$w(a) = -\frac{A}{A + \frac{B}{a^{3(\alpha+1)}}}, \quad (3.14)$$

where $A = -w_0(\Omega_{Q,0}\rho_c)^{1+\alpha}$ and $B = (1+w_0)(\Omega_{Q,0}\rho_c)^{1+\alpha}$. ρ_c is the present critical density and $w_0 = -A/(A+B)$ is the present value of the equation-of-state parameter. We studied the classical Chaplygin gas with $\alpha = 1$ and a generalised version with $\alpha = 0.2$. Both models have $w_0 = -0.8$.

Another possible way to explain the current accelerated expansion is to study quantum properties of the vacuum using the Casimir effect. This effect arises from a change in the zero-point oscillation spectrum of a quantised field when the quantisation domain is finite or the space topology is non-trivial. In a cosmological context, the Casimir effect is relevant if the topology is not simply connected or when compact extra dimensions are involved. In a more general setting, it can be used to study the properties of the vacuum. In this context the contribution given by the Casimir force is scaling like a^{-4} , exactly like relativistic species do.

The expansion function is

$$E(a) = \sqrt{\frac{\Omega_{m,0}}{a^3} + \Omega_{Q,0} - \frac{\Omega_{Cas,0}}{a^4}}, \quad (3.15)$$

where $\Omega_{Cas,0}$ is the density of the Casimir component today. It is possible to interpret this as a time evolution of the dark energy component, one can invert Eq. 3.15 using the general equation

$$w(a) = -\frac{1 + \frac{2}{3}a \frac{d \ln E(a)}{da} - \frac{1}{3} \frac{\Omega_{K,0}}{a^2 E(a)^2}}{1 - \frac{\Omega_{m,0}}{a^3 E(a)^2} - \frac{\Omega_{K,0}}{a^2 E(a)^2}} \quad (3.16)$$

to obtain the equation-of-state parameter

$$w(a) = -\frac{1}{3} \frac{3\Omega_{Q,0}a^4 + \Omega_{Cas,0}}{\Omega_{Q,0}a^4 - \Omega_{Cas,0}}. \quad (3.17)$$

Chapter 3. The zoo - Cosmological models

Here, we shall assume a value of $\Omega_{\text{Cas},0} = -0.00035$ (Godłowski & Szydlowski 2006; Szydlowski & Godłowski 2008).

In Fig. 3.4, we show the time evolution of the Chaplygin (magenta, dashed curve) and of the generalised Chaplygin (turquoise, dotted curve) gas, and in brown, dot-dashed the equation-of-state parameter for the Casimir effect. The two curves representing the generalised Chaplygin gas are very similar: only the initial slope changes with the change of the α parameter.

3.4 Phantom models and topological defects

A better fit to type-Ia supernova data is achieved if one assumes a varying equation-of-state parameter with some phantom crossing at low redshift (Caldwell 2002), or in other words that there $w < -1$. Models fulfilling this condition are called phantom models, and they seriously challenge the foundations of theoretical physics, since they violate several energy conditions. Here, we study five different phantom models, all having a constant equation-of-state parameter. In particular, we focus on the models with $w = -4/3$, $w = -3/2$, $w = -2$, $w = -3$. Certain grand unified theories predict topological defects to have formed in the early Universe: since they rapidly diluted, their abundance should be very low. Here, we consider models with $w = -2/3$.

A satellite has no conscience.

Edward R. Murrow
(1908-1965)

4

The *PLANCK* mission

The satellite mission *PLANCK* (Tauber 2000), part of ESA's Cosmic Vision Programme is the third Medium-Sized Mission (M3) of ESA's Horizon 2000 Scientific Programme. The main mission objective is the imaging of the anisotropies of the cosmic microwave background radiation field over the whole sky, with unprecedented sensitivity ($\Delta T/T \sim 2 \times 10^{-6}$) and angular resolution (down to 5 arcminutes). The data provided by *PLANCK* will help to improve our understanding of several cosmological and astrophysical issues, such as testing theories of the early Universe and the origin of cosmic structure. In this chapter, after a short introduction in Sect. 4.1, the main mission objectives (Sect. 4.2) and the instrument itself (Sect. 4.3) are presented.

4.1 Introduction

PLANCK, named in honour of the German scientist and Nobel Prize laureate Max Planck (1858-1947), originated from the previously proposed missions COBRAS / SAMBA, and was finally selected and approved in late 1996. After the launch had to be postponed several times, the Ariane 5 carrier rocket finally lifted off from the Kourou space centre on 14th May 2009, transporting *PLANCK* into space together with the Herschel satellite. After a transit-time of 50 days, *PLANCK* entered its final orbit around the Second Lagrangian point of the Sun-Earth system (L2), at a distance of 1.5 million kilometres from Earth. *PLANCK* started its routine operations after the end of the commissioning and performance verification phases in mid-August 2009 and is continuously taking data since then. After ESA's advisory bodies approved an extension of

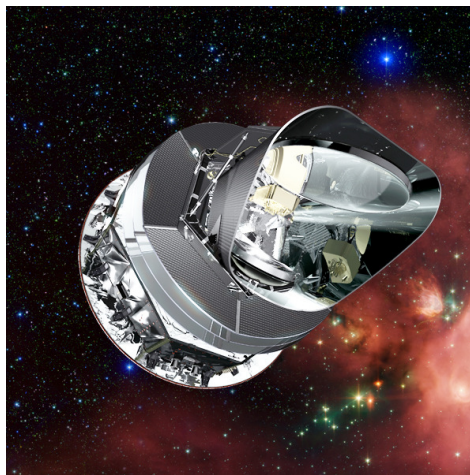


Figure 4.1: Artist impression *PLANCK* orbiting L2, courtesy of ESA/*PLANCK*.

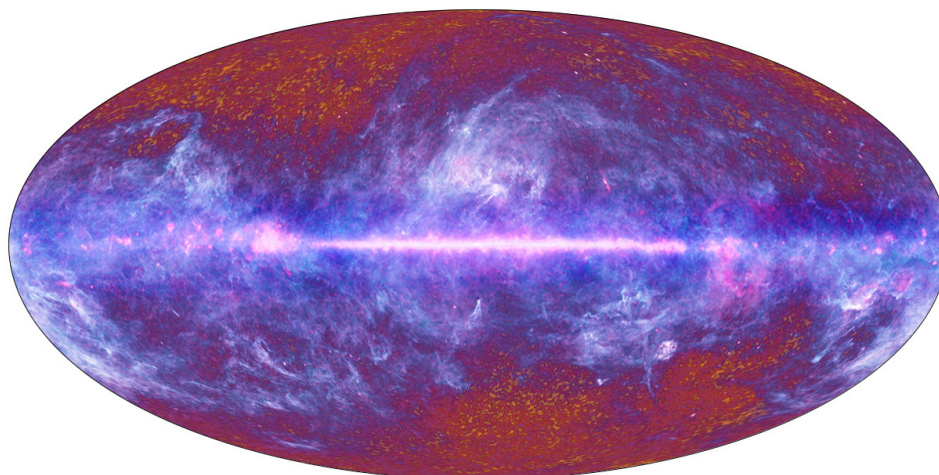


Figure 4.2: *PLANCK*'s first one-year all-sky map, courtesy of ESA/*PLANCK* .

PLANCK's operations by 12 months on 15th January 2010, *PLANCK* has started its third all sky survey on 14 August 2010 after successfully concluding its second survey and is now scheduled to acquire continuously high-quality science data until the end of 2011. A first year all-sky map is shown in Fig. 4.2, which shows how detailed the *PLANCK* maps really are. In the following section, I briefly summarise the primary mission objectives.

4.2 Mission objectives

Even though *PLANCK* main scientific objective is clearly headed towards cosmology, its data are supposed to give us additional insight to a number of astrophysical questions ranging from solar system physics to Galactic studies. The following list summarises the major fields on which strong contributions by *PLANCK* are expected.

CMB Studies Due to its instrument design, as described in Sect. 4.3, *PLANCK* will be able to measure the CMB power spectrum up to multipoles of $\ell \sim 2000$, well beyond the third acoustic peak and deep into the Silk damping regime (see Fig. 1.3). Due to this high accuracy, *PLANCK* will be able to narrow the constraints on several cosmological parameters like density parameters Ω_{m0} , Ω_{Λ} and Ω_b , as well as the spectral index n_s on large scales and the Hubble constant H_0 , on the 1% level. The high quality cartography of the microwave sky will allow further studies of non-Gaussianity, topological defects and other anomalies like the cold-spot Cruz et al. (2005) or the axis of evil (Schwarz et al. 2004; Land & Magueijo 2005) as reported by WMAP.

CMB polarisation *PLANCK* is the most ambitious polarimetry experiment heading towards measuring the CMB polarisation on the full-sky. This highly an-

anticipated data will help to constrain cosmic reionisation scenarios, not very well though, by measuring the power spectra of the polarised components, which will be used as well to break the degeneracies of the cosmological parameters stemming from measurements of the autocorrelation function alone. It is also speculated that a measurement of the tensor modes, namely the B-modes, could be within reach, providing a smoking-gun signature of a stochastic background of gravitational waves.

Thermal SZ effect Apart from studying the primary anisotropies, *PLANCK* was also designed with a strong science case in secondary anisotropies, especially the thermal SZ effect, defining the high-frequency channel design as shown in Fig. 4.3. As discussed in this work, *PLANCK* is expected to deliver a full-sky SZ-detected cluster catalogue comprising around 1000 entries, much less than the formerly anticipated 10^4 clusters. Still, by combining the results with probes in other bands, like X-ray surveys, one can hope to gain insight into the cosmic cluster evolution.

Gravitational lensing Another class of secondary anisotropies are lensing effects, such as CMB lensing, ISW and the Rees-Sciama effect. The sensitivity and angular resolution of *PLANCK* will allow to detect deviations from the CMB power spectrum due to lensing by the large-scale structure. Also corrections stemming from the ISW and RS effect should be found on large scales (see also Fig. 1.3)

Extra-Galactic point sources Supplemental to the full-sky SZ-based cluster catalogue, *PLANCK* will deliver a point source catalogue including a crude estimation of their spectral properties. The catalogue will comprise sources like infra-red and radio galaxies as well as AGNs, QSOs and blazars.

Galactic studies One very important objective of the mission, also in view of the foreground subtraction prior to the CMB analysis, is the determination of the properties of the Galactic dust and synchrotron emission, which will allow to draw conclusions on the Galactic cosmic ray distribution and the Galactic magnetic field.

Solar system studies The list of objects detectable by *PLANCK* does not stop at the Solar System but will include the study of the zodiacal light and the detection of about 100 – 150 asteroids and comets and the measurement of their thermal properties at low frequencies.

4.3 The instrument

The optical design of the *PLANCK* satellite, as depicted in Fig. 4.1, consists of an off-axis tilted Gregorian system, offering the advantages of no blockage and compactness. To avoid significant degradation in the large focal plane array, the

Chapter 4. The PLANCK mission

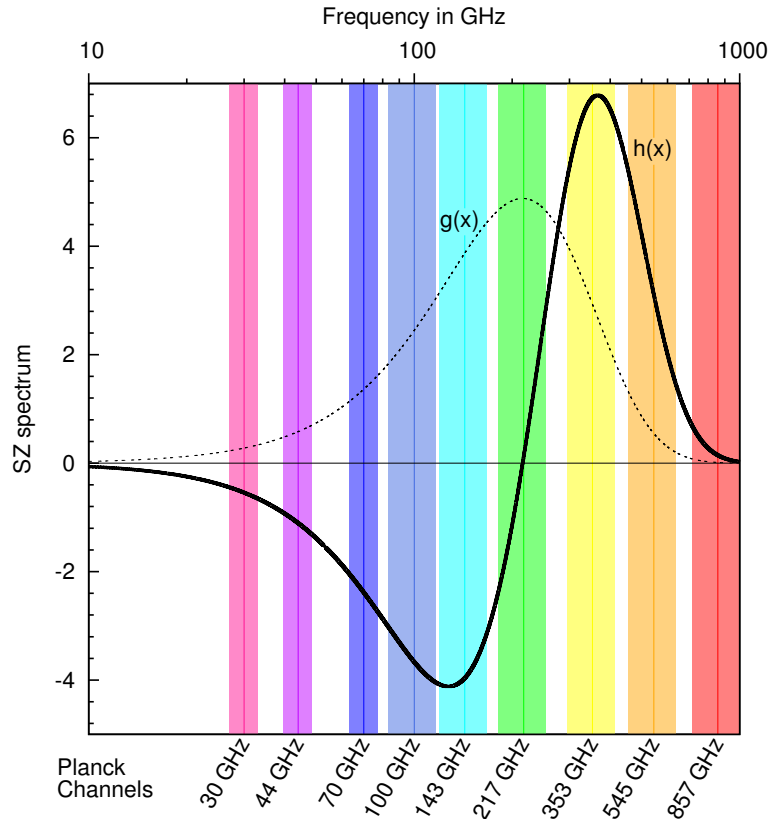


Figure 4.3: Frequency dependence of the SZ effect, both thermal and kinetic, and schematic redistribution of CMB photons (blue balls) due to Compton scattering

eccentricity and tilt angle of the secondary mirror, and the off-axis angle obey the so-called Dragone-Mizuguchi condition minimising at the same time the polarisation effects introduced by the telescope. The primary mirror is an off-axis mounted paraboloid with a diameter of 1.3 m and a focal length of 72 cm. The smaller secondary mirror is 80 cm in diameter having a focal length of 50 cm. Both mirrors were fabricated using Carbon Fibre (CFRP) technology in order to reduce the weight of payload. The total expected wave front error is smaller than $40 \mu\text{m}$.

The second main instrumental part are the detectors operating in nine different channels divided into two different types according to the used detector technologies: The low frequencies instrument (LFI) covering the channels of 30 GHz, 44 GHz and 70 GHz uses high electron mobility transistors operating at 20 K and the high frequency instrument (HFI) operating in the bands between 100 GHz and 857 GHz is an array of bolometers, that have to be cooled down to 0.1 K.

Cooling down the detectors to such low temperature is indeed a challenge to the cryogenic design, which includes several cooling mechanisms built on top of each other, starting with passive, radiative pre-cooling during the transit to L2 down to

4.3. The instrument

Table 4.1: Characteristics of the *PLANCK* channel design: centre frequency ν , frequency window $\Delta\nu$, angular resolution $\Delta\theta$ (FWHM), effective noise level σ_N , fluxes $\langle S_Y \rangle$ (see Eq. 2.25) and $\langle S_W \rangle$ (see Eq. 2.31) generated by the respective Comptonisation of $Y = W = 1 \text{ arcmin}^2$ the corresponding changes in antenna temperature ΔT_Y and ΔT_W . Note that due to *PLANCK*'s symmetric frequency window, the thermal SZ-effect does not vanish entirely at the limiting frequency of $\nu = 217 \text{ GHz}$ (see Schäfer et al. (2006a,b)).

<i>Planck</i> channel	1	2	3	4	5	6	7	8	9
centre freq. ν_0 [GHz]	30	44	70	100	143	217	353	545	857
freq. wind. $\Delta\nu$ [GHz]	3.0	4.4	7.0	16.7	23.8	36.2	58.8	90.7	142.8
ang. res. $\Delta\theta$ [arcmin]	33.5	26.8	13.1	9.2	7.1	5.0	5.0	5.0	5.0
noise. lev. σ_N [mK]	1.01	0.49	0.29	5.67	4.89	6.05	6.80	3.08	4.49
tSZ flux $\langle S_Y \rangle$ [Jy]	-12.2	-24.8	-53.6	-82.1	-88.8	-0.7	146.0	76.8	5.4
kSZ flux $\langle S_W \rangle$ [Jy]	6.2	13.1	30.6	55.0	86.9	110.0	69.1	15.0	0.5
ant. temp. ΔT_Y [nK]	-440	-417	-356	-267	-141	-0.5	38	8.4	0.2
ant. temp. ΔT_W [nK]	226	220	204	179	138	76	18	1.6	0.02

60 K, followed by a hydrogen sorption cooler which provides 20 K to LFI and 18 K to HFI, from which a Joule-Thomson refrigerator driven by mechanical compressors takes over and cools the HFI down to 4 K, and finally an open-loop $^3\text{He}^4\text{He}$ dilution refrigerator provides the HFI working temperature of 0.1 K. The cooling requirements of the HFI detectors limit the mission life-time, due to the limited amount of coolant that can be transported, to a time scale of 30 months (this estimate is however going to be surpassed).

An integral part for the success of the mission is, apart from the instrument itself, the appropriate choice of orbit and sky scanning strategy. In order to control the systematics *PLANCK* will fly in a Lissajous orbit around the L2 point of the Earth-Sun system, spinning at $\sim 1 \text{ rpm}$ around an axis offset by $\sim 85^\circ$ from the telescope central axis. In doing so, the observed sky patch will trace a large circle on the sky, while the spin axis can be continuously pointed in the anti-Sun direction. Since being in orbit around L2, the satellite itself is used to shield the instrument from solar illumination, minimising potentially confusing signals due to thermal fluctuations and straylight entering the detectors through the far-side lobes. This plays a crucial role in the thermal design of *PLANCK*, allowing the required radiative pre-cooling before the active cooling mechanisms set in.

As concluding remark one can state that *PLANCK* being the successor of the COBE and WMAP missions represents the climax of space-borne microwave based missions. We can expect a really strong scientific impact on various astrophysical fields with an emphasis on cosmology. It is highly probable that *PLANCK* is going to be the last mission to measure the CMB power spectrum, possible successors will for sure be polarimetry missions tailored to detect gravitational B-modes.

*It is not down in any map; true
places never are.*

Herman Melville (1819-1891)

5

Semi-analytic mapmaking of full-sky SZ maps for *PLANCK*

In Chapter 4, the main mission objectives of *PLANCK* are presented, one of which is the compilation of a full-sky cluster catalogue selected by the thermal SZ effect, introduced in Sect. 2.2.3. In order to understand what features such a cluster catalogue would have, i.e. what selection function we can expect, what the effect of alternative models to the Λ CDM scenario and so on would be, it is necessary to simulate the satellite observations. This task requires in the case of the SZ observations the creation of a full-sky Compton- y map, which is the topic of this chapter. After a short introduction in Sect. 5.1, the modelling of the mass and redshift distribution of the simulated cluster sample is discussed in Sect. 5.2 and the methodology for placing the clusters in a correlated way on the sky is covered in Sect. 5.5.

5.1 The general idea

As outlined in Schäfer et al. (2006a), one possibility for constructing a full-sky map of the Compton- y parameter is to use large scale pure dark matter cosmological simulations in order to obtain the cluster positions and to simulate additionally individual clusters including gas physics to get the Compton- y signature, or to model the individual clusters by analytic β -profiles, as done by Geisbüsch et al. (2005). Afterwards, everything can be projected on the sphere to obtain a full-sky Compton- y map. Since for arbitrary dark energy cosmologies with a varying equation of state, as introduced in Chap. 3, these numerical simulations are up to now not available and in order to be more flexible, we decided to take the semi-analytic approach that is outlined in the following sections and summarised in the flowchart in Fig. 5.1. In the following, I will discuss step by step how the map construction proceeds and what assumptions have been taken.

5.2 Mass & redshift distribution of the cluster sample

The computation of the mass and redshift distribution of galaxy clusters is the core part of the map construction and is summarised in the second column of Fig.

Chapter 5. Semi-analytic mapmaking of full-sky SZ maps for PLANCK

5.1. The basic information needed is the number of galaxy clusters per mass and redshift bin, that can be estimated using the comoving mass function

$$\frac{dN}{dMdz}(M, z) = \Delta\Omega \frac{dV}{dzd\Omega}(z) \frac{dn}{dM}(M, z), \quad (5.1)$$

giving the cluster number density within the comoving volume element, $dV/dzd\Omega$, for a given solid angle $\Delta\Omega$ on the sky. For the comoving mass function we utilise Eq. 2.11, following the suggestion by Press & Schechter (1974), because it does not depend on numerical simulations that assume a certain cosmological model, like for instance the mass functions proposed by Jenkins et al. (2001) and Sheth et al. (2001). By integrating over the mass and redshift interval of interest, one obtains the number of clusters in the aforementioned bins on the full-sky

$$N_{\Delta M, \Delta z} = 4\pi \int_{\Delta z} dz \int_{\Delta M} dM \frac{dN}{dMdz}(M, z). \quad (5.2)$$

The number of clusters, N , we assign to a bin is then obtained from a Poisson distribution with an average value of $N_{\Delta M, \Delta z}$. In order to create the sample of the N clusters in the given bin $(\Delta M, \Delta z)$, we use a uniform random distribution. The mass bins are equally logarithmically spaced with $\log(\Delta M) = 0.1$ starting at the minimum mass $M_{\min} = 10^{13} h^{-1} M_{\odot}$ up to the upper limit of $M_{\max} = 1 \times 10^{16} h^{-1} M_{\odot}$ and the redshifts range from $z_{\min} = 0.01$ up to $z_{\max} = 3$, where the size of the redshift bin is $\Delta z = 0.02$. Having obtained the mass and redshift distributions of the clusters, the remaining task is to model the individual SZ signal and the spatial distribution on the full-sky.

5.3 Modelling the SZ signal of the individual clusters

After the random realisation of N clusters in ΔM and Δz , both, mass and redshift, for the individual clusters are known. The next step illustrated by the right column in Fig. 5.1 is to model the individual Compton- y signal, which can be derived from the cluster scaling relations. The mass is connected to the virial radius r_{vir} by $M = 4\pi/3 \Delta_V \rho_{\text{crit}} r_{\text{vir}}^3$, where Δ_V is the mean overdensity of a virialised sphere and ρ_{crit} is the critical cosmic density. Solving for r_{vir} gives

$$r_{\text{vir}} = \frac{9.5103}{1+z} \left(\frac{\Omega_{m0} \Delta_V(z)}{\Omega_m(z)} \right)^{-1/3} \left(\frac{M_{\text{cl}}}{10^{15} M_{\odot} h^{-1}} \right)^{1/3} h^{-1} \text{Mpc}. \quad (5.3)$$

Moreover, the application of the virial theorem allows us to connect the mass to the temperature by means of

$$k_B T_e = \beta_T^{-1} (1+z) \left(\frac{\Omega_{m0} \Delta_V(z)}{\Omega_m(z)} \right)^{1/3} \left(\frac{M_{\text{cl}}}{10^{15} M_{\odot} h^{-1}} \right)^{2/3} \text{keV}, \quad (5.4)$$

with the normalisation $\beta_T = 0.75$, being valid under the assumption of hydrostatic equilibrium and isothermality (see e.g. Kaiser 1986; Sarazin 1986). However, since

5.3. Modelling the SZ signal of the individual clusters

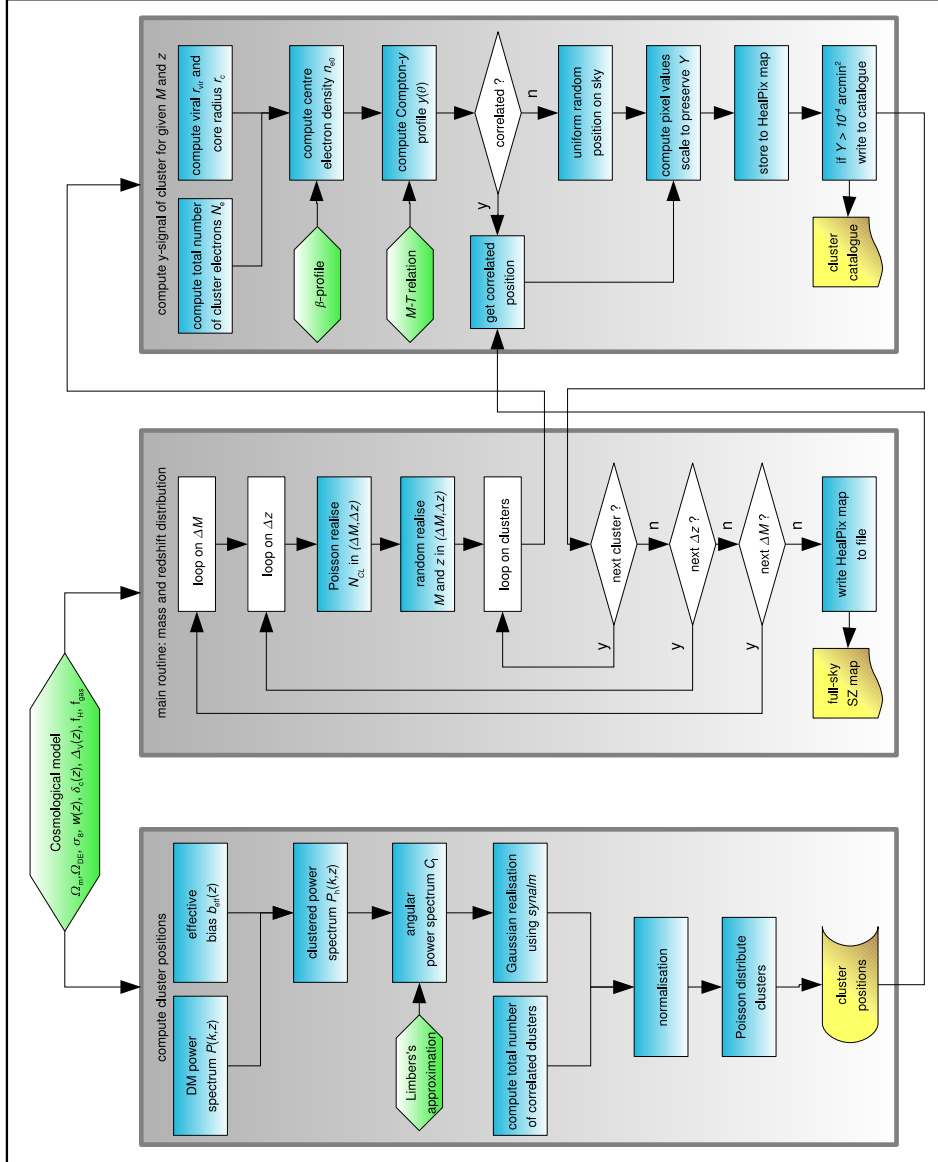


Figure 5.1: Flowchart for the creation of full-sky Compton-y maps. The left column illustrates the process of obtaining the spatial cluster distribution on the sky, the centre one shows the routine for calculating the mass and redshift distributions, and the right column summarises the computation of the Compton-y profile for the individual clusters on the HEALPix sky map. Green boxes illustrate physical assumptions, blue ones computations, white ones stand for algorithmic structures and yellow for results of the routines.

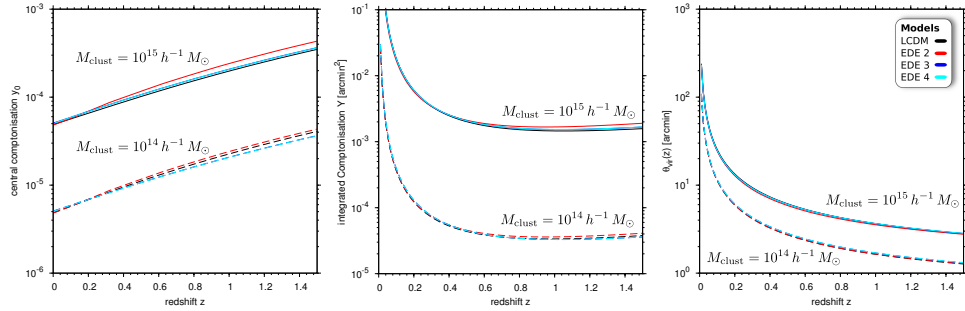


Figure 5.2: Redshift evolution of the individual cluster properties for the Λ CDM and the EDE 2, 3 and 4 models. The left panel shows the central Compton- y parameter y_0 , the middle panel the total Comptonisation Y and the right one the virial angular extent θ_{vir} . Solid lines denote a cluster of $10^{15} h^{-1} M_{\odot}$ and the dashed lines are for a system with $10^{14} h^{-1} M_{\odot}$.

we want to model the SZ signal for a given cluster, it is necessary to model the spatial distribution of the gas component, which is given by the β -profile if hydrostatic equilibrium and isothermality are assumed, see Chap. 2. Therefore, the distribution of the thermal electron density is given by

$$n_e(r) = n_{e0} \left(1 + \frac{r^2}{r_c^2} \right)^{-3/2\beta}, \quad (5.5)$$

where r_c denotes the core radius. The core radius r_c and the virial radius r_{vir} are related (see e.g. Geisbüsich et al. (2005)) by

$$r_c(z) = \xi(z) r_{\text{vir}} = 0.14 (1+z)^{1/5} r_{\text{vir}}. \quad (5.6)$$

Due to the lack of an according relation for the various DE cosmologies, we apply this relation also in these cases. In what follows we chose to set $\beta = 2/3$, delivering good fits to the X-ray surface-brightness of observed clusters.

After these prerequisites have been fulfilled, the first step that has to be taken is to fix n_{e0} by solving the condition $4\pi \int_0^{r_{\text{vir}}} n_e(r) r^2 dr = N_e$ for n_{e0} , which directly leads to

$$n_{e0} = \frac{N_e}{4\pi r_c^3 \left[\frac{1}{\xi} + \arctan(\xi) - \frac{\pi}{2} \right]}. \quad (5.7)$$

Since we do not integrate to infinity, we are utilising a truncated β -profile. By using the assumption of isothermality in Eq. 2.24 and integrating out to r_{vir} , we then obtain for the central Comptonisation

$$y_0 = 2 \frac{k_B T_e}{m_e c^2} \sigma_T r_c n_{e0} \left[\frac{\pi}{2} - \arctan(\xi) \right]. \quad (5.8)$$

5.4. How to tessellate a sphere - HEALPix

In addition, the line-of-sight integrated Compton- y profile is needed and can easily be shown to be given by

$$y(\theta) = 2 \frac{k_B T_e}{m_e c^2} \frac{\sigma_T r_c n_{e0}}{\sqrt{1 + \frac{\theta^2}{\theta_c^2}}} \arctan \sqrt{\frac{\frac{1}{\xi^2} - \frac{\theta^2}{\theta_c^2}}{1 + \frac{\theta^2}{\theta_c^2}}}, \quad (5.9)$$

where $\theta = r/D_A$. In Fig. 5.2 the redshift dependence of some individual cluster properties are shown for the Λ CDM and EDE cases introduced in Subsect. 3.2.3. The three panels show individual properties of the clusters, like central and integrated Comptonisation, as well as angular extent on the sky, where all of these are only mildly affected by the presence of EDE. Having introduced all these relations from above, everything is prepared to populate a full-sky-map with the SZ-signal of the cluster sample. However, this particular point has to be addressed with caution, since one has to think about the pixelisation of a full-sky map, which is covered in the following section.

5.4 How to tessellate a sphere - HEALPix

Assigning values to pixels of equal area is, in contrast to the flat Euclidean case, non-trivial on a sphere. In order to solve this problem the HEALPix tessellation has been proposed (Górski et al. 2005), where the acronym stands for **H**ierarchical **E**qual **A**rea iso**L**atitude **P**ixelisation on the sphere. It was originally developed to address the data processing and analysis needs of the present generation of cosmic microwave background experiments like e.g. *PLANCK* and *WMAP*, but it is also applicable to all problems requiring a discretisation of functions on a spherical domain.

HEALPix tessellates the sphere hierarchically into curvilinear quadrilaterals, starting with the lowest resolution partition comprising 12 base pixels. The resolution of the tessellation increases by division of each pixel into four new ones, as illustrated in Fig. 5.3, where (clockwise from upper-left to bottom-left) the resolution increases by three steps from the base level. This means the sphere is partitioned, respectively, into 12, 48, 192, and 768 pixels. Moreover, the area comprised by each pixel is identical at the same resolution level, which is one the main requirements for our purpose. Apart from this feature,

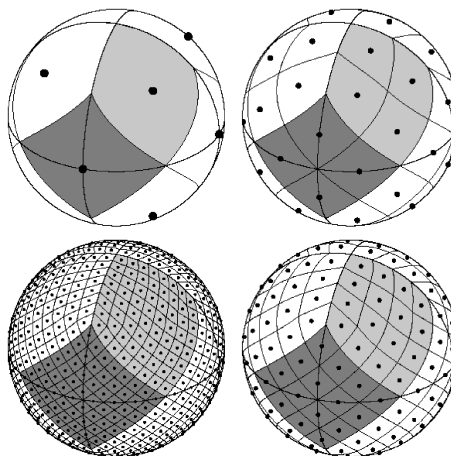


Figure 5.3: HEALPix tessellation scheme for four different values of $N_{\text{side}} = 1, 2, 4, 8$.

Chapter 5. Semi-analytic mapmaking of full-sky SZ maps for PLANCK

Table 5.1: Properties and angular resolution of the relevant HEALPix tessellations (see also Górski et al. (2005)).

k	$N_{\text{side}} = 2^k$	$N_{\text{pix}} = 12N_{\text{side}}^2$	$\theta_{\text{pix}} = \Omega_{\text{pix}}^{1/2}$
0	1	12	58.6°
1	2	48	29.3°
2	4	192	14.7°
3	8	768	7.33°
4	16	3072	3.66°
5	32	12,288	1.83°
6	64	49,152	55.0'
7	128	196,608	27.5'
8	256	786,432	13.7'
9	512	3,145,728	6.87'
10	1024	12,582,912	3.44'
11	2048	50,331,648	1.72'

there is another property of particular importance to CMB analysis, namely the fact that all pixels are distributed on lines of constant latitude, allowing for a significant speed up in the harmonic analysis using spherical harmonics.

Due to the specific geometrical properties, HEALPix supports two different numbering schemes for the pixels. The first one, dubbed the *ring scheme*, numbers the pixels consecutively on the iso-latitude rings from the north to south pole, having the advantage of a rather simple implementation of the spherical harmonic transforms. The second one, dubbed the *nested scheme*, numbers the pixels in tree-like structure, allowing fast nearest-neighbour searches, (Wandelt et al. 1998), and direct implementation of the fast Haar wavelet transform. Table 5.1 summarises the basic properties, like the number of pixels N_{pix} and resolutions θ_{pix} , of the different orders k of the HEALPix tessellation and relates them to the parameter $N_{\text{side}} = 2^k$. As stated before, all pixels cover the same area $\Omega_{\text{pix}} = \pi/(3N_{\text{side}}^2)$. Since all pixels have the same surface area but slightly different shape, the angular resolution is defined as

$$\theta_{\text{pix}} \equiv \sqrt{\Omega_{\text{pix}}} = \sqrt{\frac{3}{\pi} \frac{3600'}{N_{\text{side}}}}. \quad (5.10)$$

In this section, the mathematical features of HEALPix have only been introduced on a very simple basis. In case a more mathematical introduction is required the reader is again referred to Górski et al. (2005).

5.5 Placing the clusters on the sky

With the results from Sect. 5.2 and Sect. 5.3, the machinery for calculating the signatures of the individual clusters in the HEALPix map is complete. First, we calculate the positions of all pixels contained in a disc of an angular size of $\theta_{\text{vir}} = r_{\text{vir}}/D_A$, then we assign the corresponding $y(\theta)$ calculated at the pixel centre, and

5.5. Placing the clusters on the sky

in order to assure consistency with the analytic total Comptonisation Y , we scale all pixels by a factor a given by

$$a = \frac{Y}{\sum_i y_i d\Omega_{\text{pix}}}. \quad (5.11)$$

Here y_i is y in the centre of pixel i and Ω_{pix} is the pixel solid angle. For clusters that are unresolved by the HEALPIX tessellation, we scale Y by the ratio of cluster solid angle to pixel solid angle. The whole procedure is performed for all clusters in the given mass and redshift range and the positions of the centre pixels are obtained as described in the following.

Being able to model the SZ signal for clusters of given mass and redshift, the remaining task is to place them in a realistic way on the sky. Although it is quite popular just to place the clusters randomly on the sky, we decided to take the cluster correlation into account. The scheme for obtaining the spatial distribution on the sky is presented by the left column in Fig. 5.1, where the starting point for computing the angular correlation (or equivalently the angular power spectrum) of the clusters is the cold dark matter power spectrum $P_\delta(k, z)$ from Eq. 1.29 normalised to the present σ_8 value using the window function $\tilde{W}_R(k)$ in k -space. Two popular choices for $\tilde{W}_R(k)$ are the spherical top-hat window function and the Gaussian smoothing, both introduced in Eq. 1.33. In our case, both choices lead to similar results for the angular power spectra.

So far we assumed that the virialised haloes trace the underlying dark matter distribution. Unfortunately, we have to consider that in hierarchical models of gravitational clustering, this relation will be biased. Thus, the next step is to correct for the biasing, $b(M)$, between the haloes of mass M and the dark matter distribution

$$\delta_h = b(M) \delta_{\text{dm}}, \quad (5.12)$$

where δ_h is the halo- and δ_{dm} denotes the dark matter density contrast. For the biasing, we utilise the relation introduced by Mo & White (1996), which is given by

$$b(M, z) = 1 + \frac{1}{\delta_c(z)} \left(\frac{\delta_c^2(z)}{\sigma_R^2 D_+^2(z)} - 1 \right), \quad (5.13)$$

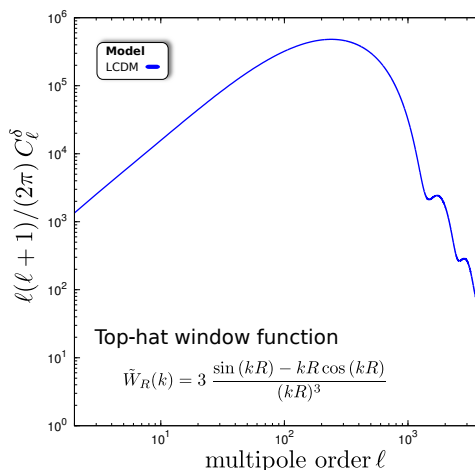


Figure 5.4: Cluster angular power spectrum assuming top-hat window function.

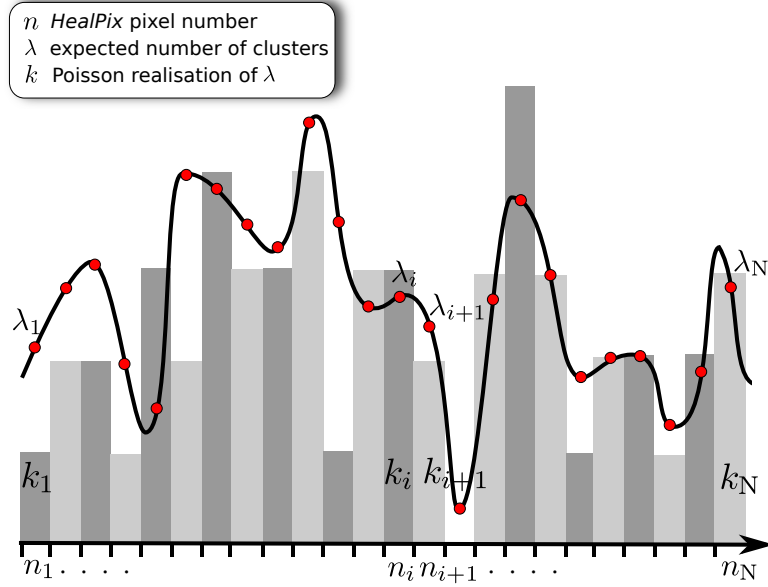


Figure 5.5: Distribution of clusters among the HEALPix pixels. The number k of assigned clusters in a given pixel n is drawn from a Poissonian distribution $f(k; \lambda) = \lambda^k \exp(-\lambda)/k!$, where λ is the expected number of clusters in the given pixel.

introducing the mass dependence on the right-hand side via the smoothing radius R in σ_R . In order to simplify the treatment, it is convenient to introduce the concept of an effective bias defined as

$$b_{\text{eff}}(z) = \frac{\int_{M_{\min}}^{M_{\max}} b(M, z) \frac{dn(M, z)}{dM} dM}{\int_{M_{\min}}^{M_{\max}} \frac{dn(M, z)}{dM} dM}, \quad (5.14)$$

which is a mass weighted integral of $b(M, z)$ over the mass, such that we can write

$$P_h(k, z) = b_{\text{eff}}^2(z) P(k, z). \quad (5.15)$$

So far, everything is defined in 3D-space, but our goal is to obtain the angular cluster correlation with respect to the positions on the sky and to neglect correlations in redshift space. In view of this, it is natural to work with line-of-sight integrated quantities like

$$\delta(\mathbf{n}) = \int_0^{\chi_{\max}} d\chi q(\chi) \delta(\chi \mathbf{n}, \chi), \quad (5.16)$$

which is the line-of-sight integrated density contrast in direction \mathbf{n} for a window function $q(\chi)$, where χ is the comoving distance. The expansion of $\delta(\mathbf{n})$ into spherical harmonics gives

$$\delta(\mathbf{n}) = \sum_{\ell m} \delta_{\ell m} Y_{\ell}^m(\mathbf{n}). \quad (5.17)$$

5.5. Placing the clusters on the sky

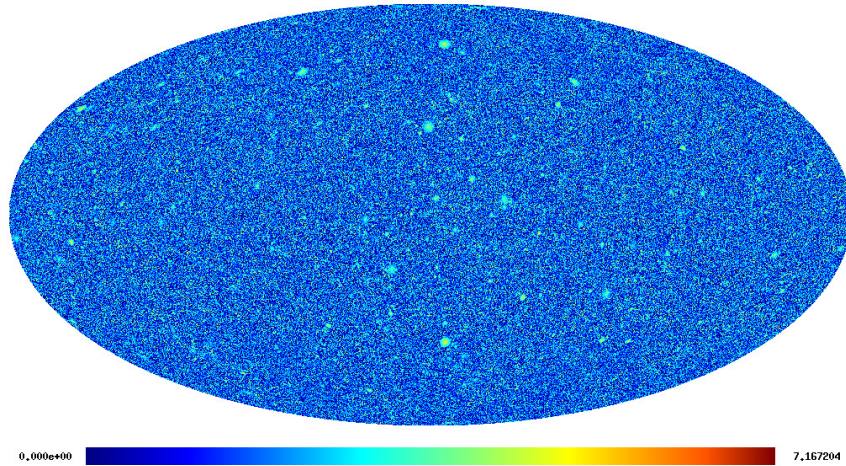


Figure 5.6: Simulated full-sky SZ-map for the EDE 4 model, taking the angular correlation into account. The colour shading indicates the Compton- y parameter, being proportional to $\text{arcsinh}(10^6 y)$, such that the maximum value of 7.167 corresponds to $y = 6.48 \times 10^{-4}$.

Putting all together, and applying Limber's approximation (Limber 1953), namely that correlations of the density contrast along the line-of-sight are negligibly small (Simon 2007), one obtains for the connection between the dark matter power spectrum and the angular power spectrum the relation

$$C_\ell^\delta = \int_0^{\chi_{\max}} d\chi' \frac{q^2(\chi')}{\chi'^2} P_h\left(\frac{\ell}{\chi'}, \chi'\right), \quad (5.18)$$

where $q(\chi)$ denotes the window function, which is for our case a simple step function being non-zero for the intended redshift range.

Given the angular power spectrum C_ℓ^δ from Eq. 5.18, one creates a Gaussian realisation from this power spectrum in the form of spherical harmonic coefficients $a_{\ell m}$ using the *synalm* routine of the *HEALPix* package. Out of the harmonic coefficients, one synthesises the real space map using the *alm2map* routine, representing the probability of having a cluster in a given pixel. After the normalisation of the map, the number of clusters per pixel is drawn from a Poisson distribution (see Fig. 5.5), such that the expectation value of the cluster density equals the mean of the Poisson distribution. Figure 5.6 shows a full-sky Compton- y map for the case of EDE 4 (having an increased number of clusters due to an erroneous low δ_c at low redshifts) with the angular correlation included.

The scheme for creating a full-sky Compton- y map, outlined in this chapter, has been implemented in C++ and requires for a non-standard cosmology (varying $w(a)$) about 48 hours on a 2 GHz-processor and $N_{\text{side}} = 1024$. The final Compton- y is prepared to be fed into the *PLANCK* pipelines for realistic simulations of the

Chapter 5. Semi-analytic mapmaking of full-sky SZ maps for PLANCK

satellite observations that will be covered in more detail in Chap. 6.

Bottom line - What to take away

- *PLANCK* has a strong science case in secondary CMB anisotropies, particularly the compilation of a SZ-selected cluster catalogue. Inspired by the question how and if *PLANCK* could constrain alternative dark energy models with its SZ observations, we constructed a fast semi-analytic method for creating full-sky Compton- γ maps.
- The method developed in the course of this work can be utilised for all cosmological models that can be described by a time dependent equation-of-state, like e.g. the models introduced in Chapter 3.
- Our spatial cluster distribution on the sky takes the angular correlation function into account. To achieve this, we utilise a line-of-sight integrated approach converting, by means of Limber's approximation, the three dimensional power spectrum to an angular one.
- Due to its computational speed, our map making algorithm allows to probe quickly a large parameter space of cosmological models without having to rely on costly numerical simulations.
- The final Compton- γ map can be directly fed into the *PLANCK* LevelS pipeline for simulating realistic observations, as discussed in Chap. 6

It is a capital mistake to theorise before one has data. Insensibly one begins to twist facts to suit theories instead of theories to suit facts.

Sherlock Holmes



Simulating *PLANCK* observations

In order to simulate realistic *PLANCK* observations, one has to take several complications into account that are briefly summarised in the following sections. First, the CMB is not the only emitting source in the frequency range of interest: our galaxy, for instance, radiates through several mechanisms like synchrotron, dust and free-free emission. Second, the detectors suffer from instrumental noise and the scan-pattern as well as the frequency response in the different observing channels have to be taken into account. *PLANCK* will operate in nine frequency channels, as summarised in Tab. 4.1, ranging from 30 GHz to 857 GHz with an angular resolution starting at 33.4 arcmin for the lowest frequency channel and going down to 5 arcmin for the high frequency channels above of 143 GHz. In this work the foreground components, discussed in Sect. 6.1 and Sect. 6.2 for Galactic and extra-Galactic components respectively, and the instrumental noise covered in Sect. 6.3, as discussed in Schäfer et al. (2006b) and Waizmann & Bartelmann (2009), were used. The for this work utilised *PLANCK* LevelS pipeline is discussed in Sect. 6.4, followed by a brief summary at the end.

6.1 Foreground components - Galactic emission

Unfortunately, observing clusters with *PLANCK* will not be as easy as Fig. 2.6 might imply, since Earth is not alone in space but is part of the Solar System, embedded into our Galaxy. Thus, one expects the observations of the CMB and the thermal SZ-effect to be seriously affected by Galactic foregrounds and the thermal emission of celestial bodies in our Solar System. Figure 6.1 shows the spectra for the major sources of sub-mm and microwave emission relevant for *PLANCK* observations. It can be clearly seen that the synchrotron emission dominates at the low frequency end, whereas the dust emission is stronger for the higher frequencies. Now, the choice for the *PLANCK* channel design becomes immediately evident: for measuring the CMB, the channels between 44 GHz and 100 GHz are perfect, and in order to subtract efficiently the foregrounds, one uses the lower and higher frequency channels. In addition the 143 GHz, 217 GHz and 353 GHz match perfectly the spectral fingerprint of the SZ-effect, as depicted in Fig. 4.3. In the following, I only discuss the foreground components that I used for this work, for further details about additional foregrounds, i.e. thermal emission of Solar System

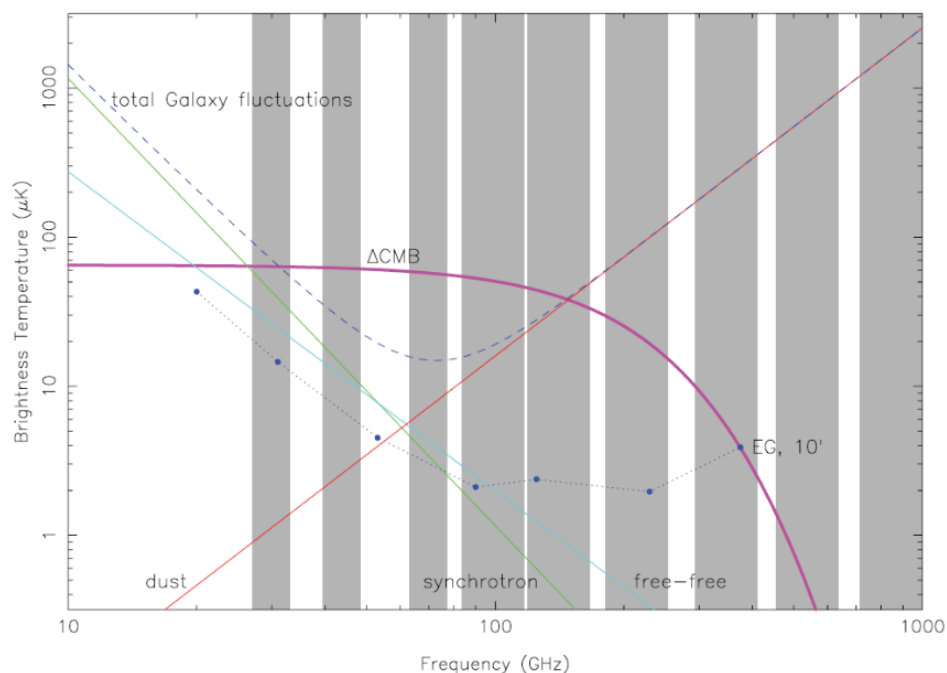


Figure 6.1: Spectrum of the CMB and the frequency coverage of the Planck channels. Also indicated are the spectra of other sources of fluctuations in the microwave sky. Dust, synchrotron, and free-free temperature fluctuation (i.e., unpolarized) levels correspond to the WMAP Kp2 levels (85% of the sky (Bennett et al. 2003)). The CMB and Galactic fluctuation levels depend on angular scale, and are shown for $\sim 1^\circ$. On small angular scales, extra-Galactic sources dominate. The minimum in diffuse foregrounds and the clearest window on CMB fluctuations occurs near 70 GHz. The highest HFI frequencies are primarily sensitive to dust. (Adopted from The Planck Collaboration (2006))

bodies, the reader is referred to Schäfer et al. (2006b).

6.1.1 Galactic dust emission

For the high frequency range above 100 GHz, Galactic dust emission is the dominant foreground component, being mostly concentrated in the Galactic disk. Attempts to model this foreground component have been made by Finkbeiner et al. (2000, 1999) and by Schlegel et al. (1998, 1997). The template Fig. 6.2 utilised in this work was derived from observations at $\nu_0 = 3$ THz that have been extrapolated to the *PLANCK* channels, using a two-component model by C. Baccigalupi, where the emission is given by the superposition of two Planck laws with $T_1 = 9.4$ K and

6.1. Foreground components - Galactic emission

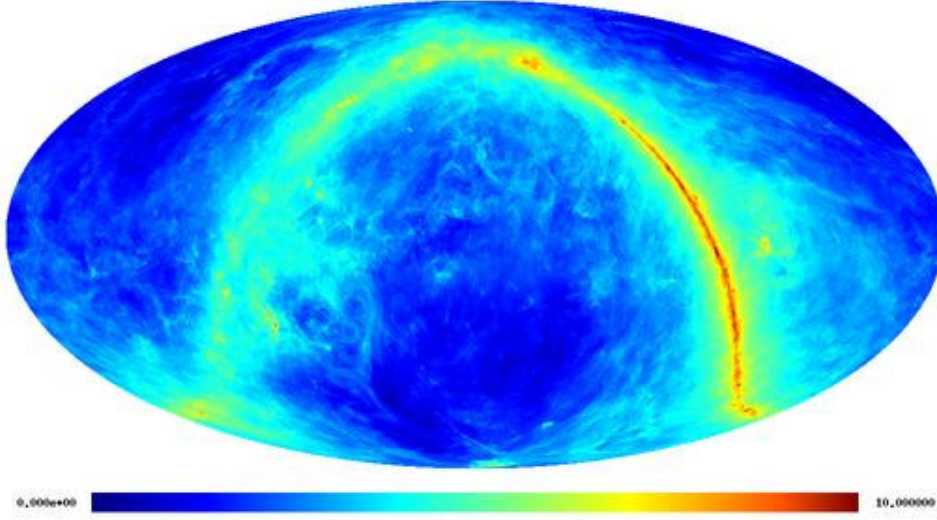


Figure 6.2: Sky template map of the antenna temperature increase for the Galactic dust emission in ecliptic coordinates in the $\nu = 100$ GHz. The shading is proportional to $\text{arsinh}(T_A(\nu = 100 \text{ GHz})/\mu\text{K})$. Courtesy of The Planck Collaboration (2006).

$T_1 = 16.2$ K at a fixed ratio. In this model, the flux $S_{\text{dust}}(\nu)$ is given by

$$S_{\text{dust}}(\nu) = \frac{f_1 q \left(\frac{\nu}{\nu_0}\right)^{\alpha_1} B(\nu, T_1) + f_2 q \left(\frac{\nu}{\nu_0}\right)^{\alpha_2} B(\nu, T_2)}{f_1 q B(\nu_0, T_1) + f_2 q B(\nu_0, T_2)} A_{\text{dust}}, \quad (6.1)$$

where $f_1 = 0.0363$, $f_2 = 1 - f_1$, $\alpha_1 = 1.67$, $\alpha_2 = 2.70$, $q = 13.0$ and $B(\nu, T)$ is the Planckian emission law

$$B(\nu, T) = \frac{2h}{c^2} \frac{\nu^3}{\exp(h\nu/k_B T) - 1}. \quad (6.2)$$

Even though the dust component is expected to have a range of temperatures, this rather simple two-component model reproduces the thermal emission quite well.

6.1.2 Galactic synchrotron emission

The source for the Galactic synchrotron emission are relativistic electrons of the interstellar medium (ISM) spiralling the Galactic magnetic fields. Dominant at frequencies below 100 GHz and extended to high Galactic latitudes, the synchrotron emission is an important foreground component for observations with *PLANCK*. The used template Fig. 6.3 is based on observations at a frequency of 408 MHz (Haslam et al. 1981, 1982), being adapted to *PLANCK* observations by Giardino et al. (2002). The spectral slope of the synchrotron emission has a spectral break

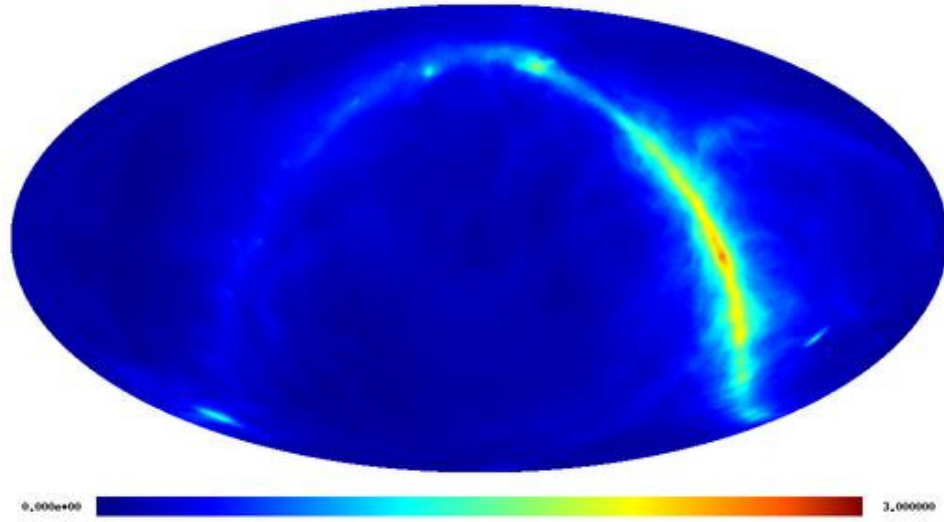


Figure 6.3: Sky template map of the antenna temperature increase for the Galactic synchrotron emission in ecliptic coordinates in the $\nu = 100$ GHz channel. The shading is proportional to $\text{arsinh}(T_A(\nu = 100 \text{ GHz})/\mu\text{K})$. Courtesy of The Planck Collaboration (2006).

at $\nu = 22$ GHz, as has been observed by the *WMAP* team (Bennett et al. 2003). Taking this into consideration, one models the flux $S_{\text{synchro}}(\nu)$ by

$$S_{\text{synchro}}(\nu) = \sqrt{\frac{22 \text{ GHz}}{408 \text{ MHz}}} A_{\text{synchro}} \left(\frac{\nu}{408 \text{ MHz}} \right)^{-1.25} \quad (6.3)$$

where A_{synchro} are the amplitudes of the input map in MJy/sr. It is assumed throughout this work that the spectral index is not spatially varying.

6.1.3 Galactic free-free emission

The template shown in Fig. 6.4 of the Galactic free-free emission is based on H_α -observations (Finkbeiner 2003). For the conversion of the H_α intensity to the free-free intensity the spectral model suggested by Valls-Gabaud (1998) was used. The conversion between the H_α -fluxes A_{H_α} given in units of Rayleighs and the free-free signal's antenna temperature $T_{\text{free-free}}$ measured in Kelvin can be parametrised by

$$\frac{T_{\text{free-free}}(\mu\text{K})}{A_{H_\alpha}(\text{R})} \simeq 14.0 \left(\frac{T_p}{10^4 \text{ K}} \right)^{0.317} 10^{290 \text{ K} \cdot T_p^{-1}} g_{\text{ff}} \left(\frac{\nu}{10 \text{ GHz}} \right)^{-2}. \quad (6.4)$$

where T_p is the plasma temperature, that in this work is always assumed to be 10^4 K. In the microwave bands, the Gaunt factor g_{ff} can be approximated (Finkbeiner 2003) in the frequency range $\nu_p \ll \nu \ll k_B T/h$ (ν_p is the plasma frequency) by

$$g_{\text{ff}} = \frac{\sqrt{3}}{\pi} \left[\ln \left(\frac{(2k_B T_p)^{3/2}}{\pi e^2 \nu \sqrt{m_e}} \right) - \frac{5}{2} \gamma_E \right], \quad (6.5)$$

6.2. Foreground components - extra-Galactic emission

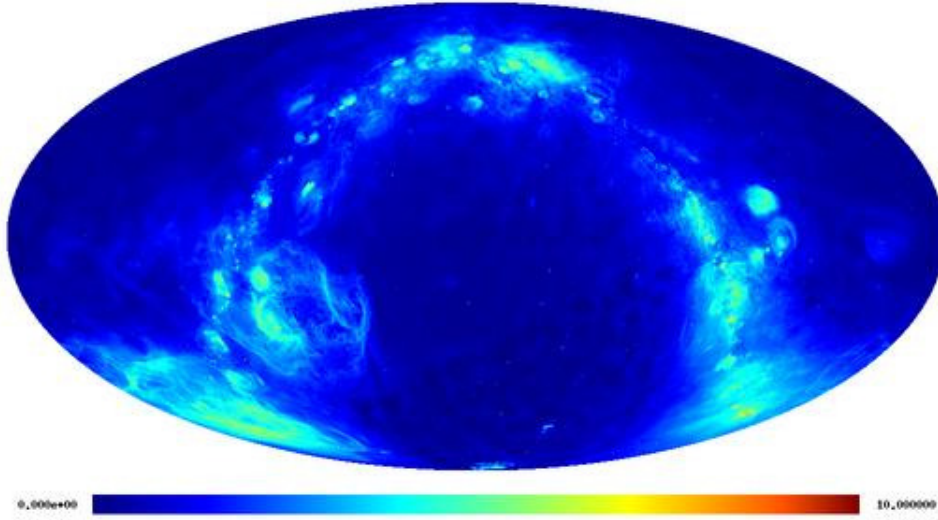


Figure 6.4: Sky template map of the antenna temperature increase for the Galactic free-free emission in ecliptic coordinates in the $\nu = 100$ GHz channel. The shading is proportional to $\text{arsinh}(T_A(\nu = 100 \text{ GHz})/\mu\text{K})$. Courtesy of The Planck Collaboration (2006).

where e and m_e denote the electron charge and mass (in Gaussian units) and $\gamma_E \simeq 0.57721$ is the Euler constant. To obtain the free-free flux $S_{\text{free-free}}(\nu)$, one converts the antenna temperature by means of

$$S_{\text{free-free}}(\nu) = 2 \frac{\nu^2}{c^2} \cdot k_B T_{\text{free-free}}(\text{K}). \quad (6.6)$$

In principle, one could speculate as well about additional H_α -uncorrelated free-free components. Observations in the X-ray bands, however, do not confirm the presence of the required hot gas in the Galaxy.

6.2 Foreground components - extra-Galactic emission

A by far more concerning foreground component, in view of the SZ cluster detection, is of extra-Galactic origin, namely point source contamination stemming from infra-red galaxies and microwave emitting AGN's. Due to the coarseness of the *PLANCK* beams of 5 arcmin, those sources cannot be resolved, indeed they confuse the SZ signal in the different bands and therefore they reduce the efficiency of the cluster finding algorithms as discussed in Chap. 7.

6.2.1 Infra-red galaxies

Infra-red galaxies usually emit more light in the far infra-red than in the visible bands. Presumably, these systems undergo strong star formation events, where the light emitted from the young stars is absorbed by the dust and then re-emitted at longer wavelengths. Star-forming galaxies can have large fractions ($\sim 90\%$) of their total emission at infra-red wavelengths, compared to about one third in the case of local galaxies. The unresolved population of these objects is also considered to be the source of the cosmic infra-red background (CIB) (Puget et al. 1996; Lagache & Puget 2000).

6.2.2 Radio point sources

Another source of extra-Galactic origin in the submillimetric bands are active galactic nuclei (AGN), where the synchrotron emission is the radiation generating mechanism. The observed spectra exhibit a variety of functional behaviours, with spectral indices α generally ranging from -1 to -0.5, even though also sources with inverted spectra $\alpha > 0$ exist. Due to this variety it is rather difficult to extrapolate fluxes to observing frequencies of CMB experiments like *PLANCK*. So far, two studies (Toffolatti et al. 1998; Sokasian et al. 2001) addressed this question in more detail, having estimated the fluctuations generated by radio emitting AGNs at SZ-frequencies to be $10^3 - 10^4$ Jy/sr. The complexity of the underlying astrophysical processes, as well as the poorly known biasing between AGN and the dark matter haloes, however make the reliable modelling of this component extremely difficult.

6.3 Instrumental effects

When simulating observations, one has, apart from the relevant physical effects, also to take the instrumental characteristics and the observing strategy into account. Only in this way one can hope to obtain a realistic picture of the anticipated performance and the quality of the scientific results that can be expected. In the following, I briefly discuss the main instrumental and observing effects included in the simulations I performed.

6.3.1 Instrumental beams

The beam shapes with which the simulated sky maps will have to be convolved can be modelled by azimuthally symmetric Gaussians of the form

$$b(\theta) = \frac{1}{2\pi\sigma_\theta^2} \exp\left(-\frac{\theta^2}{2\sigma_\theta^2}\right) \quad \text{with} \quad \sigma_\theta = \frac{\Delta\theta}{\sqrt{8\ln(2)}}, \quad (6.7)$$

where the $\Delta\theta$ defining the variance is the angular resolution that can be found in Tab. 4.1 for all nine *PLANCK* channels. The approximation of the beam shapes by a

Gaussian is accurate to the percent level and thus deviations like ellipticity, higher-order distortions, diffraction rings, far-side lobes and stray-light are neglected for the present work. Yet they might be important for other applications like e.g. CMB lensing, where real beam shapes in the GRASP8-format have to be used.

6.3.2 Instrumental noise

Apart from the beam pattern, another important instrumental effect is the noise of the detectors giving rise to uncorrelated pixel noise. In order to model this contribution, one creates a map where the noise values in the different pixels are drawn from a Gaussian distribution with width σ_N . Due to the different detector technology for the HFI and LFI detectors, there are two definitions in use to obtain σ_N . First, for *PLANCK*'s LFI detectors one uses

$$\sigma_N = \sqrt{2} \frac{T_{\text{cmb}} + T_{\text{noise}}}{\sqrt{\Delta\nu}/\nu_{\text{sampling}}} \quad (6.8)$$

and second, for the HFI detectors the following relation is applied:

$$\sigma_N = \frac{2\text{NEP}\sqrt{\nu_{\text{sampling}}}}{k_B\Delta\nu}. \quad (6.9)$$

The value for both, the noise equivalent power (NEP) and the noise temperature T_{noise} , are listed in the appendix of the manual of the *PLANCK* simulation pipeline, available from the *PLANCK* website. Further, when creating the noise map, one has to take into account that there is more than one detector per channel. Therefore, assuming Poissonian statistics, one has to scale down the rms-fluctuations σ_N in antenna temperature by $\sqrt{N_{\text{det}}}$, where N_{det} is the number of detectors in the corresponding channel.

6.3.3 Impact of scan strategy

The *PLANCK* spacecraft, situated at the Lagrangian point L2, spins at ~ 1 rpm around an axis offset by $\sim 85^\circ$ from the telescope boresight, therefore the microwave sky is scanned in great circles fixed at the ecliptic poles. For one bearing of the satellite, 60 scans, corresponding to a measurement time of 1 hour, are performed. After that, the rotation axis will be shifted by 2.5 arcmin, which is approximately half a beam diameter, and the next scanning phase starts. In this way, the full sky will be mapped in about half a year.

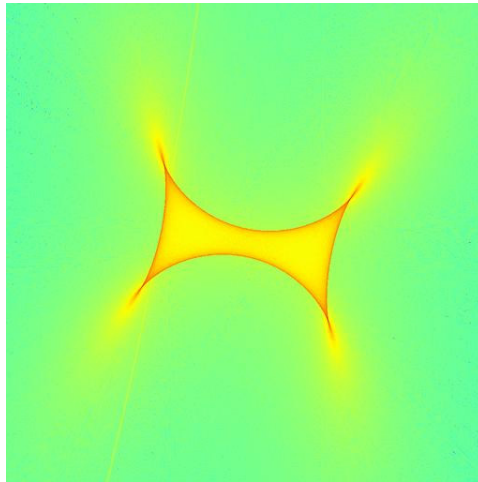


Figure 6.5: Exposure map of the ecliptic North Pole (Schäfer et al. 2006b)

6.3.4 $1/f$ -noise

Due to shifts in the zero-point of the detector gain with time, this peculiar observing pattern will leave its fingerprints in the form of stripes in the noise structure. By Fourier transforming the noise time series of the *PLANCK* receivers, one obtains the noise power spectrum $P(f)$ which reads

$$P(f) = \sigma_N^2 \left[1 + \left(\frac{f}{f_{\text{knee}}} \right)^{-\alpha} \right]. \quad (6.10)$$

Two components contribute to this power spectrum: in the first place, a white noise component, as discussed in Subsect. 6.3.2 and, secondly, a power law component in f having a spectral index α with $0 \leq \alpha \leq 2$. Both components are smoothly joint at the frequency f_{knee} . Large efforts have been undertaken to develop reliable de-stripping techniques (Maino et al. 2002; Keihänen et al. 2005; Ashdown et al. 2007; Kurki-Suonio et al. 2009; Keihänen et al. 2010) which have been proven to be able to remove the $1/f$ -noise efficiently, leaving only the uncorrelated pixel noise. Thus, I neglect the $1/f$ -noise component in my sky simulations in what follows.

6.3.5 Exposure

The scanning strategy just discussed, has another impact on the simulated noise maps: pixels will be observed multiple times during the ongoing survey by the receivers. Bearing this in mind, one can scale down the noise amplitudes in the individual pixels by $\sqrt{N_{\text{obs}}}$, where N_{obs} is numbers of observations in the given pixel. The exposure pattern is not uniform but it exhibits well observed regions around the ecliptic poles (see Fig. 6.5) and less well observed ones around the ecliptic equator.

6.4 The simulation pipeline

For all simulations of *PLANCK* observations presented in this work, I used the *PLANCK* LevelS pipeline (Reinecke et al. 2006), a collection of numerical tools for modelling the output data of the *PLANCK* satellite. The software package allows to create a CMB sky, add in foregrounds (see Sect. 6.1 and Sect. 6.2) and to convolve the sky maps with arbitrary, even non-symmetric and polarised beam patterns. Furthermore the pipeline can deliver the time ordered data streams (TOD) for different scanning strategies as well as incorporate different forms of instrumental noise (see Sect. 6.3).

The LevelS pipeline makes intensive use of the HEALPix package, introduced in Sect. 5.4, and all final products are stored in the fitsio format. Most operations are done in spherical harmonic space, where maps are defined via their spherical

6.4. The simulation pipeline

harmonic expansion coefficients

$$a_{\ell m} = \int_{4\pi} d\Omega a(\theta) Y_{\ell m}^*(\theta) \quad \text{and} \quad a(\theta) = \sum_{\ell=0}^{\infty} \sum_{m=-\ell}^{+\ell} a_{\ell m} Y_{\ell m}(\theta) \quad (6.11)$$

and convolutions can be done by simple multiplications.

The usual steps for a typical simulation with the `LevelS` pipeline are shown in the flowchart presented in Fig. 6.6. Starting from the CMB creation, the simulation is getting more and more mission specific when going down the flowchart. The main steps are:

- Everything begins with the CMB power spectrum which is generated from a set of assumed cosmological parameters. In `LevelS`, the `CAMB` code Lewis et al. (2000), is implemented for this purpose. However, due to the fact that we wanted to study also non-standard dark energy models, we chose for this task the `CMBEASY` code (Doran 2005).
- A realisation of the power spectrum in the form of spherical harmonic coefficients ($a_{\ell m}$) is generated by the `syn_alm_cxx` module.
- The foreground sky maps as discussed in Sect. 6.1 and Sect. 6.2 are converted to spherical harmonic coefficients using the `anafast_cxx` module.
- The `almmixer` module generates a combined set of $a_{\ell m}$ coefficients, where the individual component maps are weighted by convolving their electromagnetic spectra with the frequency response of the selected channel.
- For incorporating the instrumental beam profiles, either a realistic beam pattern is decomposed into spherical harmonics using the `beam2alm` module, or alternatively an idealised beam is created by the `gaussbeampol` module.
- In order to ensure efficient convolution of the beams with point sources in real space, the `beam2alm` module samples the beam on a uniform grid in (θ, φ)
- The `totalconvolve_cxx` module creates, out of the $a_{\ell m}$ of the combined sky and the beam, the so-called *ring set*, allowing to determine the expected intensity a in given receiver for a specific detector pointing and orientation.
- Specifying the mission parameter, the `simmission` module delivers a time stream of satellite locations and orientations. Additionally, the module can also provide the locations of the planets as seen from the spacecraft.
- Finally, the versatile `multimod` module processes the satellite pointing information, the ring sets and the beam profiles to create time streams of the detector pointings and the measured signal. Further, it is able to deliver the signal of the CMB dipole, the point source signal as well as the different sources of instrumental noise. Furthermore, it also provides the co-added sky maps and the exposure maps in the `HEALPix` format.

Chapter 6. Simulating PLANCK observations

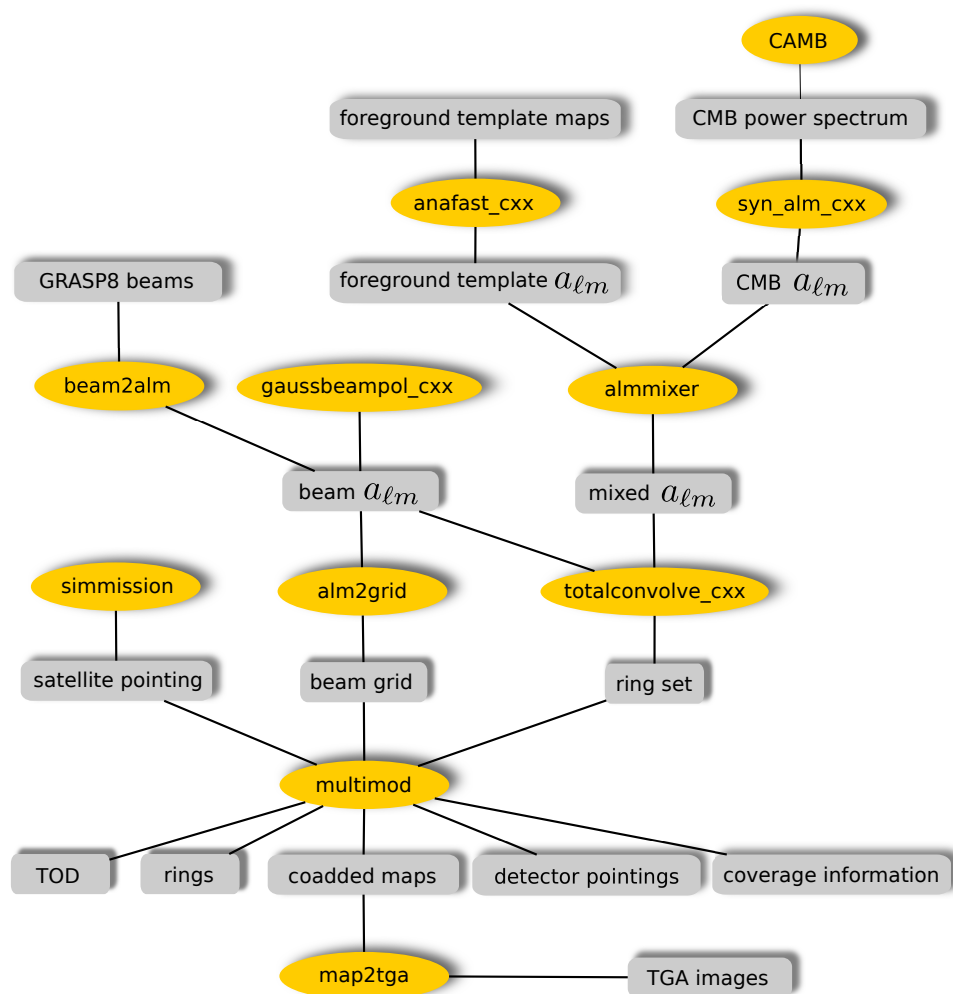


Figure 6.6: Flowchart for the *PLANCK* Level1S pipeline. Here the yellow ellipses denote modules being part of the pipeline and the grey rectangles depict either input parameters or data product.

The Level1S package has been used extensively for this work and has been proven to be of good use for its purpose.

Bottom line - What to take away

- For realistic simulations of *PLANCK* observations, one has to include a number of foreground components. In our Galaxy we have to consider dust, synchrotron and free-free emission. Zodiacal light and the thermal emission of planets are omitted.
- In the light of the SZ cluster detection, extra-Galactic foregrounds, like infrared and radio point sources, should be considered. This is covered more in detail in Chap. 7.
- For our purposes the *PLANCK* beams are assumed to be azimuthally symmetric Gaussian.
- The instrumental noise can be divided into two components, namely a white noise and a $1/f$ component, giving rise to stripe patterns in the noise maps.
- Due to *PLANCK*'s observing strategy, the sky coverage is not homogeneous. Pixels at the ecliptic poles are observed more often compared to those, situated near the equator.
- The aforementioned effects are all incorporated into the LevelS pipeline, that is widely used in the *PLANCK* consortium for realistic simulations of the observations.

There is no rule more invariable than that we are paid for our suspicions by finding what we suspect.

Henry David Thoreau
(1817-1862)

7

Studying SZ cluster with *PLANCK*

Having introduced methods for creating simulated full-sky maps of the SZ-effect and the LevelS pipeline, we are now able to perform realistic simulations of *PLANCK* observations. The remaining task, covered in this chapter, is to find the SZ clusters in the observed maps and to study the properties of the recovered cluster sample. In Sect. 7.1, the applied methods for filtering and detecting the clusters are introduced, followed by a brief discussion about finding the cluster in the filtered maps in Sect. 7.2. Afterwards, in Sect. 7.3, the impact of the different foreground components on the filtering performance is, along with the characteristics and properties of the detected sample, studied in detail. In Sect. 7.4 the perspectives of the used routines and of the *PLANCK* cluster sample are discussed. A brief summary of the key results is outlined in the bottom line at the end.

7.1 Introducing multi-frequency filtering on spherical domains

Efficient and reliable source extraction is one of the major challenges for two-dimensional all-sky surveys. Sources have to be extracted from observed maps containing strong background of varying spectral behaviour and morphology. Depending on the situation, different methods are applied. For instance, in the case of small scale noise, low-pass filtering has been proven to be a reliable method, whereas, in the case of large scale noise, wavelet analysis can successfully be applied. Unfortunately, these methods fail in conditions in which the noise scale is comparable to the signal scale. In the case of CMB observations with *PLANCK*, the background structure is extremely complex and comprises a multitude of scales. However, the task of extracting the sources of interest and to separate the individual components is not hopeless, since one can incorporate the different frequency dependence of the components. *PLANCK*'s nine channel design ensures that the different components can successfully be separated.

7.1.1 Filtering - the general idea

Among the plethora of filtering and component separation methods (Hobson et al. 1998, 1999; Bouchet & Gispert 1999; Maino et al. 2002; Melin et al. 2006; Cardoso

et al. 2008; Leach et al. 2008) available, we decided to utilise the method discussed in Schäfer et al. (2006b) and Schäfer & Bartelmann (2007), which is a generalisation of the matched filtering, as introduced by Sanz et al. (2001) and Herranz et al. (2002), to spherical datasets formulated in spherical harmonic space. The derivation of the filter kernels $\psi(|\theta|, R)$, constructed for the detection of objects of a certain scale R , can be formulated as the solution of a variational problem. The mathematical details of the filter construction are covered in the following Subsect. 7.1.2 such that at this point it is sufficient to state that the detection map $D_i(\theta, R)$ for channel i is obtained by convolving the corresponding filter kernel $\psi_i(|\theta|, R)$ with the co-added map $C_i(\theta)$, where the variance $\sigma_D^2(R)$ of the detection map is constrained to be minimal. Additionally, the filter kernels have to fulfil two further conditions:

1. to ensure the existence of a scale R_0 , such that the filtered field $\langle D(\theta_0, R_0) \rangle$ at the source position θ_0 is maximal and that
2. the filter kernel should be an unbiased estimator of the underlying source amplitude.

The source profiles needed for the filter construction are assumed to be spherically symmetric β -profiles and to be superimposed on a homogeneous and isotropic fluctuating background, obeying Gaussian statistics. Further details on the filter construction, as well as the results of extensive testing of the filter performance and the key assumptions made, can be found in Schäfer et al. (2006b) and Schäfer & Bartelmann (2007). For our case the filtering procedure is summarised in the flowchart shown in Fig. 7.1. After the construction of the co-added Compton- y maps in $a_{\ell m}$ -space, as shown in the upper part of the flowchart, filters optimised for finding beam convolved β -profiles are constructed and normalised by the variance of the co-added sky maps. In doing so, the convolution of the filters with the co-added maps and back-transforming to real-space yields a detection map, giving a signal-to-noise (S/N) ratio for each pixel. Applying a S/N threshold of 3σ and a Galactic cut of 10° prepares the detection map for the last step of cluster identification, which is discussed in further detail in Sect. 7.2.

7.1.2 Filtering - mathematical description

The signal map $s_\nu(\theta)$ that is supposed to be filtered is modelled by

$$s_\nu(\theta) = f_\nu y_\nu(|\theta - \theta_0|) + n_\nu(\theta), \quad \nu = 1, \dots, N, \quad (7.1)$$

where $\theta = (\vartheta, \varphi)$ denotes a two-dimensional vector on the sphere, θ_0 is the source location, N is the number of frequencies ν , $f_\nu \equiv \langle S_Y \rangle_\nu$ is the flux-weighted frequency dependence of the thermal SZ effect, $y_\nu(|\theta - \theta_0|)$ is the amplitude of the sources to be detected and $n_\nu(\theta)$ is the noise component, consisting of the CMB, the foregrounds and the instrumental noise. For constructing the optimal filter, it is assumed that an individual cluster is situated at the North Pole ($\theta_0 = \mathbf{0}$). The

7.1. Introducing multi-frequency filtering on spherical domains

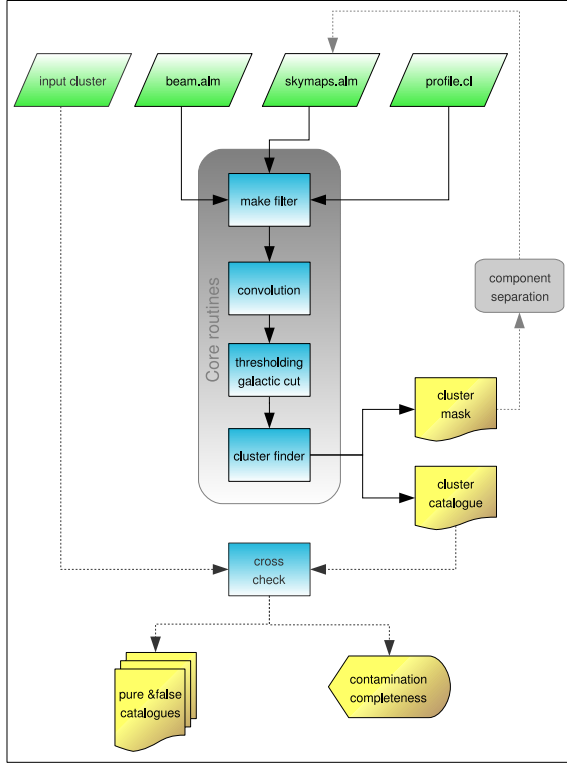


Figure 7.1: Flowchart for the cluster detection routines applied in this work. The green rhomboids illustrate input data, like sky maps, beam profiles, the input cluster catalogue and the filter profile. The blue rectangles depict modules and the yellow objects are products like the cluster catalogues or a cluster mask which could be used in further attempts of component separation. On the bottom, there is also the cross-check module shown, which compares the recovered with the input cluster catalogue delivering information about contamination and completeness of the sample.

angular SZ-signal is modelled by $y_\nu(\theta = |\theta|) = A\tau_\nu(\theta)$, separating the amplitude A and the profile $\tau(\theta)$. The underlying cluster profile $p(\theta)$ is assumed to be a King-profile, which has to be convolved at each observation frequency with the (Gaussian) beam (see Sect. 6.3) of the corresponding *PLANCK* channel, such that we have:

$$\tau_\nu(\theta) = \int d\Omega' p(\theta') b_\nu(|\theta - \theta'|) = \sum_{\ell=0}^{\infty} \tau_{\ell 0, \nu} Y_\ell^0(\cos \theta), \quad (7.2)$$

$$p(\theta) = \left[1 + \left(\frac{\theta}{\theta_c} \right)^2 \right]^{-1}, \quad \text{and} \quad \tau_{\ell 0, \nu} = \sqrt{\frac{4\pi}{2\ell + 1}} b_{\ell 0, \nu} p_{\ell 0}. \quad (7.3)$$

The convolution theorem on the sphere has been used in the second step above. Furthermore, it is assumed that the noise background $n_\nu(\theta)$ is a homogeneous and isotropic random field with a cross power spectrum $C_{\ell, \nu_1 \nu_2}$ defined by

$$\langle n_{\ell m, \nu_1} n_{\ell' m', \nu_2}^* \rangle = C_{\ell, \nu_1 \nu_2} \delta_{\ell \ell'} \delta_{m, m'}, \quad \text{where} \quad \langle n_\nu(\theta) \rangle = 0, \quad (7.4)$$

here $n_{\ell m, \nu}$ is the spherical harmonics expansion coefficient of $n_\nu(\theta)$, $\delta_{\ell \ell'}$ denotes the Kronecker symbol, and $\langle \cdot \rangle$ corresponds to an ensemble average. Assuming ergodicity of the field under consideration allows taking spatial averages over sufficiently large areas $\Omega = \mathcal{O}(4\pi)$ instead of performing the ensemble average.

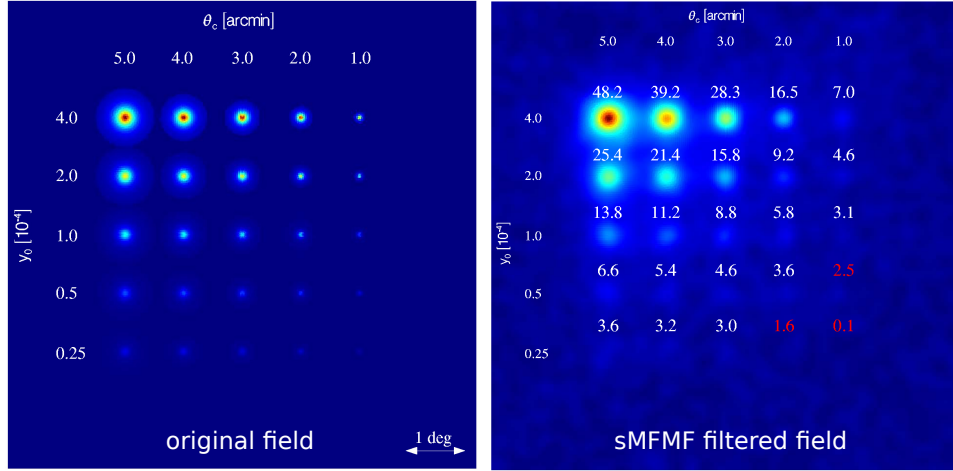


Figure 7.2: Comparison of unfiltered (left panel) with the filtered field (right panel). The simulated clusters were placed on the North Pole in a prick-test setup for different central Comptonisations y_0 and profile core sizes θ_c .

The spherical multi-frequency matched filter (sMFMF) has been introduced and studied in detail by Schäfer et al. (2006b). Basically, one constructs a centrally symmetric optimised filter function $\psi_\nu(\theta)$ operating on a sphere, which induces, by means of its functional behaviour, a family of filters $\psi_\nu(\theta, R_\nu)$ differing only by a scaling parameter R_ν . The filtered field $u_\nu(R_\nu, \beta)$ is, for a given choice of R_ν , defined as the convolution of the filter function with the observed all-sky map at a frequency ν ,

$$u_\nu(R_\nu, \beta) = \int d\Omega s_\nu(\theta) \psi_\nu(|\theta - \beta|, R_\nu) \quad (7.5)$$

$$= \sum_{\ell=0}^{\infty} \sum_{m=-\ell}^{+\ell} u_{\ell m, \nu} Y_\ell^m(\beta) \quad \text{with} \quad (7.6)$$

$$u_{\ell m, \nu} = \sqrt{\frac{4\pi}{2\ell+1}} s_{\ell m, \nu} \psi_{\ell 0, \nu}(R_\nu). \quad (7.7)$$

where the convolution theorem on the sphere has been utilised once more. The next step is to combine the single filtered fields by means of

$$u(R_1, \dots, R_N; \beta) = \sum_{\nu} u_\nu(R_\nu, \beta). \quad (7.8)$$

In our noise model from Eq. 7.4, the expectation value of the noise $\langle n_\nu(\theta) \rangle$ is assumed to vanish, therefore the expectation value of the filtered field at the North Pole $\beta = \mathbf{0}$ yields

$$\langle u_\nu(R_\nu, \mathbf{0}) \rangle = A f_\nu \sum_{\ell=0}^{\infty} \tau_{\ell 0, \nu} \psi_{\ell 0, \nu}(R_\nu). \quad (7.9)$$

7.1. Introducing multi-frequency filtering on spherical domains

Since the amplitude of the thermal SZ effect is small compared to unity, $A_{y,w} \ll 1$, the cross power spectrum of the signal is assumed to be negligible compared to the noise power spectrum. Therefore, the variance of the combined filtered field (Eq. 7.8) is determined by

$$\begin{aligned}\sigma_u^2(R_1, \dots, R_N) &= \left\langle [u(R_1, \dots, R_N; \beta) - \langle u(R_1, \dots, R_N; \beta) \rangle]^2 \right\rangle \\ &= \sum_{v_1, v_2} \sum_{\ell=0}^{\infty} C_{\ell, v_1 v_2} \psi_{\ell 0, v_1}(R_{v_1}) \psi_{\ell 0, v_2}(R_{v_2}),\end{aligned}\quad (7.10)$$

where the filter functions $\psi_v(\theta)$ are optimised to detect the clusters at the North Pole of the sphere (to which they have been translated by construction). The filters have a singly peaked profile characterised by the scale $R_v^{(0)}$ as given by Eq. 7.2. Furthermore the optimised *matched filter* is constructed to obey the two following conditions Schäfer et al. (2006b):

1. The combined filtered field $u(R_1^{(0)}, \dots, R_N^{(0)}; \mathbf{0})$ is an unbiased estimator of the source amplitude A , i.e. $\langle u(R_1^{(0)}, \dots, R_N^{(0)}; \mathbf{0}) \rangle = A$.
2. The variance of $u(R_1, \dots, R_N; \beta)$ has a minimum at the scales $R_1^{(0)}, \dots, R_N^{(0)}$ ensuring that the combined filtered field is an efficient estimator.

Since we are not dealing with single-frequency objects, it is convenient to define column vectors $\boldsymbol{\psi}_\ell \equiv [\psi_{\ell 0, v}]$, $\mathbf{F}_\ell \equiv [f_v \tau_{\ell 0, v}]$, and the inverse $\hat{\mathbf{C}}_\ell^{-1}$ of the matrix $\hat{\mathbf{C}}_\ell \equiv [C_{\ell, v_1 v_2}]$. The first constraint from above can be formulated in terms of spherical harmonic expansion coefficients as

$$\sum_v \sum_{\ell=0}^{\infty} f_v \tau_{\ell 0, v} \psi_{\ell 0, v} = \sum_{\ell=0}^{\infty} \mathbf{F}_\ell \boldsymbol{\psi}_\ell = 1. \quad (7.11)$$

The spherical matched filter $\boldsymbol{\psi}_\ell$ is obtained by performing a functional variation (with respect to the filter function ψ_ℓ) of $\sigma_u^2(R_1, \dots, R_N)$ while incorporating the boundary condition Eq. 7.11 through a Lagrangian multiplier. Thus, the spherical matched filter turns out to be given by

$$\boldsymbol{\psi}_\ell = \alpha \hat{\mathbf{C}}_\ell^{-1} \mathbf{F}_\ell, \quad \text{where} \quad \alpha^{-1} = \sum_{\ell=0}^{\infty} \mathbf{F}_\ell^T \hat{\mathbf{C}}_\ell^{-1} \mathbf{F}_\ell. \quad (7.12)$$

Usually, the cross power spectrum $C_{\ell, v_1 v_2}$ is computed from the observed data, which will be in our case the co-added maps, provided that the cross power spectrum of the signal is negligible. The quantities α , $\mathbf{F}_{\ell 0}$, and thus $\boldsymbol{\psi}_{\ell 0}$ can directly be computed for a specific frequency dependence f_v and for a model source profile $\tau_v(\theta)$.

When it comes to the assessment of observational significance, it is important to have a measure of the signal-to-noise ratio (S/N) for a given possible detection. It is therefore useful to construct the optimised filter function with the aim of

maximising the signal-to-noise ratio D_u ,

$$D_u \equiv \frac{\langle u(R_1, \dots, R_N; \mathbf{0}) \rangle}{\sigma_u(R_1, \dots, R_N)} = A \cdot \frac{\sum_{\ell=0}^{\infty} \mathbf{F}_\ell \boldsymbol{\psi}_\ell}{\sqrt{\sum_{\ell=0}^{\infty} \boldsymbol{\psi}_\ell^T \hat{\mathbf{C}}_\ell \boldsymbol{\psi}_\ell}}. \quad (7.13)$$

The signal-to-noise ratio D_s of a signal on the fluctuating background can be found by computing the dispersion of the unfiltered field on the sphere and is given by

$$\sigma_s^2 = \sum_{v_1, v_2} \sum_{\ell=0}^{\infty} C_{\ell, v_1 v_2} \Rightarrow D_s = \frac{A}{\sigma_s}. \quad (7.14)$$

Therefore, the *gain* for comparing the signal-to-noise ratios of a peak before and after convolution with a filter function reads:

$$g \equiv \frac{D_u}{D_s} = \frac{\sigma_s}{\sigma_u(R_1, \dots, R_N)}. \quad (7.15)$$

For further details on gain related issues, the reader is referred to Schäfer et al. (2006b). However, it should be mentioned at this place that a successful filter construction is directly linked to the fact the filters are able to reduce the dispersion ($\sigma_u(R_1, \dots, R_N) < \sigma_s$) while simultaneously retaining the expectation value of the field (Eq. 7.9). Due to the additional third constraint, the scale-adaptive filter is expected to achieve smaller gains compared to the matched filter.

7.2 Finding clusters in the filtered maps

The delivered product of the filtering, outlined in the previous Sect. 7.1, is a HEALPix map of the S/N ratios. The map is prepared for the final cluster detection with `clustFind_cxx` by setting all pixels below the S/N threshold and in the region of the Galactic cut to zero. The `clustFind_cxx` module I implemented, is designed to be very general and therefore applicable to finding objects in HEALPix maps, without sacrificing the computational speed. For development and testing purposes, additional modules for creating test maps, like the one shown in Fig. 7.3, have been coded.

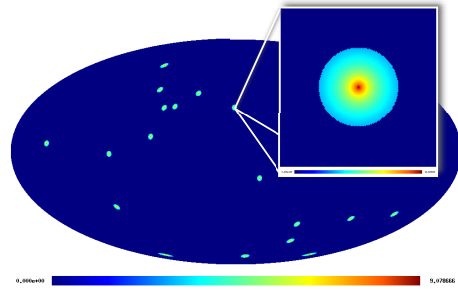


Figure 7.3: Testmap for the development of the `clustFind_cxx` algorithm.

Algorithmic idea

The basic idea of how clusters are detected is depicted in Fig. 7.4. In order to be as general as possible, all connected pixels (groups), being above a specified threshold

7.2. Finding clusters in the filtered maps

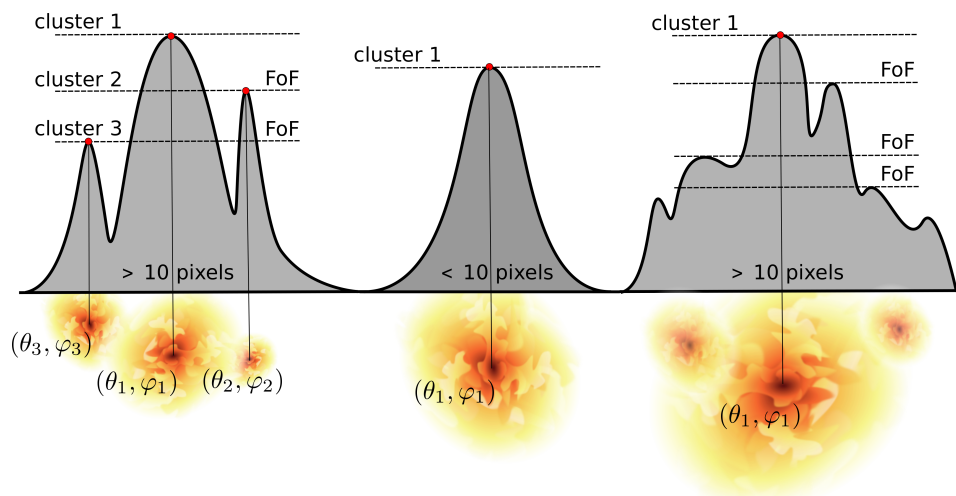


Figure 7.4: Possible cases of cluster identification that could be encountered with `clustFind_cxx`. From left to right, group of more than 10 pixels and the FoF finds two subgroups resulting in three detections, then the case of less than 10 pixels in the group and thus on detection, followed by the case in which the group has more than 10 pixels and several subgroups such that only the main peak is taken.

are considered as a possible cluster detection. If the number of pixels in that group is smaller than 10, then the pixel with maximum significance in that group is taken as centre of the detected cluster. However, if more pixels belong to the group, then a friend-of-friend finder (FoF) is activated, ensuring that all maxima in group are found. In the case that the FoF finds more than 4 subgroups in the main group (a ring-like structure e.g. could have several maxima), the original maximum finder is activated. Detections that only consist of one pixel are neglected, since they stem with a high probability from statistical fluctuations. Finally, all identified systems are dumped to a catalogue specifying the `HEALPix` pixel of the centre, the angular coordinates and the statistical significance in S/N. Additionally, the module can as well include an estimate of the Comptonisation Y , which is discussed in Subsect. 7.3.4.

Implementation

The `clustFind_cxx` module has been implemented in C++, using extensively the `HEALPix` and Standard Template Library (STL). In order to reduce the memory consumption, the module saves only the `HEALPix` Pixel number and the S/N value for non-zero pixels (remember that all pixels below the S/N threshold were set to zero) into a STL map container. I decided to make extensive usage of STL container methods, because they allow to code the problem in a memory efficient way and allowing for fast searches for container members.

The whole filtering and cluster detections pipeline is rather fast: starting from a given set of co-added maps, it takes less than 45 minutes on a normal PC architecture to obtain a cluster catalogue. The fact that the method works full-sky is fast and blind makes it an ideal tool for our purposes in allowing fast parameter studies for different dark energy models or the effect of various foreground components.

7.3 The impact of foregrounds on the filter performance

For a reliable assessment of *PLANCK*'s expected cluster sample, a crucial part is to understand the filter performance and to analyse which astrophysical effects, present as background noise, affect the results in the strongest way. To do so, I decided to compile a set of co-added test maps, built up from different astrophysical components. This set of maps comprised the following components: CMB (C), thermal SZ effect (T), noise (N), synchrotron emission (S), dust emission (D), free-free emission (F), radio sources (R) and infrared galaxies (I). Hereafter, the nomenclature of the co-added maps is based on adding the abbreviations listed before, like e.g. a map consisting of CMB, thermal SZ effect, noise and Synchrotron emission will be abbreviated as CTNS map. The influence of the different components can be studied by feeding these co-added maps into the cluster detection pipeline and by cross-checking the result against the known input cluster catalogue. Since the computational costs for the cluster finding and cross-checking are relatively small, the whole procedure was as well done for several choices of the filter core sizes θ_c .

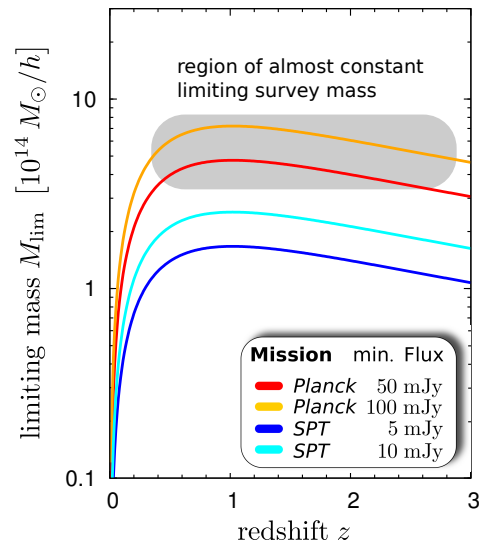


Figure 7.5: Limiting survey mass as a function of redshift for four hypothetical *PLANCK* and *SPT* surveys.

7.3.1 Number of detections, contamination and completeness

Principally, (full-sky) SZ cluster surveys, provided that they are big enough, are a powerful tool for cosmology Carlstrom et al. (2002). A SZ survey is basically mass limited, almost independent of redshift as can be seen from Fig. 7.5, where the limiting survey mass, computed for four hypothetical *PLANCK* and *SPT* survey with different detection limits, is shown. In general, the redshift distribution of galaxy clusters is critically sensitive to Ω_m and the properties of the dark energy.

7.3. The impact of foregrounds on the filter performance

For sufficiently large and deep SZ surveys, it is possible, in principle, to extract also the equation-of-state of the dark energy. Unfortunately, in reality current SZ surveys still suffer from immense observational problems, stemming for example from foreground contamination.

The expected number of by *PLANCK* detectable clusters was historically subject to strong change. In the beginning estimates ranged from $(1 - 5) \times 10^4$ clusters (Aghanim et al. 1997; Bartelmann 2001; Kay et al. 2001; The Planck Collaboration 2006), which would have meant a huge leap in cluster cosmology. And then gradually decreased to numbers between $(3 - 10) \times 10^3$ (Geisbüsch et al. 2005; Schäfer & Bartelmann 2007) followed by a drop to significantly below 1000 in recent years triggered by the *PLANCK* cluster challenge (Melin et al.[in prep.]).

Apart from the pure number of detections, there are two other important quantities: first, the contamination of the detected sample, which is defined as

$$\Gamma_{\text{cont}} = 1 - \frac{N_{\text{true}}}{N_{\text{det}}}, \quad (7.16)$$

where N_{true} is the number of true detected clusters and N_{det} is the number of claimed detections. Furthermore, one can ask oneself what fraction of the clusters that could have been detected, actually were detected. This quantity is referred to as completeness and is defined as

$$\Gamma_{\text{comp}} = \frac{N_{\text{true}}}{N_{\text{tot}}(Y > Y_{\text{min}})}. \quad (7.17)$$

The number of detectable clusters $N_{\text{tot}}(Y > Y_{\text{min}})$ depends on a lower limit of the observable which is in our case a limiting Comptonisation Y_{min} . In the following discussion, I always assume a minimal Comptonisation of $Y_{\text{min}} = 10^{-4} \text{ arcmin}^2$. In order to study the impact of the single foreground components, I added one component respectively and fed it into the filtering pipeline. In doing so, one can directly assess the individual influence of the single components. The results of this analysis are summarised in the histograms shown in Fig. 7.6, where I list the individual contaminations, completeness (left column) as well as the total and true number of detections (right panel) for different filter core sizes θ_c increasing from top to bottom. For the individual foreground components, one can summarise:

Synchrotron This component only marginally affects the completeness and causes an increase in the contamination on the few percent level. Total number of claimed detections increases a bit but the number of true detections remains constant.

Free-Free The impact of the free-free component is similar to the synchrotron one, in the sense that completeness and contamination as well as the number of claimed and true detections are only marginally affected.

Chapter 7. Studying SZ cluster with PLANCK

Dust This foreground has a substantial effect on the detected sample, which is more strongly contaminated and simultaneously exhibits a drop in completeness. This is accompanied by a drop in both, claimed and true detections.

Radio Interestingly, the radio sources cause a significant drop in the absolute number of detections but at the same time the sample has the smallest contamination and a quite low completeness.

Infra-red Similar to the radio source, the infra-red foreground leads to a drop in the overall number of detections and shows the highest level of contamination and the lowest completeness.

From the point of view of spherical multi-frequency matched filtering one can, according to the findings depicted in Fig. 7.6, distinguish two classes of foregrounds. First, the synchrotron and free-free emission does not lessen the performance of the filtering and cluster finding. Second and more important, the dust emission, radio and infra-red sources drastically worsen the results. This result is worrisome from several points of view, since the last two components (radio and infra-red) have usually been omitted in previous studies (Schäfer et al. 2006b; Schäfer & Bartelmann 2007) resulting in an overestimation of the by this method detectable clusters. Apart from this, even in the perfect CTN case, the level of contamination, which ranges depending on the filter core size θ_c from 14% – 27%, is quite alarming. The impact of θ_c can be summarised as: increasing θ_c reduces the number of detections, but also reduces the contamination and the completeness.

Having studied the individual impact of the foregrounds, the next step is to add subsequently the different components and to study the evolution of the detected cluster sample as shown in Fig. 7.7. As expected, the number of both detections, claimed and true, drop with each component that is added. For a $\theta_c = 3.0$, one starts with ~ 4800 true detections that in the full CTNSDFRI case end up at ~ 1800 hits. This is attended by a successive drop in completeness and an overall increase in contamination. The fact that the contamination does not monotonically increase stems from the fact that the size of the claimed and true sample shrinks simultaneously. The effect of θ_c is identical to the one inferred from Fig. 7.6.

Overall, one has to bear in mind that a contamination of the order of $\sim 30\%$ and a completeness of 10% for a $Y_{\min} = 5 \times 10^{-4}$ poses a challenge in terms of extracting cosmological information. Or more drastically, from a cosmologist's point of view, the scientific value of *PLANCK*'s SZ cluster sample has to be seriously questioned. The only way out is a thorough follow-up of all the claimed detections in order to confirm them, or to raise the S/N threshold, which in turn reduces the size of the sample to a few hundred clusters. A number that could easily be reached by optical cluster detection.

7.3. The impact of foregrounds on the filter performance

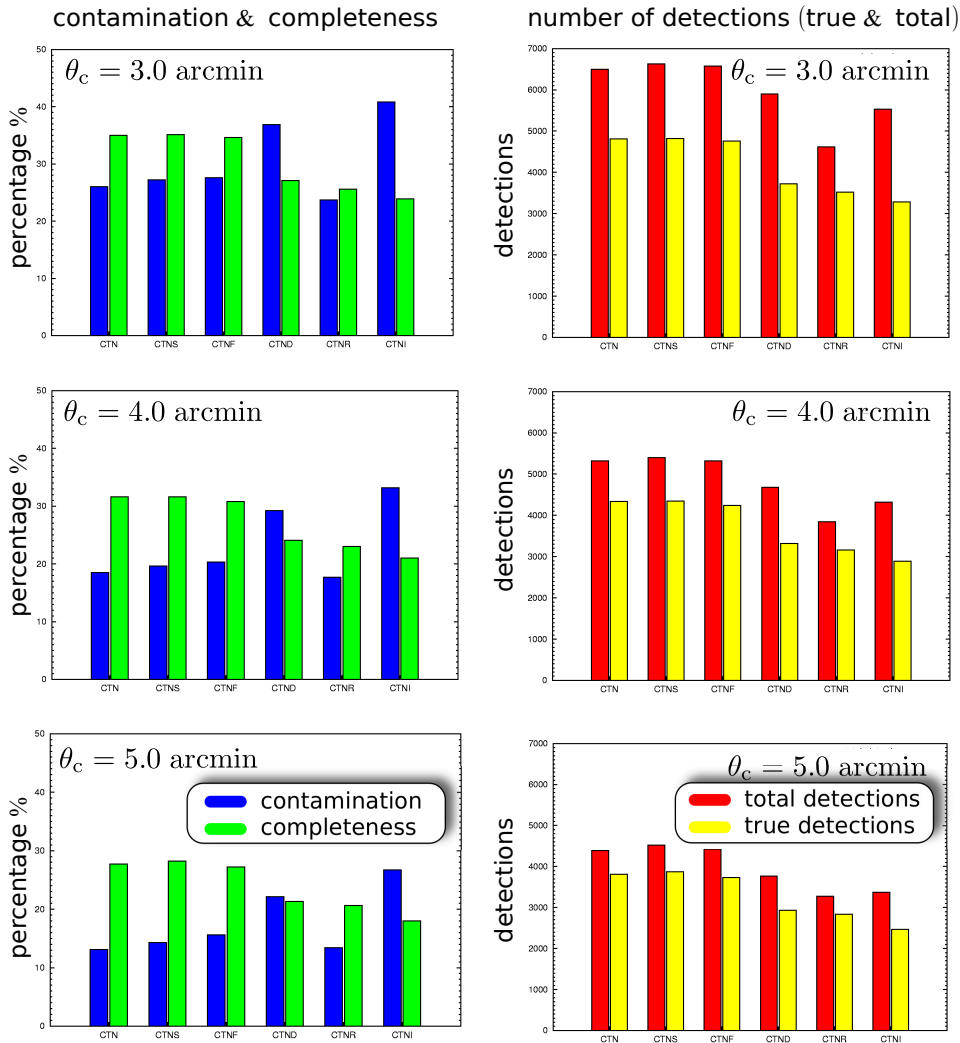


Figure 7.6: Impact of the different foreground components on the filter performance. The left column gives the contamination and completeness of the detected sample as a function for the differently co-added maps, whereas the right column comprises the number of total and true detections for the same maps. From top to bottom, increasing angular core sizes θ_c for the filters have been used. The abbreviations for denoting the different co-added maps are: C (CMB), T (thermal SZ), S (synchrotron), D (dust), F (free-free), R (radio sources), I (infra-red sources).

7.3.2 Spatial distribution of the detections

Apart from the numerical properties of the detected sample, it is interesting to study the spatial distribution of the true and false detections. To do so, I computed the detection density on the sphere averaging over a disc of the size of 20° for both groups of detections and the consecutively added up foreground maps.

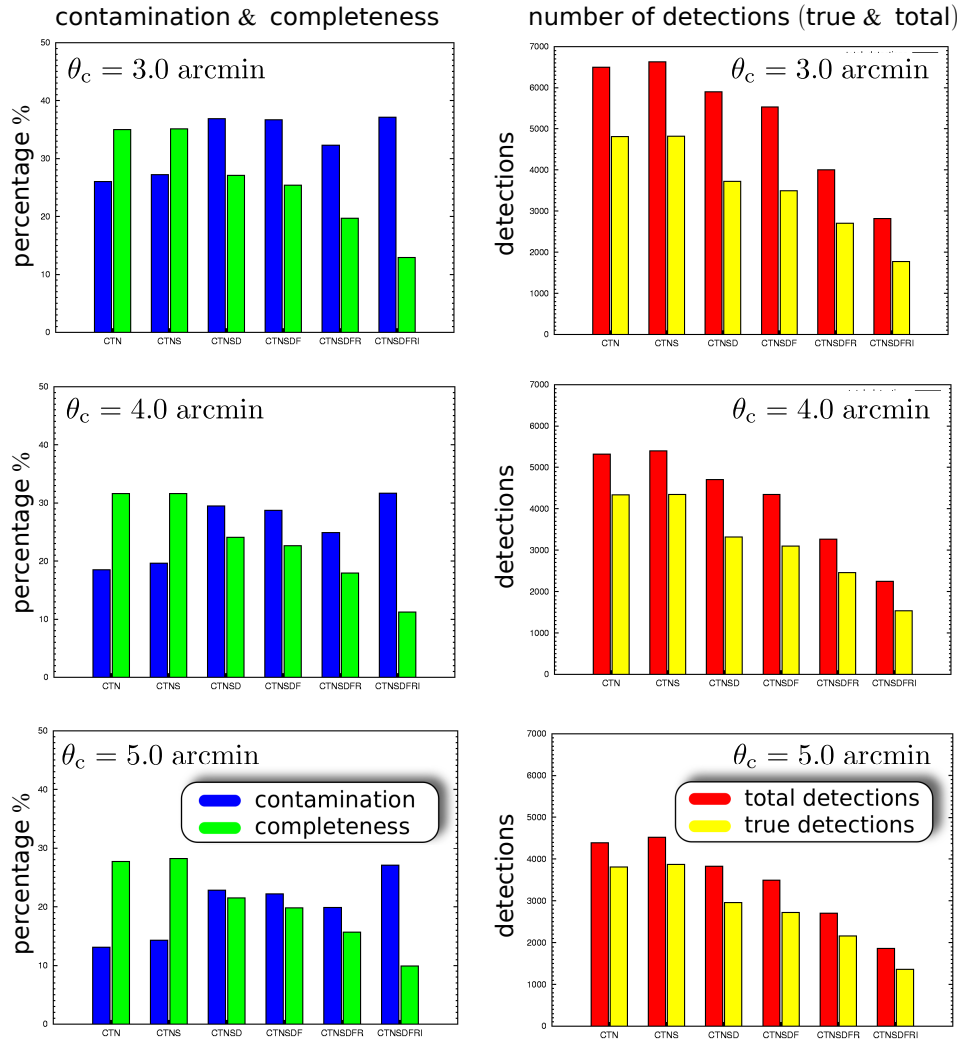


Figure 7.7: Impact of the different added foreground components on the filter performance. The left column gives the contamination and completeness of the detected sample as a function for the differently co-added maps, whereas the right column comprises the number of total and true detections for the same maps. From top to bottom, increasing angular core sizes θ_c for the filters have been used. The abbreviations for denoting the different co-added maps are: C (CMB), T (thermal SZ), S (synchrotron), D (dust), F (free-free), R (radio sources), I (infra-red sources).

The resulting maps are shown in Fig. 7.9 and Fig. 7.10. The first feature one recognises in the maps is that the distribution of the detections is by no means isotropic, but it follows an identical bipolar pattern on the sky. The pattern of both the false and true detections anti-correlates with the exposure map giving

7.3. The impact of foregrounds on the filter performance

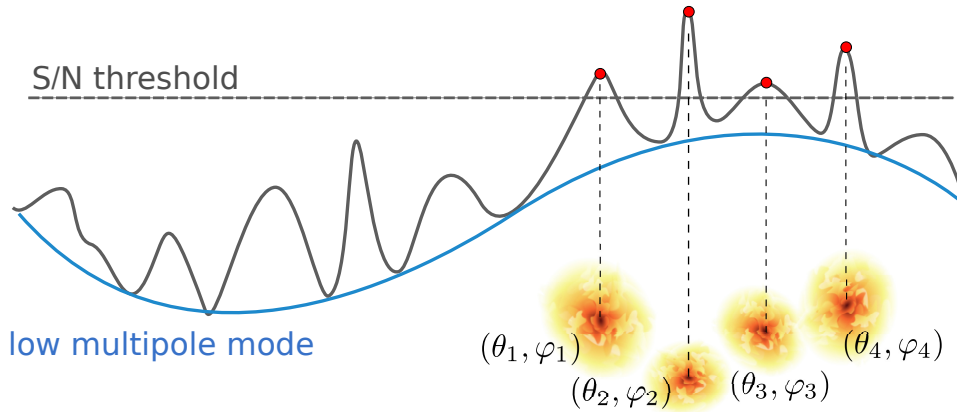


Figure 7.8: Effect of long wavelength modes on cluster detectability.

the number of observations per pixel. As discussed in Subsect. 6.3.3, the number of observations in a pixel is highest at the ecliptic poles due to *PLANCK*'s scan-strategy. Figure 6.5 presents a cut of exposure map (number of hits per pixel) from the ecliptic North Pole for the 353 GHz-channel. As discussed in Subsect. 6.3.3, the noise amplitudes in the individual pixels are scaled down by $\sqrt{N_{\text{obs}}}$, which means that we observe most of the clusters in the regions where the instrumental noise is biggest.

In order to understand the non-isotropy of the spatial distribution of the detections, we have to recall the process of filter construction in Subsect. 7.1.2. One of the basic assumptions in the filter construction was the isotropy and homogeneity of the noise background, if we think to our co-added sky maps however, it is immediately obvious that our noise background is not isotropic, the instrumental noise has a bipolar pattern due to the scanning strategy and all the Galactic foregrounds add a strong signal at the Galactic plane. Due to the failure of our isotropy assumption on large scales (small multipoles), the constructed filters will not work properly at the small multipole-end. As shown in Fig. 7.8, we obtain long-wavelength modes in our detection maps on which the enhanced detection peaks of our clusters will sit. Due to these long-wavelength modes, in some regions the detections will more easily pierce the detection threshold than in others. This situation is similar to the peak-background split used for the biasing of galaxies with respect to dark matter haloes (Mo & White 1996). This observation also coincides with the fact that for the CT case, where there is no instrumental noise present at all, the filtering process completely fails.

7.3.3 The selection function

An important quantity for characterising the quality of a survey, apart from the contamination and completeness of the detected sample, is the selection function. This function characterises how the detected sample is distributed in mass and redshift,

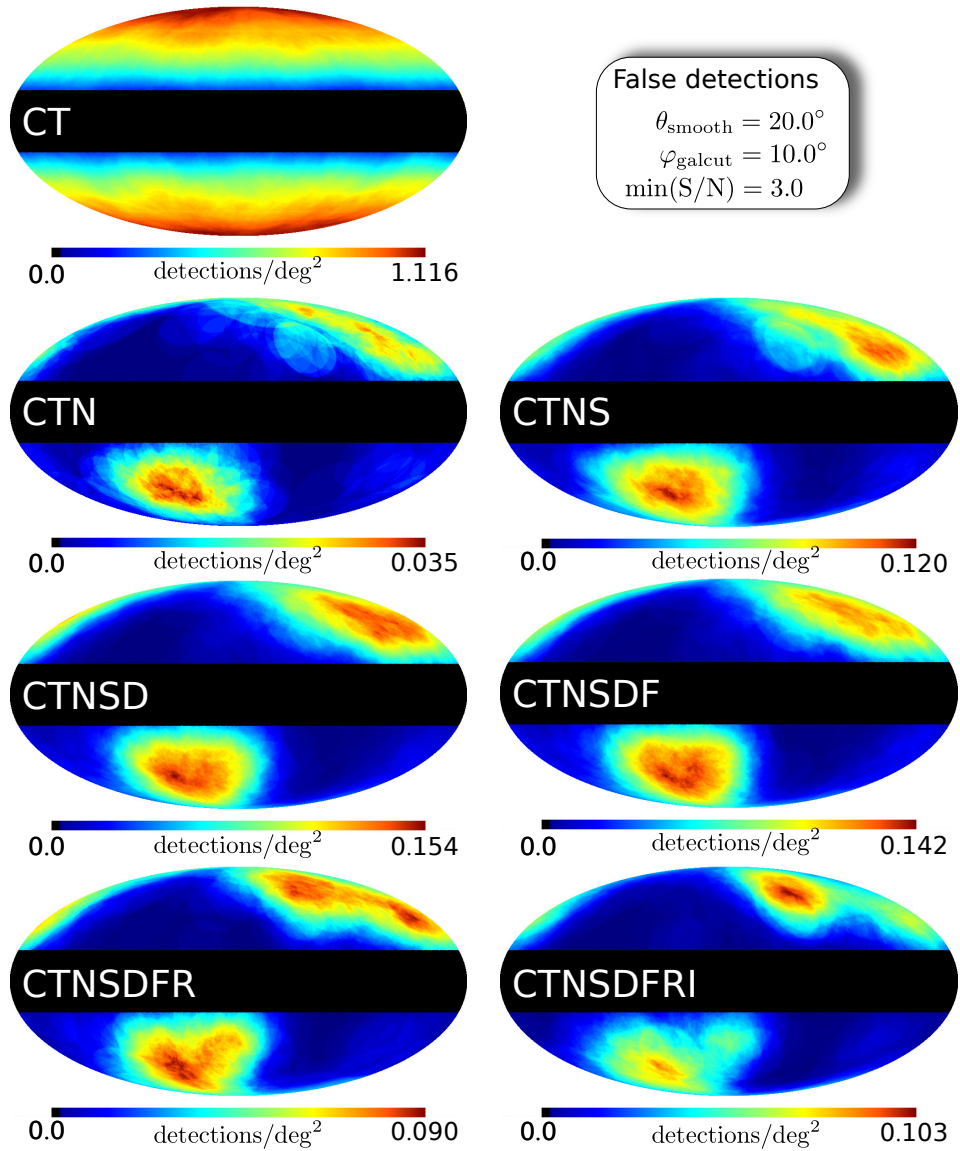


Figure 7.9: Spatial distribution of the false detections given in number of detections per square degree, averaged in as disc of size $\theta_{\text{disc}} = 20^\circ$. The black region depicts the Galactic cut of $\theta_{\text{cut}} = 10^\circ$ in which we do not consider detections due to the strong Galactic signal. The abbreviations for denoting the different co-added maps are: C (CMB), T (thermal SZ), S (synchrotron), D (dust), F (free-free), R (radio sources), I (infra-red sources). Note that the colour bars are individually different for the different maps.

or in different words, how complete the sample is distributed in mass and redshift bins. For the construction of the selection function we can rely on the input cluster catalogues produced in the map making process outlined in Chap. 5. Since

7.3. The impact of foregrounds on the filter performance

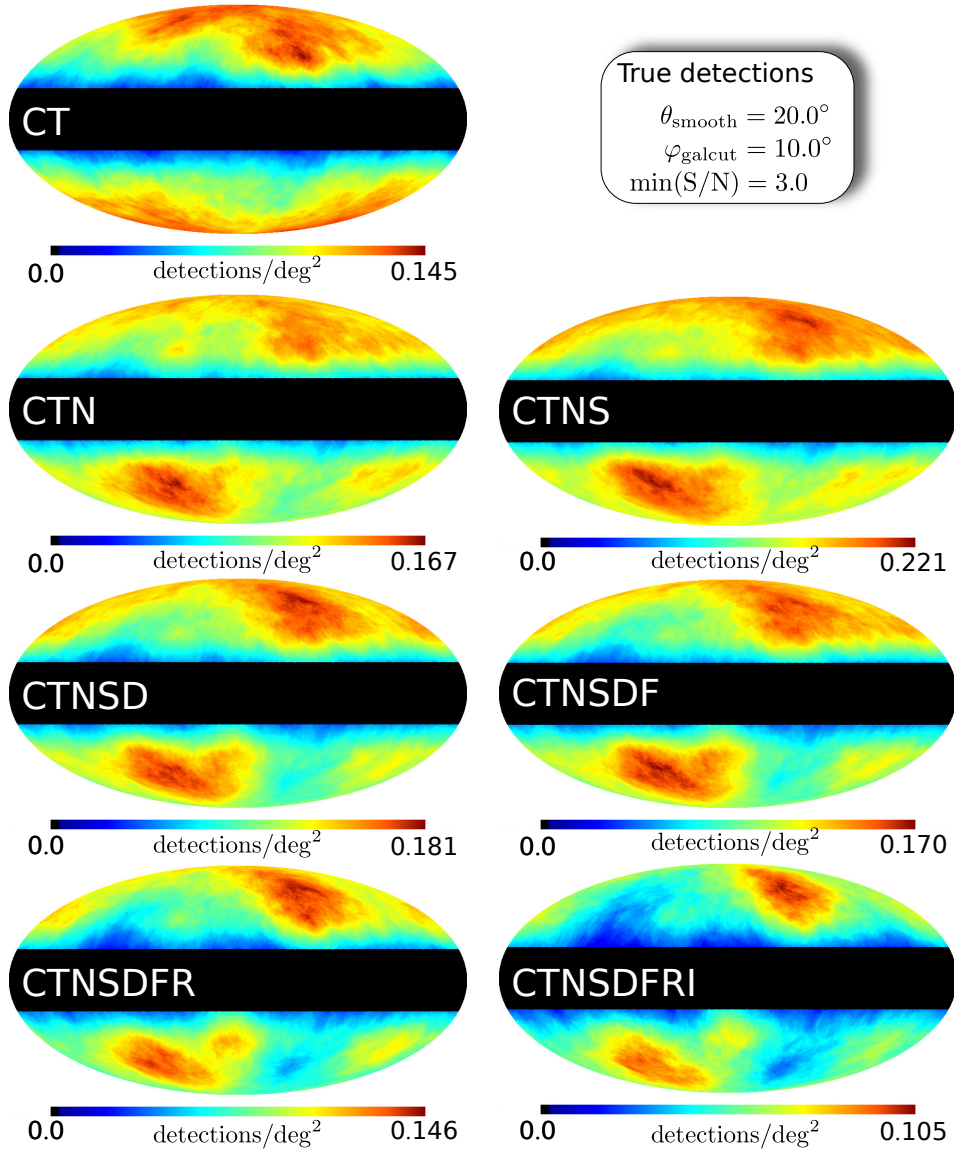


Figure 7.10: Spatial distribution of the false detections given in number of detections per square degree, averaged in as disc of size $\theta_{\text{disc}} = 20^\circ$. The black region depicts the Galactic cut of $\theta_{\text{cut}} = 10^\circ$ in which we do not consider detections due to the strong Galactic signal. The abbreviations for denoting the different co-added maps are: C (CMB), T (thermal SZ), S (synchrotron), D (dust), F (free-free), R (radio sources), I (infra-red sources). Note that the colour bars are individually different for the different maps.

these catalogues contain the position, redshift, mass, and Comptonisation of each individual cluster, simple cross-checking provides all the information needed. The result of this procedure is summarised in Fig. 7.11 and Fig. 7.12, respectively for

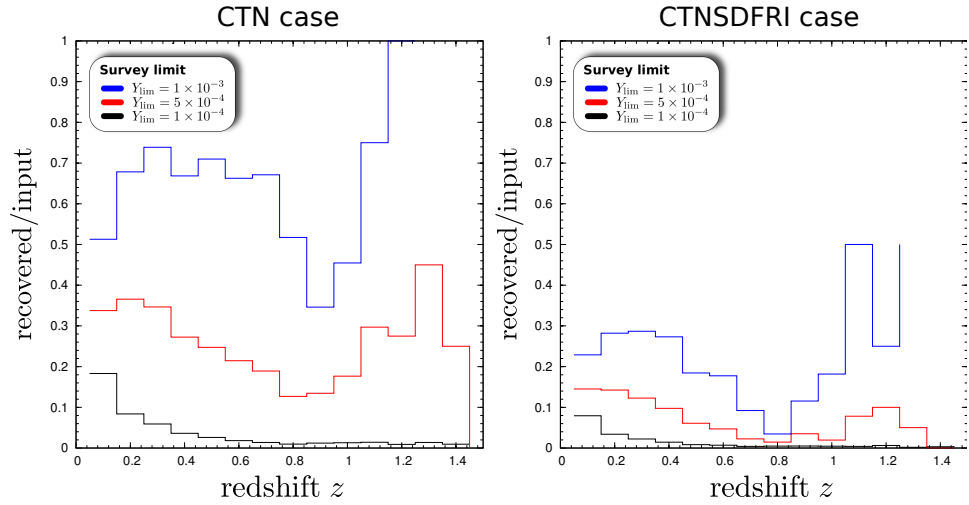


Figure 7.11: Selection functions with respect to redshift z for the CTN (left panel) and the CTNSDFRI case (right panel) for three different values of the limiting Comptonisation Y_{lim} , namely 1×10^{-4} arcmin² (black-line), 5×10^{-4} arcmin² (red line) and 1×10^{-3} arcmin² (blue line).

the redshift and mass dependence. When assessing the completeness, in mass or redshift bins, one has to specify a Y_{min} defining the in principle detectable sample. In our case, I computed the respective selection functions for three different values of Y_{min} , namely 1×10^{-4} arcmin², 5×10^{-4} arcmin² and 1×10^{-3} arcmin².

In Fig. 7.11, one can clearly see the difference between the idealised CTN and the rather realistic CTNSDFRI case. The overall performance is, as already indicated by the findings of Sect. 7.3.1, not very convincing. Apart from the low completeness in redshift bins, it seems also that systems with redshifts > 0.8 will barely be contained in the sample. The rise of completeness for $Y_{\text{lim}} = 10^{-3}$ arcmin² can be explained by the fact, that for such high Comptonisations, only very few systems exist at very high redshifts and thus an increase in completeness is a natural consequence.

The selection function in term of cluster mass, depicted in Fig. 7.12, shows as well the difference between the ideal CTN and the realistic CTNSDFRI scenario. Considering a completeness of 70%, the sample reaches out down to masses of $\sim 7 \times 10^{14} M_{\odot} h^{-1}$, whereas the CTNSDFRI sample only comprises systems with $M \gtrsim 1.5 \times 10^{15} M_{\odot} h^{-1}$. In general, the selection function in terms of cluster mass drops quite fast for the realistic simulations. Therefore, the sample will be rather incomplete concerning clusters with masses below $\sim \times 10^{15} M_{\odot} h^{-1}$.

7.3.4 The physical properties of the detected cluster sample

So far, I only discussed the size, contamination and selection function of the sMFMF-detected sample. However, since all the input information about the clusters is

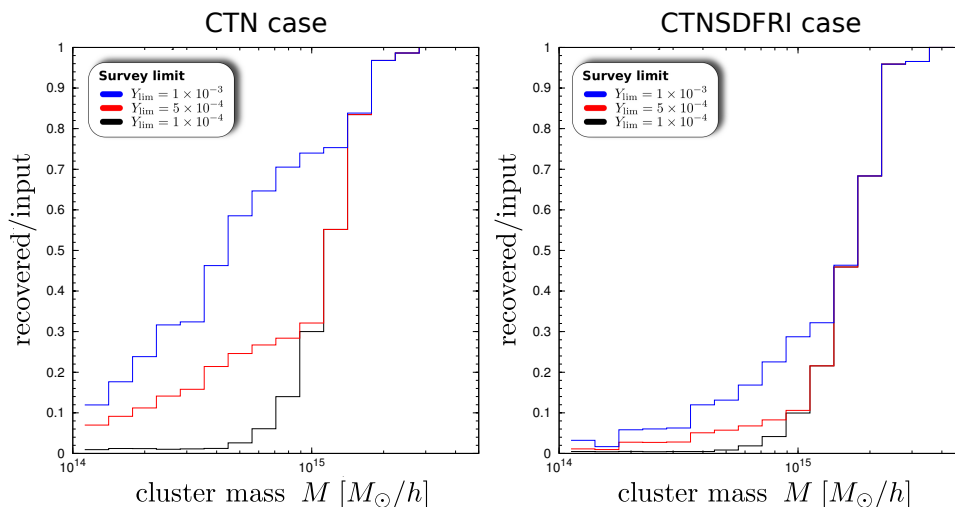


Figure 7.12: Selection functions with respect to cluster mass for the CTN (left panel) and the CTNSDFRI case (right panel) for three different values of the limiting Comptonisation Y_{lim} arcmin², namely 1×10^{-4} arcmin² (black-line), 5×10^{-4} (red line) and 1×10^{-3} arcmin² (blue line).

known, one can relate the S/N values from the filtering to the input values of the mass M , redshift z and the Comptonisation Y . The results are shown Fig. 7.13 for the mass-redshift relation of the detected sample. It can be seen, that the clusters populate the $\log(M) - z$ -plane in a well defined region. From the realistic CTNSDFRI case, depicted in the right panel, it can be inferred that only few systems are recovered at redshifts beyond $z \simeq 0.6$ with quite low significances. It is nice to see how the S/N values increase for increasing mass at a fixed redshift. Of course, it is interesting to relate the input Comptonisation Y_{input} with the recovered one Y_{recov} , as shown in Fig. 7.14. For reference, also the ideal one-to-one relation (black line) has been added. Especially for strong Comptonisations there seems to be small bias. This could probably be alleviated by imposing a stricter S/N threshold for both calibration and measurement. In Fig. 7.15, I also show that the input and recovered cluster sample populates the $Y - M$ -plane, for both the CTN and the CTNSDFRI cases. The perceptible slope stems from the $Y \propto M^{5/3}$ scaling relation. It is interesting to see how the filtering process softens the distinct relation between M , Y and z . For the high-redshift, high-mass systems the input distribution is completely destroyed by the filtering process, whereas at intermediate redshifts the distribution is widened but still in place.

7.4 Perspectives

The perspectives of the sMFMF filtering and of *PLANCK*'s cluster sample as a whole are not easy to rate. The filtering method is appealing and unmatched in

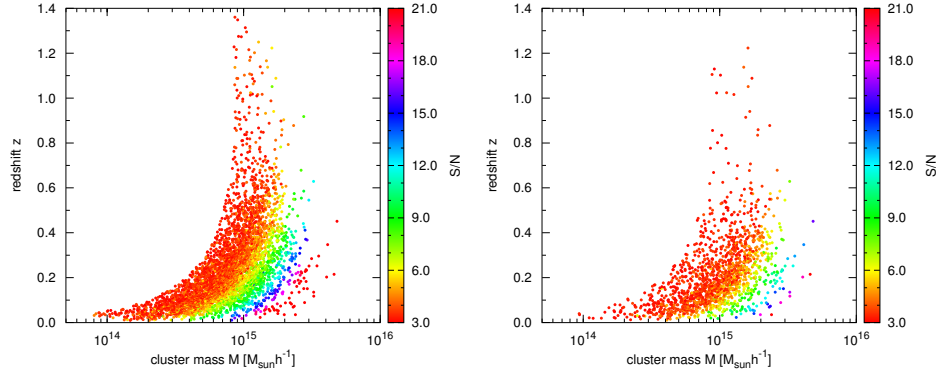


Figure 7.13: $M - z$ relation for the detected cluster sample for the idealistic CTN case and the realistic CTNSDFRI case, where all foreground components are contained. Each dot represents a detection of a galaxy cluster, where the colour of the dots denotes the signal-to-noise ratio (S/N) for the individual detection.

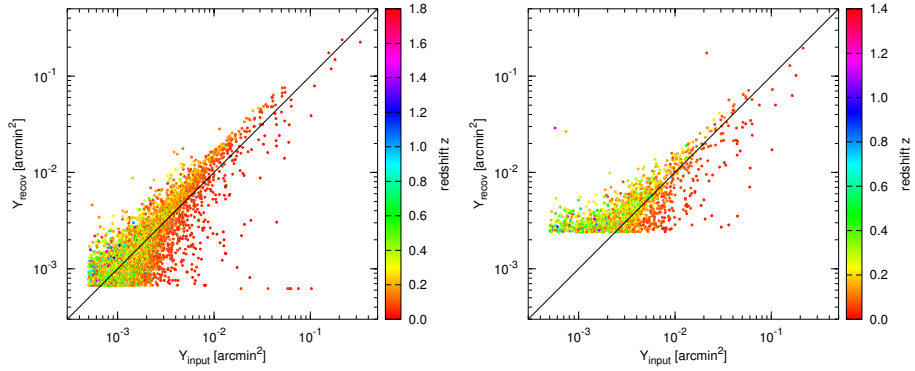


Figure 7.14: Relation between the by sMFMF filtering recovered Comptonisation, Y_{recov} , and the input Comptonisation, Y_{input} , for the idealistic CTN case and the realistic CTNSDFRI cases. the black, solid line represent the perfect linear one-to-one relation. Each dot represents a detection, where the colour stands for the redshift of the detected cluster, as known from the input catalogue.

7.4. Perspectives

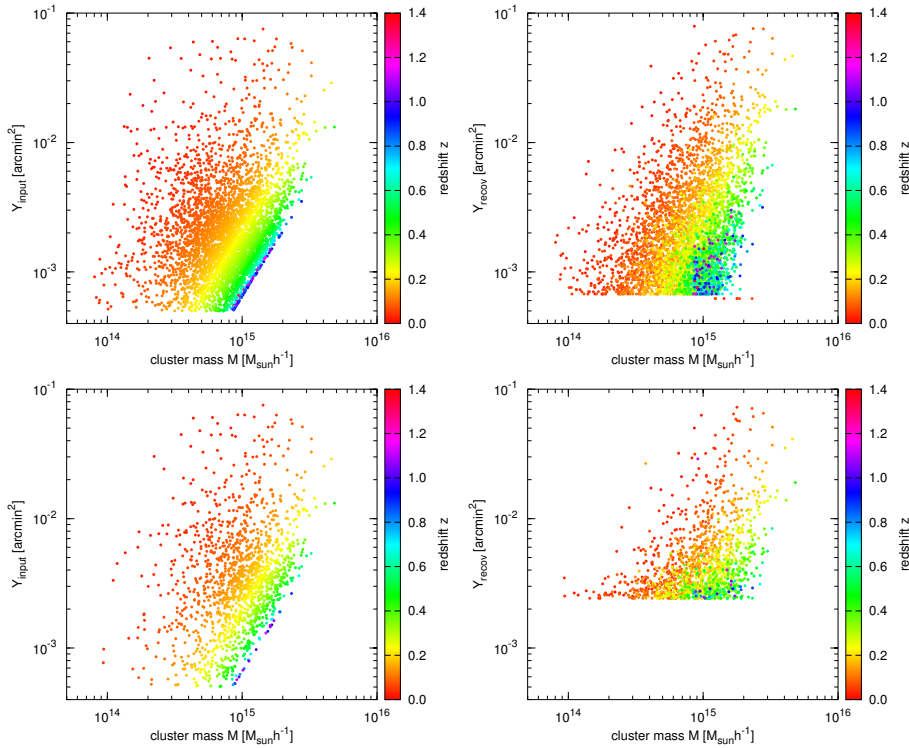


Figure 7.15: $Y - M$ relations for the input (left column) and the recovered Y (right column) for the idealistic CTN case (upper row) and the realistic CTNSDFRI case (lower row). Each dot denotes a detection and the colour illustrates the redshift of the detected cluster, as given by the input cluster catalogue.

its elegance. Being formulated in the spherical harmonic space and acting on the full-sky maps, it can be immediately applied to the reduced maps after the de-striping has been done. Methods working on patches in flat space have to tile the sphere causing multiple detections in the overlapping boundaries and are more complicated to deal with. On the other hand, the global noise estimate causes long-wavelength modes in the detection maps giving rise to a non-isotropic distribution of the detections. Methods estimating the noise locally do not principally suffer from this drawback.

Nevertheless, strong efforts in testing, developing and implementing a number of different cluster detection algorithms in the framework of the *PLANCK* cluster challenge (Melin et al., [in prep.]) led to the conclusion that, with no algorithms the initially anticipated number of galaxy clusters can be found. The reasons for this discrepancy, already mention in Subsect.7.3.1, are complex, ranging from the drop of the initially higher value of $\sigma_8 = 0.85$ down to $\sigma_8 = 0.796$, a 15% lower normalisation of the $Y - M$ -relation and the preference of a more peaked modified NFW pressure profile over the β -profile from recent X-ray observations. In contrast to the lower normalisation, the more peaked profile should increase the

Chapter 7. Studying SZ cluster with PLANCK

detectability. Moreover, previous studies (e.g. Schäfer et al. (2006b) and Schäfer & Bartelmann (2007)) usually completely omitted the point source contamination, which has been shown in this work to be a major source of concern.

Even though *PLANCK*'s SZ cluster sample will stay behind the initial expectations by one order of magnitude, a survey yield of 1000 – 2000 clusters could be compiled by using different search algorithms and follow-up observations to remove false-positives. In view of this, one should keep in mind that the *PLANCK* SZ survey is the first full-sky SZ survey since the ROSAT All-Sky Survey (RASS) (Truemper 1992). One could say that we will definitely learn more about galaxy clusters but the time of cluster cosmology has not yet come.

Bottom line - What to take away

- We implemented a filtering and cluster detection pipeline based in the spherical multi-frequency matched filtering (sMFMF), a method working fast and on the full-sky.
- The newly implemented `clustFind_cxx` module is fast and reliable in finding peaks in the S/N maps that can be identified as clusters. The method is versatile enough to be applied to all peak-finding problems on spherical domains.
- In order to characterise the impact of the different foreground components on the filter performance, namely the contamination and completeness of the detected samples, I created a collection of individually co-added maps.
- It turns out that synchrotron and free-free emission only mildly affect the filter performance, whereas dust emission as well as source emission in the radio and infra-red regimes cause a significant drop in size and quality of the detected sample.
- Furthermore, we found that the detected clusters are not uniformly distributed on the sky but happen to be detected, where the noise suppression is smallest. Thus, the presence of noise helps the filters.
- The cluster sample will mainly reside on the high-mass and low-intermediate redshift side.
- We have been able to calibrate the filtering method to obtain a acceptable Y recovery.
- Judging the overall performance for realistic cases, the results are not too promising. Instead of $\sim 10^4$ clusters it will be realistic to find around ~ 1000 clusters, substantially limiting the impact of the SZ survey on cosmological studies.

The theory of our modern technic shows that nothing is as practical as theory.

Julius Robert Oppenheimer
(1904-1967)

8

Spherical collapse in dark energy cosmologies

In the past it was believed (Bartelmann et al. 2006; Sadeh et al. 2007) that the presence of a dark energy component at early times could significantly lower the spherical collapse parameter δ_c and therefore lead to an increase in the number of collapsed high-mass objects in the Universe with respect to Λ CDM. However, numerical simulations and analytic works (Francis et al. 2009b,a; Grossi & Springel 2009) raised doubts about the validity of these results. Motivated by these findings we (Pace et al. 2010) decided to study analytically the spherical collapse based on a hydrodynamic approach for several dark energy scenarios. The findings of this work are discussed in the following sections of this chapter starting with the discussion of Newtonian hydrodynamics of a relativistic fluid in Sect. 8.1 and a comparison of the linear with the non-linear evolution of a spherical overdensity in Sect. 8.2. The results for the collapse parameters are presented in Sect. 8.3, followed by a study of the volume effects in Sect. 8.4. Thereafter, the conclusions that can be drawn are summarised in Sect. 8.5 and a short bottom line is given at the end.

8.1 Newtonian hydrodynamics of a relativistic fluid

In order to perform a general study of spherical collapse, we decided to study a generic collapse geometry, containing spherical and ellipsoidal collapse as special cases. Furthermore, we were interested in a time-dependent equation-of-state and we did not want to omit pressure terms. In order to derive a differential equation governing the evolution of the overdensity δ in a fluid that satisfies the equation-of-state $P = w\rho c^2$, we followed Abramo et al. (2007).

Starting point for our considerations is the continuity equation of the stress-energy tensor in general relativity $\nabla_\nu T^{\mu\nu} = 0$, where in the case of a perfect fluid we have

$$T^{\mu\nu} = (\rho c^2 + P)u^\mu u^\nu + P g^{\mu\nu}, \quad (8.1)$$

where ρ is the density of the fluid, P the pressure, u the 4-velocity and $g^{\mu\nu}$ the metric. In the weak field limit, where the gravitational potential is small $\Phi \ll c$

Chapter 8. Spherical collapse in DE cosmologies

and the time variation of the potential is small, the metric can be rewritten as

$$ds^2 = g_{\mu\nu}dx^\mu dx^\nu = (1 + 2\Phi)dt^2 - (1 - 2\Phi)\delta_{ij}dx^i dx^j, \quad (8.2)$$

where Φ the Newtonian gravitational potential and i, j range from 1 to 3 denote the spatial coordinates. From the relations above we can derive the relativistic expressions for the continuity and Euler equations, by contracting first with u_μ and then with the projection-operator $g_{\mu\alpha} + u_\mu u_\alpha$, leading to

$$\frac{\partial \rho}{\partial t} + \nabla_{\mathbf{r}} \cdot (\rho \mathbf{v}) + \frac{P}{c^2} \nabla_{\mathbf{r}} \cdot \mathbf{v} = 0, \quad (8.3)$$

$$\frac{\partial \mathbf{v}}{\partial t} + (\mathbf{v} \cdot \nabla_{\mathbf{r}}) \mathbf{v} + \nabla_{\mathbf{r}} \Phi + \frac{\nabla_{\mathbf{r}} P + \frac{\mathbf{v}}{c^2} \frac{\partial P}{\partial t}}{\rho + \frac{P}{c^2}} = 0. \quad (8.4)$$

In these equations \mathbf{r} is the physical coordinate and \mathbf{v} denotes the 3-velocity. The gravitational potential and the pressure are related by means of the relativistic Poisson equation that reads

$$\nabla^2 \Phi = 4\pi G \left(\rho + \frac{3P}{c^2} \right). \quad (8.5)$$

and which can be derived from the 0-0 component of Einstein's field equations. From the space components of Einstein's equation one obtains the continuity equation for the mean background density, which is then modified to

$$\dot{\bar{\rho}} + 3H \left(\bar{\rho} + \frac{P}{c^2} \right) = 0, \quad (8.6)$$

in which $\bar{\rho} = 3H^2 \Omega_{\text{fluid}} / 8\pi G$ denotes the background mass density of all contributions to the cosmic fluid, and Ω_{fluid} is its density parameter. In order to adapt those equations to our cosmological framework, one introduces comoving coordinates $\mathbf{x} = \mathbf{r}/a$, defining

$$\rho(\mathbf{x}, t) = \bar{\rho}(1 + \delta(\mathbf{x}, t)), \quad (8.7)$$

$$P(\mathbf{x}, t) = w\rho(\mathbf{x}, t)c^2, \quad (8.8)$$

$$\Phi(\mathbf{x}, t) = \Phi_0(\mathbf{x}, t) + \phi(\mathbf{x}, t), \quad (8.9)$$

$$\mathbf{v}(\mathbf{x}, t) = a[H(a)\mathbf{x} + \mathbf{u}(\mathbf{x}, t)], \quad (8.10)$$

here $\mathbf{u}(\mathbf{x}, t)$ is the comoving peculiar velocity and $H(a)$ is the Hubble function. By inserting the definitions above into Eqs. 8.3–8.5, one obtains the following equations

$$\dot{\delta} + (1+w)(1+\delta)\nabla_{\mathbf{x}} \cdot \mathbf{u} = 0, \quad (8.11)$$

$$\frac{\partial \mathbf{u}}{\partial t} + 2H\mathbf{u} + (\mathbf{u} \cdot \nabla_{\mathbf{x}})\mathbf{u} + \frac{1}{a^2}\nabla_{\mathbf{x}}\phi = 0, \quad (8.12)$$

$$\nabla_{\mathbf{x}}^2 \phi - 4\pi G(1+3w)a^2\bar{\rho}\delta = 0. \quad (8.13)$$

8.1. Newtonian hydrodynamics of a relativistic fluid

In order to continue from this point, one has to remember that one is interested in obtaining a single differential equation for δ , which means finding a way of combining the three equations above. The recipe that leads to success is to take the divergence of the Euler equation Eq. 8.12 and to recall the decomposition

$$\nabla \cdot [(\mathbf{u} \cdot \nabla)\mathbf{u}] = \frac{1}{3}\theta^2 + \sigma^2 - \omega^2, \quad (8.14)$$

into the expansion $\theta = \nabla_{\mathbf{x}} \cdot \mathbf{u}$, the shear tensor $\sigma^2 = \sigma_{ij}\sigma^{ij}$ and the rotation tensor $\omega^2 = \omega_{ij}\omega^{ij}$. It should be mentioned that the shear is a symmetric traceless tensor, while the rotation is antisymmetric. They read

$$\sigma_{ij} = \frac{1}{2} \left(\frac{\partial u^j}{\partial x^i} + \frac{\partial u^i}{\partial x^j} \right) - \frac{1}{3} \theta \delta_{ij}, \quad (8.15)$$

$$\omega_{ij} = \frac{1}{2} \left(\frac{\partial u^j}{\partial x^i} - \frac{\partial u^i}{\partial x^j} \right). \quad (8.16)$$

In doing so, one can, by taking the time derivative of the continuity equation Eq. 8.11 and by combining all three equations above, arrive at the fully non-linear evolution equation

$$\begin{aligned} \ddot{\delta} + \left(2H - \frac{\dot{w}}{1+w} \right) \dot{\delta} - \frac{4+3w}{3(1+w)} \frac{\delta^2}{1+\delta} - 4\pi G \bar{\rho} (1+w)(1+3w)\delta(1+\delta) - \\ (1+w)(1+\delta)(\sigma^2 - \omega^2) = 0. \end{aligned} \quad (8.17)$$

This general equation can be specialised to dust ($w = 0$), which is consistent with equation Eq. (41) of Ohta et al. (2003). Further, one should notice that Eq. 8.17 generalises Eq. (7) of Abramo et al. (2007) to the case of a non-spherical configuration of a rotating fluid, which is however not subject of this work.

In order to arrive at a more convenient form of Eq. 8.17, it is useful to change the independent variable from the time t to the scale factor a . Taking account of the relation $\partial_t = aH(a)\partial_a$, one can write the evolution equation in the following way

$$\begin{aligned} \delta'' + \left(\frac{3}{a} + \frac{E'}{E} - \frac{w'}{1+w} \right) \delta' - \frac{4+3w}{3(1+w)} \frac{\delta^2}{1+\delta} - \\ \frac{3}{2} \frac{\Omega_{\text{fluid},0}}{a^2 E^2(a)} g(a)(1+w)(1+3w)\delta(1+\delta) - \\ \frac{1}{aH^2(a)} (1+w)(1+\delta)(\sigma^2 - \omega^2) = 0, \end{aligned} \quad (8.18)$$

here $\Omega_{\text{fluid},0}$ denotes the density parameter of the fluid at $a = 1$, and $g(a)$ is a function specifying the time evolution of the dark energy model considered.

Chapter 8. Spherical collapse in DE cosmologies

For all what follows, we are assuming the collapse of a homogeneous sphere, ignoring rotation and the shear tensors, where the latter vanish for a sphere anyway. Since the treatment of the spherical collapse as discussed so far did not specify $w(a)$ at all, naturally the question on what happens in the case of a cosmological constant given by $w = -1$ arises. The fact that the cosmological constant is not expected to clump should be recoverable from Eq. 8.18 above, and indeed by multiplying both sides with $1 + w$ and then specialising to $w = -1$ and the rotation and shear free spherical case, one obtains $\delta'^2/(1 + \delta) = 0$. This implies that $\delta = \text{const}$, where the constant can always be set to zero by specifying the appropriate initial conditions. Furthermore the discussion is restricted to the case of a spherical perturbation filled with dust, where $w = 0$ and $g(a) = a^{-3}$, such that the evolution equation simplifies to

$$\delta'' + \left(\frac{3}{a} + \frac{E'}{E} \right) \delta' - \frac{4}{3} \frac{\delta'^2}{1 + \delta} - \frac{3}{2} \frac{\Omega_{m,0}}{a^5 E^2(a)} \delta(1 + \delta) = 0. \quad (8.19)$$

which can be linearised and reads then

$$\delta'' + \left(\frac{3}{a} + \frac{E'}{E} \right) \delta' - \frac{3}{2} \frac{\Omega_{m,0}}{a^5 E^2} \delta = 0. \quad (8.20)$$

At this point, it is convenient to mention that the different forms of the non-linear evolution equation as derived above have already been used in previous studies of structure formation (Padmanabhan 1996; Abramo et al. 2007), and, furthermore, for the cases of spherical and ellipsoidal collapse (Bernardeau 1994; Ohta et al. 2004, 2003). The linearised equation was presented in Coles & Lucchin (2002) specialised for two limiting cases, namely dust ($w = 0$) and relativistic matter ($w = 1/3$), and in Lima et al. (1997) for a general model with constant w . The novel aspects of the preceding discussion are that, first, the evolution equation was generalised to a generic collapse geometry and, second, that the newly obtained generality of the method allows its possible application to modified-gravity cosmologies and coupled-quintessence models in the future.

8.2 Spherical collapse - Linear vs. non-linear evolution

Due to the considerations carried out in the previous section, we have now the tools to study the actual collapse in more detail and to derive quantities that we will need later to model cosmic structure formation. The equations 8.19 and 8.20 allow us to follow the non-linear and the linear evolution of a collapsing sphere, where the latter is of peculiar interest since it will allow us to infer the *linear* overdensity parameter at any point in time. It should be mentioned that Eq. 8.20 is identical with the differential equation that has to be solved for obtaining the time evolution of the growth factor 1.21 if suitable initial conditions are used.

In order to determine the appropriate initial conditions for the linear evolution equation, one has to go back to the non-linear one. Due to its non-linearity, we

8.2. Spherical collapse - Linear vs. non-linear evolution

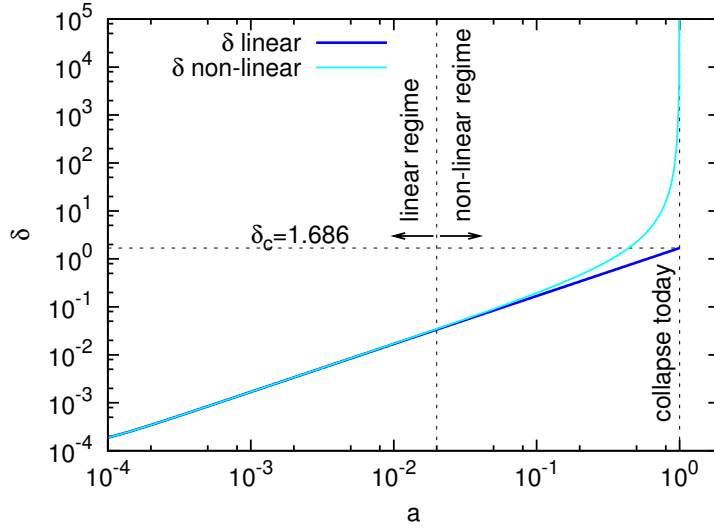


Figure 8.1: Linear (blue, dashed curve) and non-linear (cyan, short-dashed curve) evolution of the overdensity parameter δ . An EdS model and a sphere collapsing at $z = 0$ are assumed. We notice how, after the initial parallel evolution, the non-linear solution grows very fast with the scale factor, in comparison to the linear solution.

expect that at the time of collapse the density contrast diverges $\delta \rightarrow \infty$, allowing us to find the appropriate initial conditions. To do so, we search for those initial conditions, ensuring that the δ solving the non-linear equation diverges at the chosen collapse time. The numerical divergence of δ is assumed to be achieved if $\delta \geq 10^7$ is fulfilled. However, due to the fact that the functional behaviour $\delta(a)$ representing the non-linear density evolution steepens significantly towards the collapse, the result is very insensitive to the exact choice of this threshold value as long as it is a large number. As soon as the search for the initial overdensity was successful, one can use this value in Eq. 8.20 to solve for the critical linear density contrast δ_c . Since the evolution equations are of second order, one has to specify two different initial values: first, the initial overdensity δ_i and second, the initial rate of evolution, δ'_i . Obviously, in the beginning the rate of evolution for the sphere should be small, and is therefore set to a small number $\delta'_i = 5 \times 10^{-5}$, corresponding to the initial scale factor used for starting the integration of the two differential equations. We carried out several numerical tests to check the dependence of the solution on δ'_i and found that the result does not depend on the precise value of δ'_i . Specifically, we considered several values in the interval between 10^{-6} and 10^{-4} and saw perfect convergence of the solution. Also setting $\delta'_i = 0$, the result does not change considerably. To ensure convergence of the result, we repeated the scheme above for many different initial values in the interval between 10^{-6} and 10^{-4} and we found out that the result does not depend on the precise value of δ'_i , such that even setting $\delta'_i = 0$ does not change the result considerably. The results of our

solution scheme for the case of an EdS model are presented in Fig. 8.1, where the evolution of δ with scale factor is shown for the non-linear (cyan, short-dashed curve) and the linear (blue, dashed curve) case. Demanding that the sphere collapses today ($a = 1$), we find that the linear solution grows as expected linearly with time, reaching the correct value for $\delta_c = 1.686$ at the collapse scale factor, while the non-linear solution after evolving initially in parallel diverges exponentially at late times. Of course, in reality collapse does not proceed to infinity, but a virial equilibrium, as depicted in the centre of the schematic drawing Fig. 2.1, is reached before. To obtain the virial overdensity, supposing that dark energy does not clump, we follow the prescription of Maor & Lahav (2005), which generalises the work by Wang & Steinhardt (1998).

Knowing the non-linear time evolution, it is possible to infer all the other properties of the collapsing sphere, in particular the time evolution of the radius, the turnaround scale factor a_{ta} when the sphere reaches its maximum radius (depicted by the black circle in Fig. 2.1), and the overdensity at turnaround ζ . The virial overdensity is defined as

$$\Delta_V = \delta_{\text{nl}} + 1 = \zeta (x/y)^3, \quad (8.21)$$

where $x = a/a_{\text{ta}}$ is the normalised scale factor and y is the radius of the sphere normalised to its value at the turnaround.

To determine the turnaround scale factor, we solve Eq. 8.19 and determine the quantity $\log(\delta_{\text{nl}} + 1)/a^3$. Apart from a multiplicative constant, this is the inverse of the collapsing sphere's radius and assumes a minimum at the turnaround scale factor a_{ta} . This can be seen by taking the logarithm of Eq. 8.21 and by recasting the terms. To determine the virial overdensity at turnaround ζ , we integrate Eq. 8.19 up to a_{ta} and add the result to unity.

8.3 Results for the collapse parameters

After applying the above method to the EdS test-case, the next step is to apply it to the plethora of dark energy models introduced in Chap. 3, including the reference Λ CDM model. In doing so, one obtains the collapse parameters, namely the linear overdensity parameter and the virial overdensity.

Our main results are shown in Fig. 8.2. The right panels show results for the virial overdensity $\Delta_V(z)$, while the left panels are specialised to the linear overdensity δ_c . The upper panels refer to the quintessence models, the middle panels refer to the (generalised) Chaplygin gas and to a cosmology with Casimir effect taken into account. The lower panels show results for the models with a constant equation-of-state parameter (non-flat Λ CDM model, topological defects and phantom models). The line-style labels are explained in the caption of the figure.

From Fig. 8.2, it is quite evident that all models considered, including the EDE cosmologies discussed in the appendix, behave very similarly to the flat Λ CDM cosmology, irrespective of the equation-of-state parameter, be it constant or varying with time. At $z = 0$, the difference in δ_c is at most of 2% for the generalised

8.3. Results for the collapse parameters

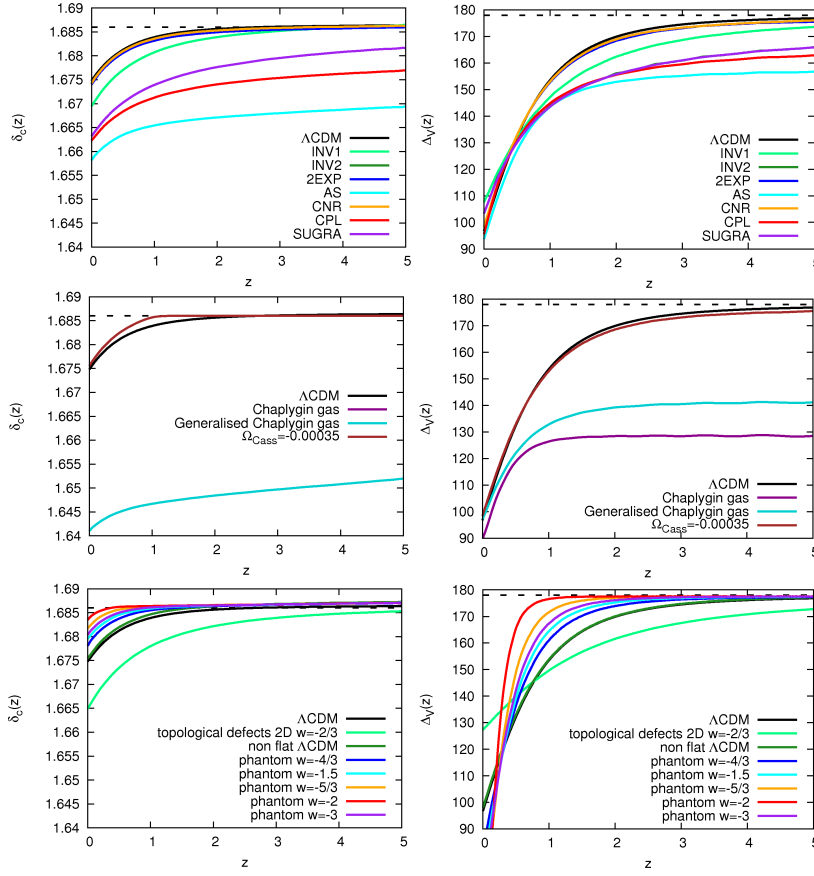


Figure 8.2: The left panels show the time evolution of the linear overdensity $\delta_c(z)$, the right panels the time evolution for the virial overdensity $\Delta_V(z)$ for the different classes of models. In all panels, the Λ CDM solution (black, solid curve) is the reference model, while the black, dashed, horizontal curve is the EdS model that is reached asymptotically by all the models. The upper panels present the quintessence models: the INV1 (INV2) model is shown with the light-green, dashed (dark-green, short-dashed) curve, the 2EXP model with the blue, dotted curve, the AS model with the cyan, dot-dashed curve, the CPL (CNR) model with the red, dot-dotted (orange, dot-short-dashed) curve and finally the SUGRA model with the violet, dot-dot-dashed curve. The middle panels show the Casimir effect (brown, dotted curve) and the (generalised) Chaplygin gas with the (turquoise, short-dashed) magenta, dashed curve. Finally, the lower panels report the solution for the models with constant equation-of-state parameter: the dark-green, short-dashed curve stands for the non-flat Λ CDM model, the light-green, dashed curve for the model with $w = -2/3$, the blue, dotted curve represents the model with $w = -4/3$, the cyan, dot-dashed curve the model with $w = -1.5$, the orange, dot-short-dashed curve the model with $w = -5/3$, the red, dot-dotted curve the model with $w = -2$ and, finally, the violet, dot-dot-dashed curve shows the model with $w = -3$.

Chaplygin gas, while for the very large majority it is even less. All models asymptotically approach the EdS limit at high redshift. This result, that all models give essentially the same results, is quite important: it shows that the linear density threshold δ_c , from the Λ CDM model is very close to the precise value in other cosmologies even if the equation-of-state parameter considerably differs from $w = -1$. We argue that a possible enhancement in structure formation might be caused by rapidly varying or discontinuous equation-of-state parameters, for example if they contain bumps or peaks. From a physical point of view, huge differences from the Λ CDM models might result from modified-gravity scenarios, such as coupled dark energy models.

It is also interesting to notice that the equation-of-state parameter has very little impact on the evolution of δ_c . We argue that this can be attributed to the fact that the equation-of-state parameter is always integrated over and thus its effects are smoothed over cosmic history. It would be interesting to work out, with the equations governing the evolution of the overdensity, which conditions must be satisfied by the equation-of-state parameter to have significant effects on δ_c .

The same considerations apply to the virial overdensity, Δ_v . Deviations at low redshift are at most of the order of a few percent, thus having negligible impact on non-linear structure evolution. This fact has also a practical advantage: all quantities depending on Δ_v will be virtually unaffected if the virial overdensity of the Λ CDM model is used as an approximation.

8.4 Volume effects

In the previous section, we studied the impact of different dark energy models on the linear overdensity threshold δ_c . A quantity closely related to observations is the mass function, representing the number of collapsed objects per unit mass and volume. Since it only depends on δ_c and on the growth factor, no appreciable differences are expected between the models studied. An important quantity that can be derived from observations is the total number of haloes above a given mass in a complete survey volume. The minimum mass detectable in a survey is generally a function of redshift and changes with the observed wave band; moreover, it will also depend on the survey according to the instrument sensitivity. Since we do not intend to specify an individual survey here, we assume the minimum mass to be independent of redshift. An idealisation in this approach is that the catalogue of objects is considered to be complete in order to compare observations with theoretical predictions.

The cumulative number of haloes above a given mass M_h is

$$N(> M_h) = \int_{M_{\min}}^{\infty} dM \int_{z_1}^{z_2} \frac{dn}{dM dV} \frac{dV}{dz} dz, \quad (8.22)$$

where $dn/dM dV$ represents the differential mass function and dV/dz the volume element. Since dark energy does not only affect the growth history but also the geometry, we expect that the contribution of volume effects on observable quantities

8.4. Volume effects

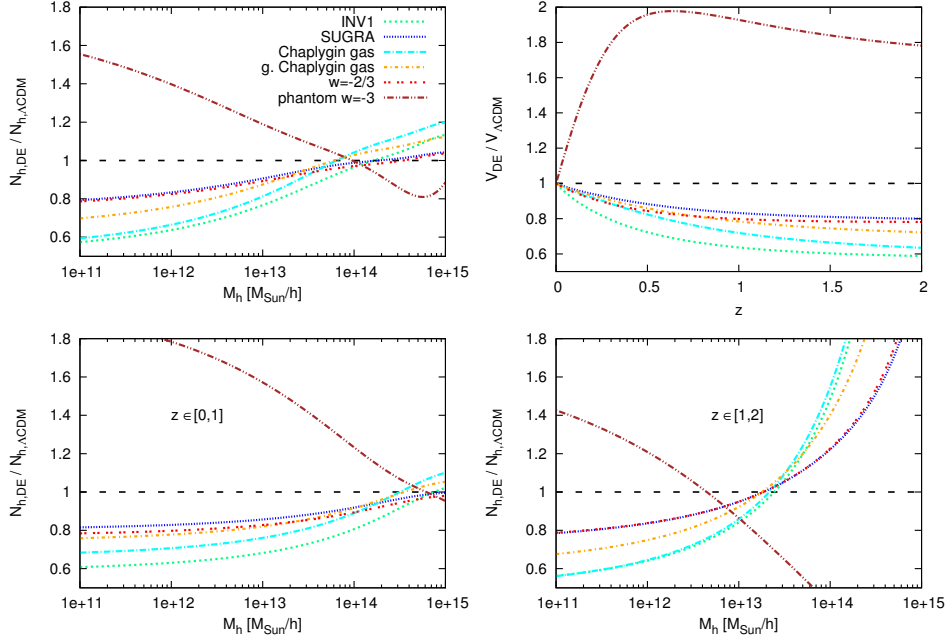


Figure 8.3: Volume effects on halo number counts. The top left panel shows the cumulative mass function between $z = 0$ and $z = 2$ normalised with the expected value of the Λ CDM model. The top right panel shows the volume as a function of redshift compared to the volume of a Λ CDM model. The lower panels present the different contributions to the number counts in two redshift bins, between $z = 0$ and $z = 1$ and between $z = 1$ and $z = 2$ in the left and right panels, respectively. Different colours refer to different dark energy models. Green, short-dashed: INV1; blue, dotted: SUGRA; (orange, dot-short-dashed) cyan, dot-dashed: (generalised) Chaplygin gas; red, dot-dotted (brown, dot-dot-dashed): phantom model with $w = -2/3$ ($w = -3$).

will provide more information than merely the differential mass function. Effects on the number of observable haloes are shown in Fig. 8.3. In the top left panel, we show the ratio of the cumulative mass function above a given mass integrated between $z = 0$ and $z = 2$ between some of the dark energy models studied and the reference Λ CDM model. The top right panel shows the volume effect for the corresponding models, i.e. the ratio between the volumes of the dark energy and the Λ CDM models. In the bottom panels, we show the contribution to the number counts in spherical shells enclosing a volume between $z = 0$ and $z = 1$ (left panel) and $z = 1$ and $z = 2$ (right panel). Please, see the figure caption for details on the models considered.

In the Press & Schechter formalism, the cosmological information, and hence the dark energy contribution, is contained in the quantity $\delta_c(z)/D(z)$, where $D(z)$ is the growth factor. To compare the different models, we thus fix the variance

Chapter 8. Spherical collapse in DE cosmologies

for the Λ CDM model ($\sigma_8 = 0.8$) and scale the variance of the dark energy models according to (see also Abramo et al. 2007)

$$\sigma_{8,DE} = \frac{\delta_{c,DE}(z=0)}{\delta_{c,\Lambda\text{CDM}}(z=0)} \sigma_8. \quad (8.23)$$

Due to the relatively small differences in terms of δ_c , the normalisations differ by a few percent at most.

Even if the differential mass functions differ only slightly, we note that differences in the number counts are as large as 40% – 60%. This is mainly due to volume effects, as shown in the top right panel of Fig. 8.3. Models with a non-phantom equation-of-state always have a smaller volume than the Λ CDM model because the expansion rate is lower, while the opposite holds for phantom models (dot-dot-dashed, brown curve). Since differences in the mass function are expected only in the high-mass tail, we can safely assume that the number of small objects is approximately the same for all the models. Thus, for low mass haloes, the non-phantom dark energy models predict fewer objects, but for objects above $\approx 10^{14} M_\odot/h$, the exponential tail of the mass function compensates the smaller volume, and we see that a larger number of high-mass objects is expected. Of course, for the phantom models, the results are reversed. We expect more objects at low mass and fewer at high mass, since they do not have time to assemble.

From an observational point of view, it is also interesting to determine in which redshift interval we expect the highest contribution. This is shown in the lower panels. We normalise to the Λ CDM counts integrated over the same redshift interval as the dark energy models, thus the sum of the two panels does not reproduce the top left panel. It is clear from the bottom right panel that the major contribution comes from high redshifts, while we do not expect more than 10% difference from the volume up to $z = 1$. Once again, for the phantom models, the situation is reversed.

Despite the fact that differences in number counts are not negligible and systematic, we have to recall that they are of the same order of magnitude as the uncertainty in the determination of halo masses. It will therefore still be difficult to discriminate between the models studied.

8.5 Conclusions

Even though the beginning of the theoretical studies of spherical collapse dates back several decades, see e.g. for reference Peebles (1980), it can still be considered as a current topic of research in modern Cosmology. Following the hydrodynamic approach, we derived the non-linear evolution equation Eq. 8.18, generalising the evolution equation to a generic collapse geometry, rendering the spherical and ellipsoidal models special cases. Moreover, the newly obtained generality of the method would allow also possible application to modified-gravity cosmologies and coupled-quintessence models. In the latter case the continuity equation for the stress-energy tensor would be modified to $\nabla_\nu T_{DM}^{\mu\nu} = Q^\nu$ and $\nabla_\nu T_{DE}^{\mu\nu} = -Q^\nu$, where

the 4-vector Q^ν governs the energy-momentum transfer between the dark components, resulting in modified collapse equations.

Solving the linear and non-linear evolution equations for a variety of dark energy models, we found that irrespective of the equation-of-state parameter of the considered cosmologies, the collapse parameters δ_c and Δ_V are very close to the Λ CDM case and, therefore, structure formation is almost unchanged. Hence, the conclusions drawn on the thermal Sunyaev-Zel'dovich effect (Sadeh et al. 2007; Waizmann & Bartelmann 2009), lensing (Fedeli & Bartelmann 2007; Fedeli et al. 2008) and clustering (Fedeli et al. 2009) are based on erroneous assumptions.

Despite the fact that we found the differences in the collapse parameters to be small for the different cosmological models, and therefore the differential mass functions basically to be indistinguishable, there is still an observable difference in the actual number counts of objects in a given volume above a given mass threshold. This effect, however, does not stem from an altered structure formation but from a different geometrical evolution in those cosmologies. At the low end of the minimum mass, the volume effects dominate and we expect a lower overall number of objects, while the mass function dominates over the volume effect at the high-mass tail, and we still expect more haloes. Unfortunately, as shown in the lower panels of Fig. 8.3, the major contributions come from redshifts above $z = 1$, where fewer objects are expected and where observations are more difficult, such that future high-redshift surveys have to be waited for.

In the considerations presented in this chapter, we exclusively assumed non-clustering dark energy models, meaning that dark matter is the only clustering component. Of course, there are more general scenarios in which also perturbations in the dark energy component can occur, having a non-negligible effect on structure formation (Abramo et al. 2007). A non-homogeneous dark energy component, present as a change in the equation-of-state of the dark energy fluid as the collapse proceeds and therefore possibly dependent on the actual overdensity, will add an additional degree of freedom, that can be parametrised by the effective sound speed $c_{s,\text{eff}}^2 = \delta P / \delta \rho$. It has been shown (Abramo et al. 2008, 2009) that a negative effective sound speed c_s^2 can lower the value of δ_c to $\approx 1.5 \dots 1.55$, giving a substantial boost to structure formation, which could leave observable imprints that would allow a clear distinction from the reference Λ CDM model.

To summarise one can say that in the near future pure number counts are not the method of choice to discriminate between different models of dark energy. However, there is still hope to use for this purpose either future high-redshift surveys or geometrical tests.

Bottom line - What to take away

- We studied the spherical collapse model for several dark energy scenarios using the fully non-linear differential equation for the evolution of the density contrast within homogeneous spherical overdensities derived from Newtonian hydrodynamics.
- It turned out that the collapse parameters δ_c and Δ_V are barely affected by the different dark energy models.
- Despite structure formation being rather insensitive to the different dark energy scenarios, the model could be constrained, due to volume effects, by counting objects in volume or geometrical tests.

The most exciting phrase to hear in science, the one that heralds new discoveries, is not "Eureka!" but "That's funny..."

Isaac Asimov (1920-1992)



SZ power spectra in dark energy cosmologies

The main part of the work presented so far always considered galaxy clusters as individual objects that can be detected by the SZ effect, characterised in terms of their physical properties and counted. By means of such a compiled cluster sample, one could infer cosmological information. Another approach is to abandon the idea to study clusters as individual cosmic objects and to study the cluster population as a whole by measuring a single quantity. This quantity, is in the current case, the angular SZ power spectrum. The advantage of the angular SZ power spectrum is, that it is easier to detect than individual clusters in the field that it is insensitive to observational selection effects and that it does not require a calibration between cluster mass and flux. However, for modelling the observed spectra such a calibration is unavoidable. I decided to study the impact of the different dark energy models introduced in Chap. 3 on the angular SZ power spectra. The work is presented in this chapter starting with halo approach to the angular SZ power spectrum in Sect. 9.1, followed by a discussion of the choice of the 3D Compton- y radial profile in Sect. 9.2. Afterwards, in Sect. 9.3, I present the predictions for the angular SZ power spectra for various dark energy cosmologies. In Sect. 9.4, an explanation for the predictions of the spectra is given by contrasting the expansion history and structure formation. The chapter closes with a brief listing of the main results and conclusions in the form of a bottom line.

9.1 Computing the SZ angular power spectrum

For the computation of the angular SZ power spectrum, I utilise the halo formalism (Cole & Kaiser 1988; Cooray 2000; Molnar & Birkinshaw 2000; Holder & Carlstrom 2001; Komatsu & Kitayama 1999; Komatsu & Seljak 2002). Galaxy clusters being on arcminute scales will contribute strongest to the angular power spectra on small scales, corresponding to large ℓ 's. Thus, one can assume that for $\ell > 300$, the one-halo Poisson term dominates C_ℓ and therefore the halo-halo correlation term can be neglected. One is left for the C_ℓ with the following relation.

$$C_\ell = g_v^2 \int_0^{z_{\max}} dz \frac{dV}{dz} \int_{M_{\min}}^{M_{\max}} dM \frac{dn(M, z)}{dM} |\tilde{y}_\ell(M, z)|^2, \quad (9.1)$$

Chapter 9. SZ power spectra in dark energy cosmologies

where the spectral function of the SZ effect g_ν is -2 in the Rayleigh-Jeans limit (Sunyaev & Zeldovich 1980), $V(z)$ is the comoving volume of the Universe at z per steradian, $dn(M, z)/dM$ is the comoving dark matter halo mass function from Eq. 2.11, and $\tilde{y}_\ell(M, z)$ stands for the 2D Fourier transform of the projected Compton- y parameter from Eq. 2.24.

It has been shown by Komatsu & Seljak (2002) that for the upper redshift integration limit $z_{\max} = 10$ and that the mass integration limits $M_{\min} = 5 \times 10^{11} M_\odot h^{-1}$ and $M_{\max} = 5 \times 10^{15} M_\odot h^{-1}$ are sufficient to ensure convergence. I adopt those values for what comes after.

The 2D Fourier transform of the projected Compton y -parameter, $\tilde{y}_\ell = \tilde{y}_\ell(M, z)$, needed in Eq. 9.1 is given by

$$\tilde{y}_\ell = \frac{4\pi r_s}{\ell_s^2} \int_0^\infty dx x^2 y_{3D}(x) \frac{\sin(\ell x/\ell_s)}{\ell x/\ell_s}. \quad (9.2)$$

Here $y_{3D}(x)$ stands for the 3D radial profile of the Compton y -parameter and $x \equiv r/r_s$, as a scaled radius, where r_s denotes the scale radius of the 3D radial profile. The corresponding angular wave number ℓ_s is defined as $\ell_s \equiv D_A/r_s$. The choice of the 3D radial profile is discussed in the following section.

9.2 Choice of the 3D Compton- y radial profile

The 3D Compton- y radial profile utilised in this work is the one used by Komatsu & Seljak (2002) that reads

$$y_{3D}(x) \equiv \frac{\sigma_T}{m_e c^2} P_e(x) = \frac{\sigma_T}{m_e c^2} \left(\frac{2 + 2X}{3 + 5X} \right) P_{\text{gas}}(x), \quad (9.3)$$

where $P_e(x)$ is an electron-pressure profile, $X = 0.76$ the primordial hydrogen abundance. It is not based on the β -profile discussed in Subsect. 5.3, but on a general gas pressure profile based on the assumptions of:

1. Hydrostatic equilibrium between the gas pressure and the dark matter potential, where a universal dark matter density profile is assumed.
2. The gas density traces the dark matter density in the out parts of the halo.
3. A constant polytropic equation-of-state $P_{\text{gas}} \propto \rho_{\text{gas}}$.

The argument in favour of a general gas pressure profile with respect to the β -profile is that the latter does not reproduce the simulation results in the outer parts of the haloes. Simulations have shown that the gas profiles in the outer regions of the haloes, asymptotically scale, similar to the dark matter profiles, as r^{-3} , whereas the β -profiles with $\beta = 2/3$ scale as r^{-2} . Thus, the β -profiles are significantly shallower in the outer parts compared to simulations giving rise to the concern that

9.3. Predictions for the angular SZ power spectra in DE cosmologies

this could cause significant errors in the predictions. The reason for this is that the SZ effect is more sensitive to the outer parts to the haloes, since it scales $\propto \rho_{\text{gas}}$, compared to e.g. X-rays, scaling $\propto \rho_{\text{gas}}^2$. For details on exact implementation of the general gas pressure profile, the reader is again referred to Komatsu & Seljak (2002).

9.3 Predictions for the angular SZ power spectra in DE cosmologies

The prediction for the angular SZ power spectra is obtained by integrating Eq. 9.1 for the considered dark energy models. For this work, I selected a representative number of models from the selection introduced in Chap. 3. In total, I selected seven models from Chap. 3, namely the inverse power-law potential model (INV1), the super gravity model (SUGRA), both, the normal and the generalised Chaplygin gas, the topological defect model with $w = -2/3$, the phantom model with $w = -3$ and, as reference model, the fiducial Λ CDM cosmology. The parameter values of the different models can be read off from Tab. 3.2 and the evolution of the equation-of-state parameter w with scale factor a is for quick reference shown in Fig. 9.1. For the calculations the individual δ_c -values from Chap. 8 are used, such that the cosmologies enter in Eq. 9.1 via the δ_c in the mass function and geometrically via the evolution of the comoving volume and in via the angular diameter distance needed for the angular wave number ℓ_s .

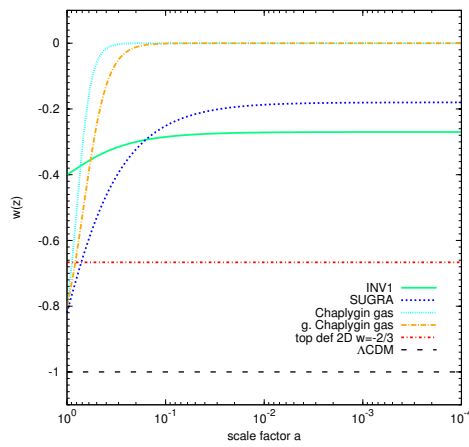


Figure 9.1: Scale factor evolution of the equation-of-state $w(a)$ for the different dark energy cosmologies .

The results of the integration of Eq. 9.1 for the different dark energy models are shown in Fig. 9.2, where the angular power spectra are given for an observing channel of $\nu = 31$ GHz. The differences between the different cosmologies are quite pronounced. Almost all models result in more angular power with respect to the fiducial Λ CDM model, only the phantom model with $w = -3$ exhibits less power. The strongest differences with respect to Λ CDM are found for both Chaplygin gases and the inverse power-law potential (INV1), less pronounced is the increase in angular power for both the SUGRA and the topological defect model. Apart from the differences in the amount of angular power, the spectra also peak for different ℓ 's. From the right panel in Fig. 9.2, where the ratio of the C_ℓ for the

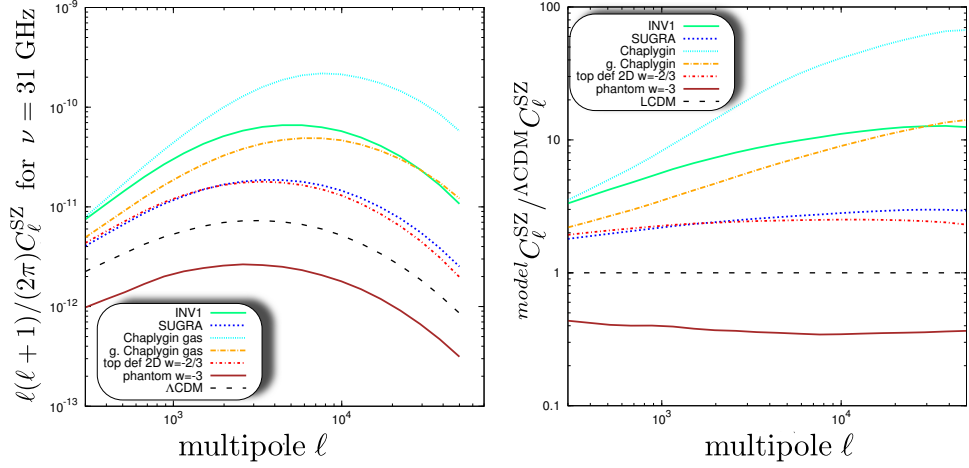


Figure 9.2: SZ power spectra for the different classes of models observed at a frequency of $\nu = 31$ GHz (left panel) and the relative difference with respect to the Λ CDM model (right panel). In both panels, the Λ CDM solution (black, dashed curve) is the reference model. The inverse potential model (INV1) model is shown with the solid green line, the SUGRA model with the blue, short-dashed curve, the (generalised) Chaplygin gas with the (cyan, short-dashed) orange, dot-dashed curve, the topological defect model with $w = -2/3$ by the red, dot-short-dashed line and the phantom model with $w = -3$ by the brown, solid line.

individual dark energy model with the Λ CDM one is shown, one identifies that for the phantom, the SUGRA and the topological defect model the shape of the Λ CDM spectrum is roughly conserved, whereas both Chaplygin gases and the inverse potential model exhibit clearly more power on smaller scales.

In order to study these results in more detail, it is an interesting question to ask which redshifts contribute strongest to the observed angular SZ power spectra. To do so, one can compute the redshift distribution of the C_ℓ 's, which is given by

$$\frac{d \ln C_\ell}{d \ln z} \equiv \frac{z \frac{dV}{dz} \int dM \frac{dn(M,z)}{dM} |\tilde{y}_\ell(M,z)|^2}{\int dz \frac{dV}{dz} \int dM \frac{dn(M,z)}{dM} |\tilde{y}_\ell(M,z)|^2}. \quad (9.4)$$

The result for computing this quantity are depicted in Fig. 9.3. First, one should note that for the Λ CDM case, haloes at $z \sim 1$ contribute strongest to the C_ℓ for multipoles $\ell \sim 3000$ corresponding to an angular scale around 3 arcmin. With respect to the Λ CDM model, the sensitivity for $\ell = 3000$ to haloes at a given redshift is quite different for the various dark energy models. It turns out that, the phantom model is more sensitive to haloes at lower redshift with respect to the Λ CDM model, whereas the other models are all more sensitive to haloes at higher redshifts. The extremest case is the Chaplygin gas which peaks at redshifts of $z \sim 4.3$, followed by the generalised Chaplygin gas and the INV1 model peaking around $z \sim 2.7$ and the SUGRA and topological defect model that reach their maxima

9.4. Expansion history vs. structure formation

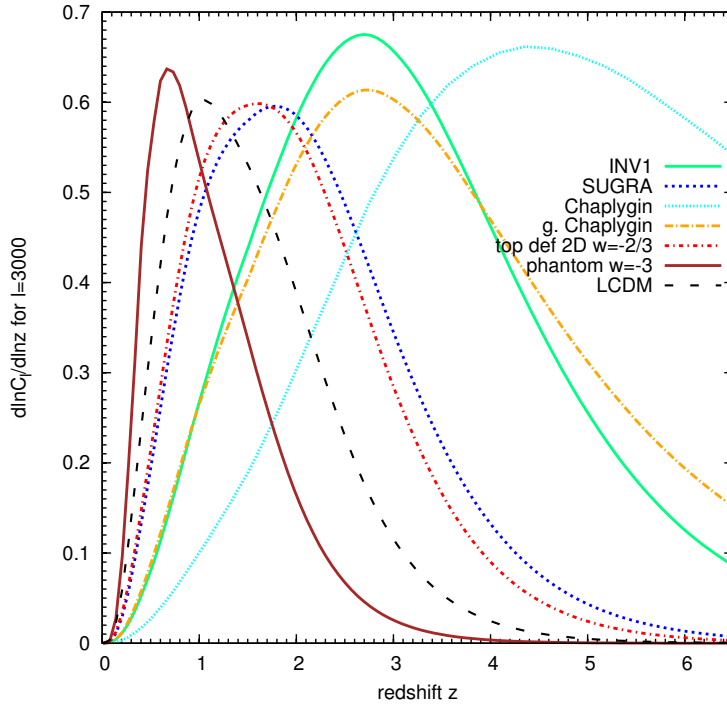


Figure 9.3: Redshift distribution of the C_ℓ 's for the different classes of models. Plotted is $d \ln C_\ell / d \ln z$ from Eq. 9.4 for a fixed given multipole $\ell = 3000$. The black, dashed curve is the Λ CDM reference model. The inverse potential model (INV1) model is shown with the solid green line, the SUGRA model with the blue, short-dashed curve, the (generalised) Chaplygin gas with the (cyan, short-dashed) orange, dot-dashed curve, the topological defect model with $w = -2/3$ by the red, dot-short-dashed line and the phantom model with $w = -3$ by the brown, solid line.

around $z \sim 1.7$. The phantom model peaks around $z \sim 0.6$.

9.4 Expansion history vs. structure formation

When searching for an explanation for the results presented above, one has to ask oneself how the dark energy models enter our calculations. As mentioned before, there are two effects entering the decisive Eq. 9.1. First, we expect differences in the comoving mass function Eq. 2.11, in which the linear density contrast δ_c and the growth factor D_+ enter. Second, there is the expansion function $E(a)$ from Eq. 1.9 entering via the evolution of the comoving volume dV/dz and the angular-diameter distance D_A . From the considerations in Chap. 8 we know that the structure formation is barely altered for the discussed dark energy models, such that the only remaining explanation can come from difference in the expansion history.

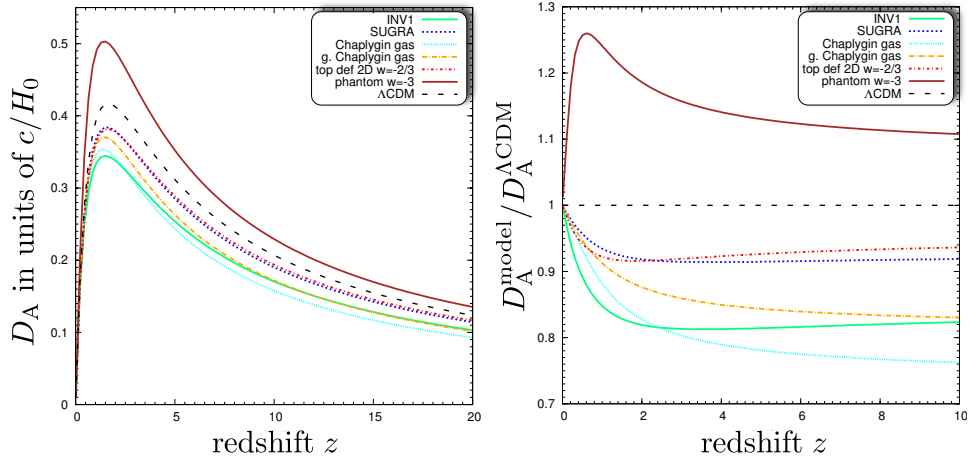


Figure 9.4: Angular diameter distance D_A for the different classes of models in units of c/H_0 (left panel) and the ratio with respect to the Λ CDM model (right panel). In both panels, the Λ CDM solution (black, dashed curve) is the reference model. The inverse potential model (INV1) is shown with the solid, green line, the SUGRA model with the blue, short-dashed curve, the (generalised) Chaplygin gas with the (cyan, short-dashed) orange, dot-dashed curve, the topological defect model with $w = -2/3$ by the red, dot-short-dashed line and the phantom model with $w = -3$ by the brown solid line.

To analyse this in further detail, I computed the redshift evolution of the angular-diameter distance for the different models. The results are compiled in Fig. 9.4, where both the absolute values and the ratio of D_A with respect to Λ CDM are shown. The connection with the results presented in Fig. 9.2 and in Fig. 9.3 are evident. The angular diameter distance anti-correlates with the C_ℓ 's in the sense that the larger angular distance transfers into less angular power and vice versa for the other models. This can be understood by the fact that $dV/dz \propto D_A^2$ and $|\tilde{y}_\ell(M, z)|^2 \propto D_A^{-4}$ and, thus, $C_\ell \propto D_A^{-2}$.

Since, according to the findings from Chap. 8, the structure formation is barely influenced by the various cosmologies, probes in which the expansion history is directly or indirectly measured, like in the current case the angular SZ power spectra, will be of the utmost importance for constraining alternative models.

Bottom line - What to take away

- Due to the lack of need of a calibration between cluster mass and flux and therefore low systematic errors, the angular SZ power spectrum is an interesting cosmological probe.
- Despite only small differences in the linear density contrast δ_c and the growth factor D_+ , different dark energy models exhibit substantial diversities for the angular SZ power spectrum.
- For a fixed multipole ℓ haloes at quite different redshifts dominate the observed signal for the various dark energy models.
- The difference in the spectra can be traced back to the fact that the C_ℓ 's are sensitive to the different expansion history and makes them an interesting probe for constraining alternative models of dark energy.

There is one thing even more vital to science than intelligent methods; and that is, the sincere desire to find out the truth, whatever it may be.

Charles Sanders Peirce
(1839-1914)

10

Conclusions

The progress of modern science proceeds at a mind-boggling speed. In the nineteenth century, it took about fifty years to double the world's knowledge, nowadays this happens on a time scale of a few years. Also cosmology has not been unaffected by this rapid development, such that one could witness in the last three decades the rise of cosmology to become a reputable and quantitative science. Despite the immense achievements in the field, it is still fair to say that we almost know nothing about the Universe. Our standard physical models describe only 5% of the observed energy content in the Universe and we attribute the other 95% to dark components leaving room to wildest speculations. However, the freedom to speculate is, and always was, the impetus for the great scientific discoveries and revolutions of the past. The unknown nature of dark matter and dark energy fascinates societies, providing the foundation to a plethora of observational and theoretical efforts. A very ambitious mission like *PLANCK* has the potential to contribute significantly to improve our understanding of the cosmos but to ensure the final success a vast amount of detailed studies are required, one of which is the PhD thesis at hand. The research that I conducted in the course of my PhD project falls in this broad picture painted above, even though it would compare to blur of colour on the canvas. Yet, I will try summarise the findings and contributions to the field by following a logic thread.

Starting from the main objective to assess the capabilities of the *PLANCK* mission to distinguish between alternative cosmological models by means of a SZ cluster survey, the path of research was self-evident. Having the cosmological models at hand, it was required to develop a fast and versatile semi-analytic method for creating full-sky Compton- γ maps. The method developed in the course of this work can be utilised for all cosmological models that can be described by a time dependent equation-of-state. Furthermore, the clusters are spatially distributed on the sky taking the angular correlation function into account. This was achieved by utilising a line-of-sight integrated approach converting, by means of Limber's approximation, the three dimensional power spectrum to an angular one. Due to its computational speed, our map making algorithm allows to probe quickly a large parameter space of cosmological models without having to rely on costly numerical simulations. The final Compton- γ map can be directly fed into the *PLANCK*

Chapter 10. Conclusions

LevelS pipeline for simulating realistic observations, taking a number of different astrophysical foregrounds as well as the instrumental properties like detector noise, scanning strategy and instrumental beams into account.

The assessment of the expected *PLANCK* SZ cluster sample was a natural continuation after the development of a fast Compton- γ map-making method, also in view of the very optimistic estimations of the anticipated cluster yields. The main part of this work has been done for the *PLANCK* Cluster Challenge (PCC), with the main objective of testing and characterising cluster detection method. To do so, I implemented a filtering and cluster detection pipeline based in the spherical multi-frequency matched filtering (sMFMF) introduced by Schäfer et al. (2006b), a method working fast and on the full-sky. For identifying the clusters in the filtered maps, the `clustFind_cxx` module has been developed, providing a fast, reliable and versatile method for finding peaks in the S/N maps. The detection pipeline was applied to a collection of individually co-added maps, resulting in the conclusion that the synchrotron and free-free emission only mildly affect the filter performance, whereas dust emission as well as source emission in radio and infrared cause a significant drop in size and quality of the detected sample.

In agreement with the findings for other detection methods utilised in the framework of the PCC, I could show that, instead of the previously anticipated $\sim 10^4$ galaxy clusters, a realistic number of detections will be in the range about ~ 1000 clusters. This rather small number of detected SZ clusters will substantially limit the impact of *PLANCK*'s SZ survey on cosmological studies.

Scientific theses are always subject to constant revision, like e.g. erroneous enhancement of structure formation in the presence of early dark energy, that was the initial hypothesis of my studies on *PLANCK*'s SZ cluster sample. Yet, they stimulate scientific progress, as in this case my research was turned in collaboration with Francesco Pace towards the more fundamental study of the spherical collapse in dark energy cosmologies. Following the hydrodynamical approach, we derived the non-linear evolution equation, generalising the evolution equation to a generic collapse geometry, rendering the spherical and ellipsoidal models special cases. Moreover, the newly obtained generality of the method would allow also possible application to modified-gravity cosmologies and coupled-quintessence models. Solving the linear and non-linear evolution equations for a variety of dark energy models, we found that, irrespective of the equation-of-state parameter of the considered cosmologies, the collapse parameters δ_c and Δ_V are very close to the Λ CDM case and therefore structure formation is almost unchanged.

Nevertheless, the different expansion history and therefore different evolution lead to differences in the actual number of objects counted in a volume. Inspired by this, I decided to compute the angular SZ power spectra for a collection of the already studied dark energy models. I found that the different expansion history leaves its fingerprints also in the power spectra. The differences and redshift sensitivity of the spectra between the different models is quite substantial, giving rise to the cognition of SZ power spectra being a promising tool for constraining alternative

cosmologies.

The conclusion that can be drawn from my work are: first, that current SZ surveys face severe challenges to achieve their anticipated cluster yields but, nevertheless, SZ surveys will become with the advance of technology a vital tool in cosmology. Second, structure formation itself is rather insensitive to models with varying equation-of-state, so that probes of the expansion history seem to be the better choice for constraining alternative dark energy models.

Science is a series of judgments, revised without ceasing.

Pierre Emile Duclaux
(1840-1904)



Studying the SZ cluster sample for a hypothetical EDE cosmology

A quite substantial part of this work was addressed to study the impact of early dark energy (see Subsect. 3.2.3) on *PLANCK*'s SZ cluster sample and its possible detectability. The foundation of this work were the results reported in Bartelmann et al. (2006), claiming that the presence of early dark energy lowers the linear density contrast δ_c at low redshifts. Therefore, at the high mass end, a significant enhancement of the number of clusters at redshifts $z \sim 1$ could be expected. From a present point of view, the structures “decayed“ much slower towards the past than for the Λ CDM case. These findings were however disputed by the works of Francis et al. (2009a,b) and Grossi & Springel (2009). The issue was finally resolved by Pace et al. (2010), arriving at the conclusion that the low- δ_c estimates were wrong. Thus, I will discuss the results of my work, from the point of view of a hypothetical “early dark energy” cosmology exhibiting the aforementioned low- δ_c behaviour.

A.1 Studying the impact on *PLANCK*'s cluster sample

Starting point for our study is the map-making method discussed in Chap. 5, by means of which we created four full-sky Compton- y maps; three for the EDE 2, 3 and 4 models (for the parameters see Tab. 3.3) and one for the fiducial Λ CDM cosmology. The maps contain a cluster sample with masses ranging between $10^{13} h^{-1} M_\odot$ and a few times $10^{15} h^{-1} M_\odot$ out to redshifts of $z_{\max} = 3.0$. In order to speed up the computation, the angular cluster correlations have been taken into account for systems with $M_{\text{cl}} \geq 1.5 \times 10^{14} h^{-1} M_\odot$, such that we assume a homogeneous and isotropic SZ background. This threshold has been chosen in order to ensure numerical feasibility, as well as minimising the effect on the detected cluster sam-

Table A.1: Properties of the simulated maps. N_{corr} is the number of correlated clusters and N_{tot} is the total number of simulated systems.

map	N_{corr}	N_{tot}
Λ CDM	1.02×10^5	3.58×10^7
EDE 2	3.08×10^5	5.68×10^7
EDE 3	2.46×10^5	5.02×10^7
EDE 4	4.10×10^5	6.21×10^7

Appendix A. Studying the SZ cluster sample for a hypothetical cosmology

ple. Varying the threshold actually showed that the statistical impact on the detected cluster sample for our filter method is negligible. Depending on the model, the maps comprise in total more than sixty million galaxy clusters as summarised in Table A.1, ensuring a sufficient treatment of the SZ-background due to unresolved clusters. We fed these maps into our observation and filtering pipelines for the clean case, where we just added the CMB and instrumental noise to the maps, dubbed hereafter the CTN case, and for the CTNSDF case, where we added also the Galactic foregrounds.

Assuming a survey threshold of $Y_{\text{threshold}} = 2 \times 10^{-4} \text{ arcmin}^2$, corresponding to a limiting mass $M_{\text{min}} = 3.5 \times 10^{14} h^{-1} M_{\odot}$ at $z = 1.0$, and an association radius of $r_{\text{search}} = 30 \text{ arcmin}$, we cross-check against the input cluster catalogues of our Compton- y maps and obtain in this way cluster catalogues that are free of false detections. In this sense, we assume a *PLANCK* cluster catalogue comprising only confirmed detections, where the validity and redshift of each detection stem from follow-up observations. Moreover, our study does not aim to recover individual cluster properties, like mass or the integrated Comptonisation, but to exploit the effect on the detected number counts.

The first step is to look at the distribution of the number of detections in bins of S/N, as shown in Fig. A.1, which is the information directly obtained from the filtering process. For the clean CTN case (upper row) as well as for the CTNSDF case (lower row), the curves in Fig. A.1 look as expected, in the sense that the number of detections is a decreasing function of the S/N. However, the deviations between the Λ CDM case and the EDE cases are evident. For S/N above 5σ the number of detections is much higher (up to 100% and more) in some bins, and overall the distribution falls off flatter with the S/N. This result is not surprising since we expect in EDE cosmologies a higher abundance of massive systems in the past and these systems are quite likely giving rise to higher S/N. However, when having a closer look on the EDE 3 CTNSDF case in Fig. A.1, it is obvious that for this case the difference is less pronounced and can hardly be distinguished from the Λ CDM case.

After the assumed redshift determination by follow-up observations, it is also possible to study the distribution of detected systems in redshift bins. The results for a redshift bin size of $\Delta z = 0.05$ are shown in Fig. A.2, again for all models, and the CTN as well as the CTNSDF datasets. In the redshift range $0 < z < 0.6$, the increase in number of detections for EDE relative to Λ CDM is quite pronounced for the clean case and also for the EDE 2 and 4 CTNSDF datasets, whereas the EDE 3 CTNSDF case is indistinguishable from a Λ CDM model in terms of the redshift distribution. As expected, the strongest detectability is found for the limiting EDE 4 case, resulting in a boosted number of detections up to $z \sim 1$. When taking the values of $\bar{\Omega}_{\text{DE,sf}}$ from Table 3.3 into consideration, one can argue that with the used detection procedure EDE models having around 4% of $\bar{\Omega}_{\text{DE,sf}}$ should be detectable.

In addition to the number counts, EDE has an effect on the contamination (see

A.1. Studying the impact on PLANCK's cluster sample

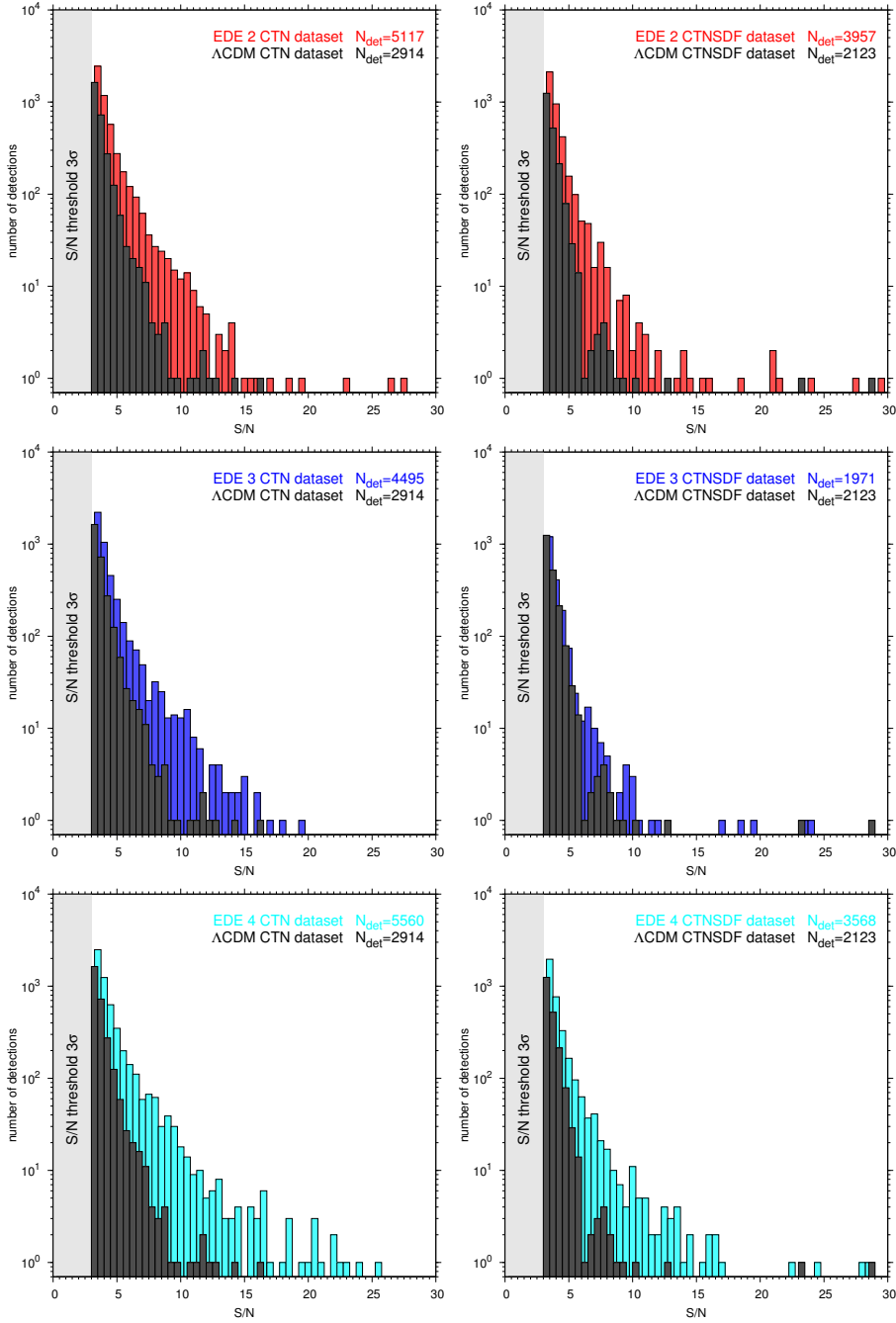


Figure A.1: Number of confirmed detections in bins of S/N of width $\Delta_{S/N} = 0.5$ for $Y_{\text{threshold}} = 2 \times 10^{-4} \text{ arcmin}^2$ and an association radius of $r_{\text{search}} = 30 \text{ arcmin}$ for the EDE 2, EDE 3 and EDE 4 models from top to bottom. The left column shows the clean datasets (CTN) and the right one the foreground contaminated datasets (CTNSDF). For comparison also the Λ CDM case is also shown in each plot. The grey strip on the left indicates the filtering detection threshold of 3σ .

Appendix A. Studying the SZ cluster sample for a hypothetical cosmology

Table A.2: Properties of the detected cluster sample for $Y_{\text{threshold}} = 2 \times 10^{-4} \text{ arcmin}^2$ and an association radius of $r_{\text{search}} = 30 \text{ arcmin}$, N_{det} is number of detections clusters and N_{true} are the true ones.

cosmology	map-type	N_{det}	N_{true}	contamination [%]
Λ CDM	CTN	4221	2914	30.96
EDE 2	CTN	5272	5117	2.94
EDE 3	CTN	4796	4495	6.28
EDE 4	CTN	5651	5560	1.61
Λ CDM	CTNSDF	3389	2123	37.36
EDE 2	CTNSDF	4124	3957	4.05
EDE 3	CTNSDF	2142	1971	8.41
EDE 4	CTNSDF	3680	3568	3.04

Eq. 7.16) of the detected cluster sample. The values for all four set-ups can be found in Table A.2, from which it is evident that all EDE catalogues are significantly less contaminated than the Λ CDM case. Such an effect can be explained by the impact of the relative noise levels for the Λ CDM and EDE cases, such that for the EDE case one has more significantly detectable clusters relative to the uniform background than for Λ CDM. This effect can also be mimicked by downscaling the noise as shown in the appendix. In this sense EDE helps its own detectability not only by increasing the number counts, but also by improving the purity of the detected cluster sample.

It was believed that early dark energy models offer an explanation for the excess in angular power at high multipoles, as discussed by Sadeh et al. (2007). To show that this is also the case for our choice of models we calculated the SZ power spectra following the approach as discussed, for example, by Cooray (2000), Komatsu & Seljak (2002) and Refregier & Teyssier (2002). In order to be comparable to Sadeh et al. (2007) we show in Fig. A.3 the SZ power spectra at an observing frequency of $\nu = 31 \text{ GHz}$ and the redshift distribution of C_ℓ . As expected for the power spectra, all EDE models lie above our fiducial Λ CDM cosmology and for the EDE4 model the boost in power is strongest, despite having the lowest $\sigma_8 = 0.655$, showing that EDE could in principle have offered an explanation to excess power at high multipoles. The redshift distribution of the C_ℓ clearly shows an enhancement in the high redshift tail, since EDE contributes the most at higher redshifts. Even though the current observational status does not allow the models to be distinguished and the nature of the excess is still unclear, future high quality measurements of the SZ power spectra will be a powerful tool for confirming, or ruling out, deviations from the Λ CDM model.

A.1. Studying the impact on PLANCK's cluster sample

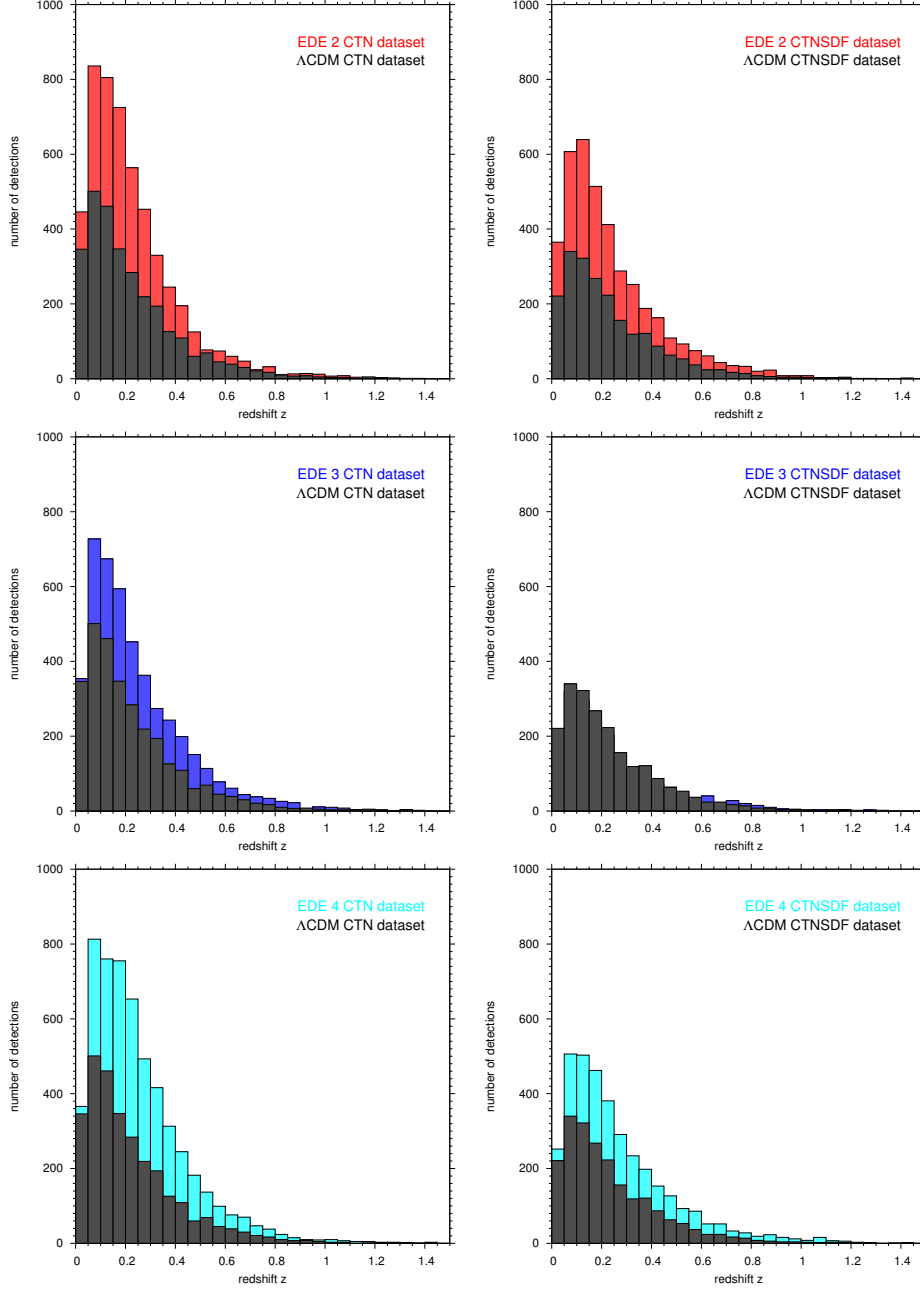


Figure A.2: Number of detections in redshift bins of width $\Delta z = 0.05$ for $Y_{\text{threshold}} = 2 \times 10^{-4} \text{ arcmin}^2$ and an association radius of $r_{\text{search}} = 30 \text{ arcmin}$ comprising the EDE 2, EDE 3 and EDE 4 models from top to bottom for the clean case (CTN) in the left column and for the Galactic foreground dataset (CTNSDF) in the right one. To ease comparison, the Λ CDM case is also shown in each plot as well.

Appendix A. Studying the SZ cluster sample for a hypothetical cosmology

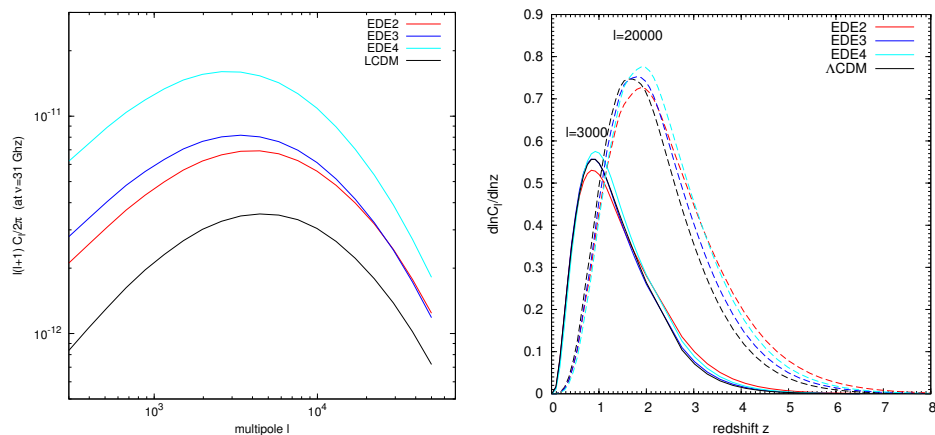


Figure A.3: SZ angular power spectra at $\nu = 31$ GHz (left panel) and redshift distribution of C_ℓ (right panel), plotted as $d \ln C_\ell / d \ln z$ for $\ell = 3000, 20000$, for the EDE2, EDE3 and EDE4 as well as the fiducial Λ CDM model.

A.2 Impact of noise levels to the filter performance

In order to study the surprising results in terms of the contamination of the detected cluster sample, we decided to perform a toy model test by downscaling the level of the CMB, which acts as source of noise to the filtering process. We applied in this case more strict association criteria of $Y_{\text{threshold}} = 3 \times 10^{-4} \text{ arcmin}^2$ and $r_{\text{search}} = 15 \text{ arcmin}$ and included also the completeness, defined as the ratio of N_{true} over the number of cluster in the map above $Y_{\text{threshold}}$, in our analysis (denoted by the green bars in Fig. A.4). By downscaling the CMB, one can mimic the effect of the relative noise level on the properties of the detected cluster sample. The results of this test are shown in Fig. A.4, where it can be seen that the contamination is decreasing with the decreasing noise level. The corresponding contaminations for the EDE 2, 3 and 4 models are illustrated by the solid lines and it can be seen that the levels of the EDE cosmologies can be reached by a relative lowering of the noise level. Hence, the presence of EDE does not only decrease the number of detectable clusters, but it also lowers the contamination by increasing the relative noise ratio between the background and the enhanced low and intermediate redshift cluster sample.

A.3 Constraining EDE parameters with cluster counts

A.3.1 Fisher analysis

The ability of cluster surveys to constrain cosmological parameters via number counts has been studied by many authors (Haiman et al. 2001; Holder et al. 2001; Majumdar & Mohr 2003, 2004; Schäfer & Koyama 2008). Assuming that the number counts in bins can be modelled as independent Poisson processes, one

A.3. Constraining EDE parameters with cluster counts

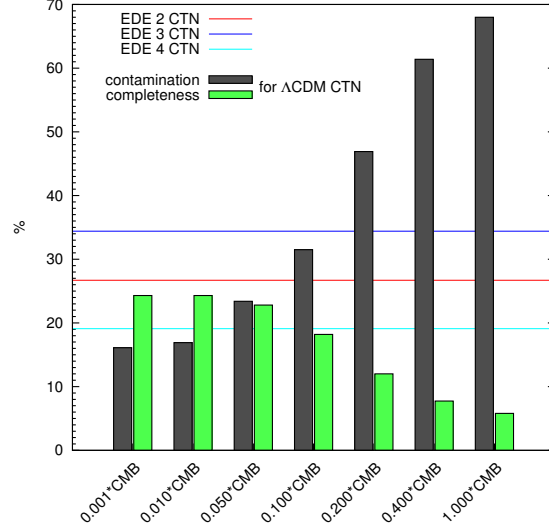


Figure A.4: Contamination (grey bars) and completeness (green bars) for the Λ CDM CTN dataset as function of the scaled CMB for a $Y_{\text{threshold}} = 3 \times 10^{-4}$ arcmin² and $r_{\text{search}} = 15$ arcmin. The solid lines show the according contamination levels for the CTN case of the models EDE 2, 3 and 4.

obtains for the likelihood (Cash 1979)

$$\ln \mathcal{L} = \sum_{\mu=1}^N n_{\mu} \ln e_{\mu} - e_{\mu} - \ln n_{\mu}!, \quad (\text{A.1})$$

where e_{μ} is the expected number of clusters in bin μ and n_{μ} is the actually observed one. Using the definition of the Fisher information matrix one arrives at the following simple relation (Holder et al. 2001)

$$\mathcal{F}_{ij} = \left\langle -\frac{\partial^2 \ln \mathcal{L}}{\partial p_i \partial p_j} \right\rangle = \sum_{\mu=1}^N \frac{\partial e_{\mu}}{\partial p_i} \frac{1}{e_{\mu}} \frac{\partial e_{\mu}}{\partial p_j}, \quad (\text{A.2})$$

being valid for the case of a Gaussian likelihood and statistically independent number counts in the individual redshift bins μ . The joint accuracy for determining a single parameter can be obtained by applying the Cramér-Rao inequality

$$\sigma_i \geq \sqrt{(\mathcal{F}^{-1})_{ii}}. \quad (\text{A.3})$$

The χ^2 for a pair of parameters can be computed by

$$\chi^2 = \begin{pmatrix} \Delta p_i \\ \Delta p_j \end{pmatrix}^t \underbrace{\begin{pmatrix} (\mathcal{F}^{-1})_{ii} & (\mathcal{F}^{-1})_{ij} \\ (\mathcal{F}^{-1})_{ji} & (\mathcal{F}^{-1})_{jj} \end{pmatrix}}_{:=\mathcal{S}_{ij}}^{-1} \begin{pmatrix} \Delta p_i \\ \Delta p_j \end{pmatrix}, \quad (\text{A.4})$$

Appendix A. Studying the SZ cluster sample for a hypothetical cosmology

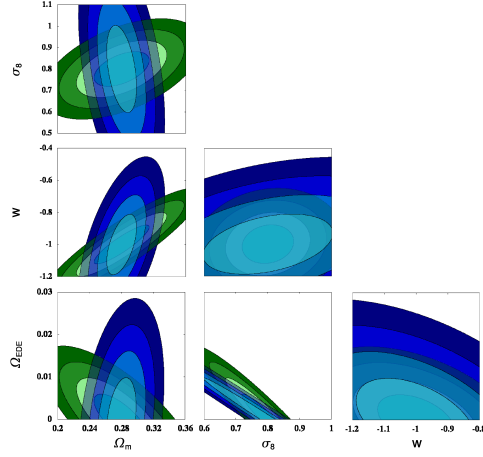


Figure A.5: Forecasts for the parameter degeneracies from a Fisher analysis for the *PLANCK* mission (blue), assuming a limiting flux $F_{\text{lim}} = 100$ mJy and for the SPT mission (green) for $F_{\text{lim}} = 10$ mJy. The ellipses show the 1, 2, 3 and 4 σ thresholds.

where $\Delta p_i = p_i - p_i^{\Lambda\text{CDM}}$ is the difference between the selected and the fiducial parameter value. In order to study the degeneracies, it is necessary to plot the error ellipses, which can be done by calculating the eigenvalues $s_{1,2}$ and the eigenvectors of \mathcal{S}_{ij} . Both quantities determine uniquely the ellipticity and orientation of the ellipses. Under the assumption of a Gaussian likelihood, we can identify the isoprobability contours with constant χ^2 values at

$$\Delta\chi^2 = -2\ln \text{erfc}\left(\frac{n}{\sqrt{2}}\right), \quad (\text{A.5})$$

as the $n\sigma$ confidence intervals. The length of the semi-axes are then given by

$$d_{1,2} = \sqrt{\frac{\Delta\chi^2}{s_{1,2}}} \quad (\text{A.6})$$

and the orientation is determined by the eigenvectors.

A.3.2 Results

The study of the parameter degeneracies from different surveys, as it is shown in Fig. A.5, A.6 and A.7, became obsolete, due to erroneous early dark energy predictions. In the following, I just briefly summarise the used survey parameters. For the standard ΛCDM cosmology the reader is referred to the references in the beginning of Subsect. A.3.1. In order to apply the Fisher analysis as outlined in the previous subsection, it is necessary to assume flux thresholds for the different surveys. For *PLANCK* we assume $S_{\text{lim}}^{\text{SZ}} = 100\text{mJy}$ and for SPT $S_{\text{lim}}^{\text{SZ}} = 10\text{mJy}$. When comparing to *eROSITA* we use a less conservative value of $S_{\text{lim}}^{\text{SZ}} = 5\text{mJy}$. For *eROSITA* we

A.3. Constraining EDE parameters with cluster counts

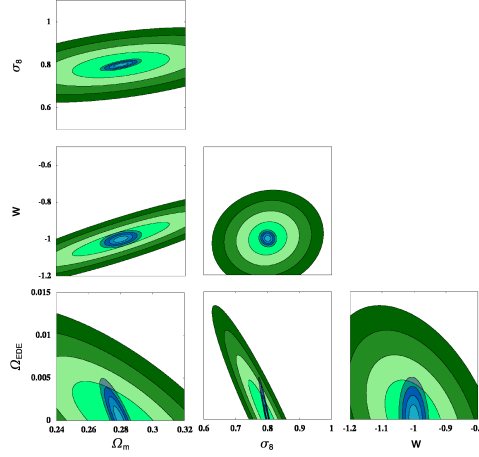


Figure A.6: Forecasts for the parameter degeneracies from a Fisher analysis for the SPT mission (green, assuming $F_{\text{lim}} = 5 \text{ mJy}$), and for the eROSITA all-sky survey (blue), being flux-limited by $F_{\text{lim}} = 1.6 \times 10^{-13} \text{ erg s}^{-1} \text{ cm}^{-2}$ in the $0.5 - 5 \text{ keV}$ range. The ellipses show the 1, 2, 3 and 4σ thresholds.

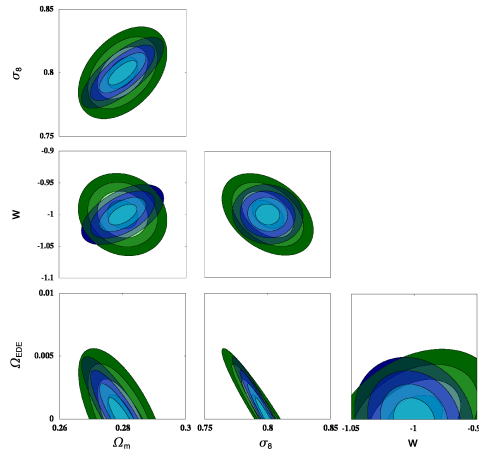


Figure A.7: Forecasts for the parameter degeneracies from a Fisher analysis for two planned eROSITA surveys, the wide survey (green) and the all-sky survey (blue). The surveys are assumed to be flux-limited in the $0.5 - 5 \text{ keV}$ range by $F_{\text{lim}} = 3.3 \times 10^{-14} \text{ erg s}^{-1} \text{ cm}^{-2}$ and $F_{\text{lim}} = 1.3 \times 10^{-13} \text{ erg s}^{-1} \text{ cm}^{-2}$, respectively. The ellipses show the 1, 2, 3 and 4σ thresholds.

Appendix A. Studying the SZ cluster sample for a hypothetical cosmology

included the all-sky and the wide survey having flux limits of we use thresholds of $S_{\text{lim}}^X = 5\text{mJy}$.

What can still be taken away is that by combining cluster surveys of different characteristics, one can in principle significantly narrow down the parameter constraints. It should be mentioned that the performance of *PLANCK* and SPT in terms of the expected cluster yields are overestimated, if one considers the findings of this thesis.

*A journey is best measured in
friends, rather than miles.*

Tim Cahill (1944-)

Acknowledgements

One says that time is relative and indeed it is. The years of my PhD passed quickly and they were never boring, but full of inspiration, insights and loads of fun. With time those years will become the glorious “good old days“ and they will be part of many stories to tell and I will always think back to them with a smile. So I think now the moment is come to thank all the persons that accompanied me on my way in the last years. I learned many things, some related to my work and others not. But since the quality of an introductory address is also measured by its brevity and I think the same applies to written acknowledgements, I think now the moment is come to thank all the persons that accompanied me on my way in the last years.

First, I would like to thank my supervisor, *Prof. Dr. Matthias Bartelmann*, for giving me the opportunity to work with him on the exciting topic of cosmology and for his support on all fields and the freedom to advance as a person. Werner Heisenberg once wrote that science is done by human beings and all I can say is that Matthias is to me a rare, prime example in this respect. Furthermore I would like to thank *Prof. Dr. Luca Amendola* for being the second referee of my thesis, as well as *Björn Malte Schäfer* for sharing his code for the filter construction and the many discussions we had. I would also like to thank *Luigi Iapichino* for all the support on the numerical simulation side and *Georg Robbers*, who provided $w(z)$ and the CMB power spectra for the EDE cosmologies. I'm also grateful to the DFG project *Transregio TR33 The Dark Universe* and to the *IMPRS for Astronomy & Cosmic Physics* at the University of Heidelberg, for supporting my work.

Now it's time for my colleagues, the ones I spent most of my time with in the last years (actually $> 7 \times 10^6$ s) and shared more than just work. Together we went skiing, hiking, climbing (*Matteo, Mischa and Peter*), sailing (*Björn, Peter*), biking (*Björn, Gero, Francesco, Lavinia, Nils and Stefan*), playing loads of table tennis (*Christian, Francesco, Gero, Julian, Matteo, Mischa*), watching movies and often enough we were the last men standing at many occasions (details are confidential...). I can hardly remember a day where we did not laugh about something and had discussions about the weirdest things (*Christian, Emanuel, Gregor, Julian, Mischa*). Also thanks to my office mates *Ana* and *Irina* for the nice working atmosphere (ok, apart from some temperature issues). Un grande grazie va ad *Alessandra, Carlo, Claudia, Federica, Francesco, Luigi, Massimo e Matteo*, la comunità italiana, per avermi "adottato". Ho apprezzato moltissimo la possibilità di iniziare a imparare una nuova lingua, di condividere le serate e le cene con voi e di imparare così tante altre cose da voi. So I would like to thank all of you, the ones I mentioned and the ones I did not, for making the last years such a rich experience.

I also want to use these lines for those with whom I share(d) more than just the office hours and who became close friends of mine. *Federica*, who deliberately tried to teach me Italian and made me laugh so many times, particularly about all

Acknowledgements

these numerous misunderstanding (You like jets? Really?) and you are a fierce competitor in skiing. *Francesco*, a passionate cook, cyclist, teacher of special Italian phrases and a person good at heart, *Lavinia*, with whom I enjoyed uncountable kilometres on the bike and the philosophical discussions and quite some episodes of LOST, and *Massimo*, with whom I shared so much time talking and discussing about everything, from the lack of toilet paper in the Gobi desert to very personal and important stuff, not to forget your memorable and sharp sense of humour.

And then, there is one person for which I lack either the words to express my gratitude or they would be misplaced here: *Eleonora*, you have been such a great support in the last weeks and months and without you my thesis would be different and definitely have more wrong commas. But more importantly you became a part of my life that I will never want to miss.

Besonders danken möchte ich meinen Eltern, *Gisela* und *Gerd Waizmann*, die mich stets mit Verständnis und voller Liebe in allem unterstützt haben und damit die hier vorliegende Arbeit erst ermöglicht haben.

Thanks to all of you!

Bibliography

- Abell, G. O. 1958, *ApJS*, 3, 211
- Abell, G. O., Corwin, Jr., H. G., & Olowin, R. P. 1989, *ApJS*, 70, 1
- Abramo, L. R., Batista, R. C., Liberato, L., & Rosenfeld, R. 2007, *Journal of Cosmology and Astro-Particle Physics*, 11, 12
- Abramo, L. R., Batista, R. C., Liberato, L., & Rosenfeld, R. 2008, *Phys. Rev. D*, 77, 067301
- Abramo, L. R., Batista, R. C., Liberato, L., & Rosenfeld, R. 2009, *Phys. Rev. D*, 79, 023516
- Aghanim, N., de Luca, A., Bouchet, F. R., Gispert, R., & Puget, J. L. 1997, *A&A*, 325, 9
- Albrecht, A. & Skordis, C. 2000, *Physical Review Letters*, 84, 2076
- Alpher, R. A. & Herman, R. C. 1948, *Phys. Rev.*, 74, 1737
- Ashdown, M. A. J., Baccigalupi, C., Balbi, A., et al. 2007, *A&A*, 467, 761
- Bardeen, J. M., Bond, J. R., Kaiser, N., & Szalay, A. S. 1986, *ApJ*, 304, 15
- Barreiro, T., Copeland, E. J., & Nunes, N. J. 2000, *Phys. Rev. D*, 61, 127301
- Bartelmann, M. 2001, *A&A*, 370, 754
- Bartelmann, M. 2003, in *Astronomical Society of the Pacific Conference Series*, Vol. 301, *Astronomical Society of the Pacific Conference Series*, ed. S. Bowyer & C.-Y. Hwang, 255
- Bartelmann, M. 2010, *Reviews of Modern Physics*, 82, 331
- Bartelmann, M., Doran, M., & Wetterich, C. 2006, *A&A*, 454, 27
- Bartelmann, M., Narayan, R., Seitz, S., & Schneider, P. 1996, *ApJL*, 464, L115
- Bartelmann, M. & Schneider, P. 2001, *Physics Reports*, 340, 291
- Bennett, C. L., Hill, R. S., Hinshaw, G., et al. 2003, *ApJS*, 148, 97
- Bernardeau, F. 1994, *ApJ*, 433, 1
- Bond, J. R., Cole, S., Efstathiou, G., & Kaiser, N. 1991, *ApJ*, 379, 440
- Bouchet, F. R. & Gispert, R. 1999, *New Astronomy*, 4, 443
- Bradač, M., Schneider, P., Lombardi, M., & Erben, T. 2005, *A&A*, 437, 39
- Brax, P. H. & Martin, J. 1999, *Physics Letters B*, 468, 40
- Cacciato, M., Bartelmann, M., Meneghetti, M., & Moscardini, L. 2006, *A&A*, 458, 349
- Caldwell, R. R. 2000, *Brazilian Journal of Physics*, 30, 215
- Caldwell, R. R. 2002, *Physics Letters B*, 545, 23
- Cardoso, J., Martin, M., Delabrouille, J., Betoule, M., & Patanchon, G. 2008, *ArXiv e-prints*
- Carlstrom, J. E., Holder, G. P., & Reese, E. D. 2002, *Annu. Rev. Astron. Astr.*, 40, 643

Bibliography

- Carroll, S. M., Press, W. H., & Turner, E. L. 1992, *Annu. Rev. Astron. Astr.*, 30, 499
- Cash, W. 1979, *ApJ*, 228, 939
- Chevallier, M. & Polarski, D. 2001, *International Journal of Modern Physics D*, 10, 213
- Cole, S. & Kaiser, N. 1988, *MNRAS*, 233, 637
- Coles, P. & Lucchin, F. 2002, *Cosmology: The Origin and Evolution of Cosmic Structure*, Second Edition, ed. F. Coles, P. & Lucchin
- Cooray, A. 2000, *Phys. Rev. D*, 62, 103506
- Copeland, E. J., Nunes, N. J., & Rosati, F. 2000, *Phys. Rev. D*, 62, 123503
- Copeland, E. J., Sami, M., & Tsujikawa, S. 2006, *International Journal of Modern Physics D*, 15, 1753
- Corasaniti, P. S. 2004, PhD thesis, University of Sussex
- Corasaniti, P. S. & Copeland, E. J. 2003, *Phys. Rev. D*, 67, 063521
- Cruz, M., Martínez-González, E., Vielva, P., & Cayón, L. 2005, *MNRAS*, 356, 29
- Dicke, R. H., Peebles, P. J. E., Roll, P. G., & Wilkinson, D. T. 1965, *ApJ*, 142, 414
- Doran, M. 2005, *Journal of Cosmology and Astro-Particle Physics*, 10, 11
- Doran, M., Karwan, K., & Wetterich, C. 2005, *Journal of Cosmology and Astro-Particle Physics*, 11, 7
- Doran, M. & Robbers, G. 2006, *Journal of Cosmology and Astro-Particle Physics*, 6, 26
- Doran, M., Robbers, G., & Wetterich, C. 2007, *Phys. Rev. D*, 75, 023003
- Doran, M., Schwindt, J.-M., & Wetterich, C. 2001, *Phys. Rev. D*, 64, 123520
- Durrer, R. 2008, *The Cosmic Microwave Background*, ed. Durrer, R.
- Dyson, F. W., Eddington, A. S., & Davidson, C. 1920, *Royal Society of London Philosophical Transactions Series A*, 220, 291
- Efstathiou, G., Bond, J. R., & White, S. D. M. 1992, *MNRAS*, 258, 1P
- Einstein, A. 1911, *Annalen der Physik*, 340, 898
- Einstein, A. 1916, *Annalen der Physik*, 354, 769
- Einstein, A. 1936, *Science*, 84, 506
- Fabris, J. C., Gonçalves, S. V. B., & de Souza, P. E. 2002, *General Relativity and Gravitation*, 34, 2111
- Fedeli, C. & Bartelmann, M. 2007, *A&A*, 461, 49
- Fedeli, C., Bartelmann, M., Meneghetti, M., & Moscardini, L. 2008, *A&A*, 486, 35

- Fedeli, C., Moscardini, L., & Bartelmann, M. 2009, *A&A*, 500, 667
- Ferreira, P. G. & Joyce, M. 1998, *Phys. Rev. D*, 58, 023503
- Finkbeiner, D. P. 2003, *ApJS*, 146, 407
- Finkbeiner, D. P., Davis, M., & Schlegel, D. J. 1999, *ApJ*, 524, 867
- Finkbeiner, D. P., Davis, M., & Schlegel, D. J. 2000, *ApJ*, 544, 81
- Finoguenov, A., Reiprich, T. H., & Böhringer, H. 2001, *A&A*, 368, 749
- Fixsen, D. J., Cheng, E. S., Gales, J. M., et al. 1996, *ApJ*, 473, 576
- Francis, M. J., Lewis, G. F., & Linder, E. V. 2009a, *MNRAS*, 394, 605
- Francis, M. J., Lewis, G. F., & Linder, E. V. 2009b, *MNRAS*, 393, L31
- Friedmann, A. 1922, *Zeitschrift f. Physik A Hadrons and Nuclei*, 10, 377
- Friedmann, A. 1924, *Zeitschrift f. Physik A Hadrons and Nuclei*, 21, 326
- Gamow, G. 1948, *Phys. Rev.*, 74, 505
- Geisbüsch, J., Kneissl, R., & Hobson, M. 2005, *MNRAS*, 360, 41
- Giardino, G., Banday, A. J., Górski, K. M., et al. 2002, *A&A*, 387, 82
- Godłowski, W. & Szydlowski, M. 2006, *Physics Letters B*, 642, 13
- Górski, K. M., Hivon, E., Banday, A. J., et al. 2005, *ApJ*, 622, 759
- Grossi, M. & Springel, V. 2009, *MNRAS*, 394, 1559
- Haiman, Z., Mohr, J. J., & Holder, G. P. 2001, *ApJ*, 553, 545
- Halliwell, J. J. 1987, *Physics Letters B*, 185, 341
- Harrison, E. R. 1970, *Phys. Rev. D*, 1, 2726
- Haslam, C. G. T., Klein, U., Salter, C. J., et al. 1981, *A&A*, 100, 209
- Haslam, C. G. T., Salter, C. J., Stoffel, H., & Wilson, W. E. 1982, *A&AS*, 47, 1
- Herranz, D., Sanz, J. L., Hobson, M. P., et al. 2002, *MNRAS*, 336, 1057
- Hobson, M. P., Barreiro, R. B., Tofolatti, L., et al. 1999, *MNRAS*, 306, 232
- Hobson, M. P., Jones, A. W., Lasenby, A. N., & Bouchet, F. R. 1998, *MNRAS*, 300, 1
- Hogg, D. W. 1999, *ArXiv Astrophysics e-prints*
- Holder, G., Haiman, Z., & Mohr, J. J. 2001, *ApJL*, 560, L111
- Holder, G. P. & Carlstrom, J. E. 2001, *ApJ*, 558, 515
- Horellou, C. & Berge, J. 2005, *MNRAS*, 360, 1393

Bibliography

- Jenkins, A., Frenk, C. S., White, S. D. M., et al. 2001, *MNRAS*, 321, 372
- Jennings, E., Baugh, C. M., Angulo, R. E., & Pascoli, S. 2010, *MNRAS*, 401, 2181
- Kaiser, N. 1986, *MNRAS*, 222, 323
- Kaiser, N. & Squires, G. 1993, *ApJ*, 404, 441
- Kamenshchik, A., Moschella, U., & Pasquier, V. 2001, *Physics Letters B*, 511, 265
- Kay, S. T., Liddle, A. R., & Thomas, P. A. 2001, *MNRAS*, 325, 835
- Keihänen, E., Keskitalo, R., Kurki-Suonio, H., Poutanen, T., & Sirviö, A. 2010, *A&A*, 510, A57
- Keihänen, E., Kurki-Suonio, H., & Poutanen, T. 2005, *MNRAS*, 360, 390
- Komatsu, E., Dunkley, J., Nolta, M. R., et al. 2009, *ApJS*, 180, 330
- Komatsu, E. & Kitayama, T. 1999, *ApJL*, 526, L1
- Komatsu, E. & Seljak, U. 2002, *MNRAS*, 336, 1256
- Kompaneets, A. S. 1957, *Sov. Phys., JETP*, 4, 730
- Kurki-Suonio, H., Keihänen, E., Keskitalo, R., et al. 2009, *A&A*, 506, 1511
- Lagache, G. & Puget, J. L. 2000, *A&A*, 355, 17
- Land, K. & Magueijo, J. 2005, *Physical Review Letters*, 95, 071301
- Leach, S. M., Cardoso, J., Baccigalupi, C., et al. 2008, *A&A*, 491, 597
- Lemaître, G. 1927, *Annales de la Société Scientifique de Bruxelles*, A47, 49
- Lewis, A., Challinor, A., & Lasenby, A. 2000, *ApJ*, 538, 473
- Lima, J. A. S., Zanchin, V., & Brandenberger, R. 1997, *MNRAS*, 291, L1
- Limber, D. N. 1953, *ApJ*, 117, 134
- Linder, E. V. 2003, *Physical Review Letters*, 90, 091301
- Linder, E. V. 2008, *General Relativity and Gravitation*, 40, 329
- Linder, E. V. & Jenkins, A. 2003, *MNRAS*, 346, 573
- Maino, D., Burigana, C., Górski, K. M., Mandolesi, N., & Bersanelli, M. 2002, *A&A*, 387, 356
- Majumdar, S. & Mohr, J. J. 2003, *ApJ*, 585, 603
- Majumdar, S. & Mohr, J. J. 2004, *ApJ*, 613, 41
- Maor, I. & Lahav, O. 2005, *Journal of Cosmology and Astro-Particle Physics*, 7, 3
- Mather, J. C., Cheng, E. S., Eplee, Jr., R. E., et al. 1990, *ApJL*, 354, L37

- Melin, J., Bartlett, J. G., & Delabrouille, J. 2006, *A&A*, 459, 341
- Merten, J., Cacciato, M., Meneghetti, M., Mignone, C., & Bartelmann, M. 2009, *A&A*, 500, 681
- Meszáros, P. 1974, *A&A*, 37, 225
- Meszáros, P. 1975, *A&A*, 38, 5
- Mo, H. J. & White, S. D. M. 1996, *MNRAS*, 282, 347
- Molnar, S. M. & Birkinshaw, M. 2000, *ApJ*, 537, 542
- Mota, D. F. & van de Bruck, C. 2004, *A&A*, 421, 71
- Narayan, R. & Bartelmann, M. 1996, *ArXiv e-prints*, astro-ph/9606001
- Navarro, J. F., Frenk, C. S., & White, S. D. M. 1996, *ApJ*, 462, 563
- Navarro, J. F., Frenk, C. S., & White, S. D. M. 1997, *ApJ*, 490, 493
- Ogawa, N. 2000, *Phys. Rev. D*, 62, 085023
- Ohta, Y., Kayo, I., & Taruya, A. 2003, *ApJ*, 589, 1
- Ohta, Y., Kayo, I., & Taruya, A. 2004, *ApJ*, 608, 647
- Pace, F., Waizmann, J., & Bartelmann, M. 2010, *MNRAS*, 1011
- Padmanabhan, T. 1996, *Cosmology and Astrophysics through Problems*, ed. T. Padmanabhan
- Peebles, P. J. E. 1980, *The large-scale structure of the universe*, ed. Peebles, P. J. E.
- Peebles, P. J. E. & Yu, J. T. 1970, *ApJ*, 162, 815
- Penzias, A. A. & Wilson, R. W. 1965, *ApJ*, 142, 419
- Perlmutter, S., Aldering, G., Goldhaber, G., & et al. 1999, *ApJ*, 517, 565
- Press, W. H. & Schechter, P. 1974, *ApJ*, 187, 425
- Puget, J., Abergel, A., Bernard, J., et al. 1996, *A&A*, 308, L5
- Ratra, B. & Peebles, P. J. E. 1988, *Phys. Rev. D*, 37, 3406
- Refregier, A. & Teyssier, R. 2002, *Phys. Rev. D*, 66, 043002
- Reinecke, M., Dolag, K., Hell, R., Bartelmann, M., & Enßlin, T. A. 2006, *A&A*, 445, 373
- Riess, A. G., Filippenko, A. V., Challis, P., & et al. 1998, *ApJ*, 116, 1009
- Robertson, H. P. 1935, *ApJ*, 82, 284
- Rosati, P., Borgani, S., & Norman, C. 2002, *Annu. Rev. Astron. Astr.*, 40, 539
- Sachs, R. K. & Wolfe, A. M. 1967, *ApJ*, 147, 73
- Sadeh, S., Rephaeli, Y., & Silk, J. 2007, *MNRAS*, 380, 637
- Sanchez, A. G., Crocce, M., Cabre, A., Baugh, C. M., & Gaztanaga, E. 2009, *ArXiv e-prints*

Bibliography

- Sanderson, A. J. R., Ponman, T. J., Finoguenov, A., Lloyd-Davies, E. J., & Markevitch, M. 2003, *MNRAS*, 340, 989
- Sanz, J. L., Herranz, D., & Martínez-González, E. 2001, *ApJ*, 552, 484
- Sarazin, C. L. 1986, *Reviews of Modern Physics*, 58, 1
- Schäfer, B. M. & Bartelmann, M. 2007, *MNRAS*, 377, 253
- Schäfer, B. M. & Koyama, K. 2008, *MNRAS*, 385, 411
- Schäfer, B. M., Pfrommer, C., Bartelmann, M., Springel, V., & Hernquist, L. 2006a, *MNRAS*, 370, 1309
- Schäfer, B. M., Pfrommer, C., Hell, R. M., & Bartelmann, M. 2006b, *MNRAS*, 370, 1713
- Schlegel, D. J., Finkbeiner, D. P., & Davis, M. 1997, in *Bulletin of the American Astronomical Society*, Vol. 29, *Bulletin of the American Astronomical Society*, 1354
- Schlegel, D. J., Finkbeiner, D. P., & Davis, M. 1998, *ApJ*, 500, 525
- Schwarz, D. J., Starkman, G. D., Huterer, D., & Copi, C. J. 2004, *Physical Review Letters*, 93, 221301
- Sheth, R. K., Mo, H. J., & Tormen, G. 2001, *MNRAS*, 323, 1
- Silk, J. 1968, *ApJ*, 151, 459
- Simon, P. 2007, *A&A*, 473, 711
- Sokasian, A., Gawiser, E., & Smoot, G. F. 2001, *ApJ*, 562, 88
- Springel, V., White, S. D. M., Jenkins, A., et al. 2005, *Nature*, 435, 629
- Steinhardt, P. J., Wang, L., & Zlatev, I. 1999, *Phys. Rev. D*, 59, 123504
- Sugiyama, N. 1995, *ApJS*, 100, 281
- Sunyaev, R. A. & Zeldovich, I. B. 1980, *Annu. Rev. Astron. Astr.*, 18, 537
- Sunyaev, R. A. & Zeldovich, Y. B. 1972, *Comments on Astrophysics and Space Physics*, 4, 173
- Szydlowski, M. & Czaja, W. 2004, *Phys. Rev. D*, 69, 023506
- Szydlowski, M. & Godłowski, W. 2008, *International Journal of Modern Physics D*, 17, 343
- Szydlowski, M., Kurek, A., & Krawiec, A. 2006, *Physics Letters B*, 642, 171
- Tauber, J. A. 2000, *Astrophysical Letters Communications*, 37, 145
- The Planck Collaboration. 2006, *ArXiv Astrophysics e-prints*
- Toffolatti, L., Argüeso Gomez, F., de Zotti, G., et al. 1998, *MNRAS*, 297, 117
- Truemper, J. 1992, *QJRAS*, 33, 165
- Valls-Gabaud, D. 1998, *Publications of the Astronomical Society of Australia*, 15, 111

- Waizmann, J.-C. & Bartelmann, M. 2009, A&A, 493, 859
- Walker, A. G. 1937, Proc. London Math. Soc., s2-42, 90
- Wandelt, B. D., Hivon, E., & Gorski, K. M. 1998, ArXiv Astrophysics e-prints
- Wands, D., Copeland, E. J., & Liddle, A. R. 1993, in New York Academy Sciences Annals, Vol. 688, Texas/PASCOS '92: Relativistic Astrophysics and Particle Cosmology, ed. C. W. Akerlof & M. A. Srednicki, 647
- Wang, L. & Steinhardt, P. J. 1998, ApJ, 508, 483
- Wetterich, C. 1988, Nuclear Physics B, 302, 668
- Wetterich, C. 1995, A&A, 301, 321
- Wetterich, C. 2004, Physics Letters B, 594, 17
- Weymann, R. 1965, Physics of Fluids, 8, 2112
- Weymann, R. 1966, ApJ, 145, 560
- Zeldovich, Y. B. 1972, MNRAS, 160, 1P
- Zwicky, F. 1933, Helvetica Physica Acta, 6, 110
- Zwicky, F. 1937, ApJ, 86, 217

- Abell, George, 22
- accretion, 17
- acoustic oscillations, 14
- AGN, 17, 43, 61
- alm2map, 55
- almmixer, 65
- anafast, 65
- angular
 - correlation function, 56
 - resolution, 41, 57, 62
 - scale, 15
 - size, 7
- anisotropies
 - primary, 14, 43
 - secondary, 14, 43
- antenna temperature, 60, 63
- arc, 23
- arclets, 23
- Aristarchus of Samos, 1
- Asimov, Isaac, 101
- asteroids, 43
- autocorrelation function, 43

- β -profile, 25, 70, 102
- B-modes, 9, 43, 45
- background, 8, 20, 22, 33, 43, 69, 90, 113, 116
- BAOs, 6
- baryonic gas, 23, 28
- beam shapes, *see* PLANCK
- bias, 53, 62, 85
 - effective, 54
- Big Bang, 8, 13
- black-body spectrum, 27
- blazars, 43
- bolometer, 44
- bolometric
 - luminosity, 7
 - volume emissivity, 24
- Boltzmann code, 12, 15
- BOOMERANG, 14
- boresight, 63
- Bremsstrahlung, 21, 23, 24
- bulk flows, 29

- χ^2 , 119
- C++, 55, 75
- calibration, 101, 107
- CAMB, 65
- Casimir effect, 39, 94
- catalogue, 1
 - cluster, 43, 47, 76, 82, 114
 - point source, 43
- caustic, *see* lensing
- central limit theorem, 11
- Chaplygin gas, 38
 - generalised, 39, 96, 103
- characteristic density, 20
- cloud-in-cloud problem, 21
- cluster detection
 - optical, 22
- clustering, 8
- clustFind module, 74, 110
- CMB, 1, 9, 13–16, 26, 27, 29, 35, 51, 52, 57, 64, 70, 114, 118
 - axis of evil, 42
 - cold-spot, 42
 - dipole, 65
 - polarisation, 9, 42
 - restframe, 15
- CMBEASY, 13, 65
- co-added sky maps, 65, 70, 76
- COBE, 14, 45
- coincidence problem, 32
- colour, 22
- comets, 43
- comoving
 - coordinates, 10, 90
 - distance, 7
 - horizon size, 8, 12
 - peculiar velocity, 90
 - radial coordinate, 7
 - volume, 5, 48, 102, 103, 105
 - wavelength, 9
- completeness, 77, 78, 81
- component separation, 69
- Compton scattering, 27, 29
 - inverse, 26

Index

- Compton- γ parameter, 27, 28, 47, 48, 55, 70, 102, 109, 113, 114
- Comptonisation, 28, 50, 53, 75, 77, 83, 114
- confidence intervals, 120
- contamination, 77, 78, 81, 118
- continuity equation, 34, 89–91, 98
- convolution, 65, 70, 74
 - theorem, 71
- core radius, 19, 25, 50
- cosmic
 - history, 35
 - infra-red background, 62
 - microwave background, *see* CMB rays, 43
- cosmo-dynamics, 4
- cosmological
 - constant, 4, 10, 31, 35, 37, 92
 - parameters, 6, 15, 20, 21, 42, 43, 65, 118
 - principle, 3
 - redshift, 4
- Cousteau, Jacques Yves, 1
- Cramer-Rao inequality, 119
- critical density, 6, 39, 48
- cross power spectrum, 71, 73
- curvature, 4, 6, 31
- curvilinear quadrilaterals, 51
- dark energy, 1, 6, 31, 38, 65, 76, 77, 89, 96, 101, 103, 105, 110
 - coupled, 96
 - domination, 34
- dark matter, 1, 10, 21, 32
 - haloes, 17, 18, 20, 62, 81, 96
 - power spectrum, 11
- DE, *see* dark energy
- de-stripping techniques, 64
- Democritus, 1
- density contrast, 10, 11, 20, 53, 55, 93, 105, 113
- density parameters, 6
- density profile, 19–20, 25, 102
 - isothermal, 19
 - NFW, 20
- detection
 - map, 70
 - threshold, 81
- diffraction rings, 63
- dimensionless frequency, 27, 29
- Dirac function, 12
- discretisation, 51
- distance
 - angular-diameter, 7, 103, 105, 106
 - comoving, 7, 54
 - cosmic, 7
 - luminosity, 7
 - measures, 7
 - proper, 7
- Doppler shift, 4
- Dragone-Mizuguchi condition, 44
- Duclaux
 - Pierre Emile, 113
- early dark energy, 2, 33, 36–38, 51, 94, 110, 113, 114, 120
- ecliptic
 - equator, 64
 - poles, 63, 64, 67, 81
- EDE, *see* early dark energy
- eigenvalues, 120
- eigenvectors, 120
- Einstein, Albert, 22
 - de Sitter, 10, 31, 94, 96
 - equations, 4, 9, 90
- ellipsoidal collapse, 89, 92
- energy transfer, 26, 29
- energy-momentum tensor
 - see* tensor, 4
- ensemble average, 71
- equation-of-state, 19, 32, 56, 77, 89
 - parameter, 31, 34, 35, 40, 94, 96, 99, 103, 110
 - polytropic, 102
- Eratosthenes, 1
- ergodicity, 71

-
- eROSITA, 120
error ellipse, 120
Esar, Evan, 31
Euclidean space, 7
Euler equation, 19, 90, 91
expansion
 accelerated, 6, 31, 32, 38, 39
 function, 34, 105
 history, 105, 110
 rate (relative), 5
 time scale, 10
exponential cut-off, 21
exponential potential, 34
extra-solar planets, 1
- far-side lobes, 45, 63
feedback processes, 17, 22
filter
 construction, 70, 81
 kernel, 70
 performance, 2, 70, 76, 110
 scale-adaptive, 74
filtering, 69–74, 118
fine-tuning, 33
Fisher
 analysis, 120
 matrix, 119
fitsio, 64
flatness, 6
flux, 60, 107
 change, 27, 29
 density, 27
 limit, 122
 observed, 7
 threshold, 120
focal
 length, 44
 plane, 43
Fokker-Planck equation, 27
foregrounds, 57–62, 64, 69, 70, 77, 110, 114
 Galactic dust emission, 43, 57, 110
 Galactic free-free emission, 57, 60
 Galactic synchrotron emission, 43, 57
 subtraction, 43
 zodiacal light, 43
Fourier transform, 12, 13, 64, 102
Friedmann, Alexander
 equations, 5
friend-of-friend finder, 75
fundamental
 interactions, 3
 observer, 3
- Galactic magnetic field, 43, 59
galaxies, 1, 8, 19, 21, 23
 elliptical, 22
 infra-red, 43, 61
 radio, 43
 red sequence, 22
 spiral, 22
galaxy clusters, 8, 17–29, 47
 in the microwaves, 26
 in the optical, 22
 observations, 21–29
 population, 21
galaxy formation, 17
Gamov, 13
Gaunt factor, 24, 60
Gaussian, 11, 62
 distribution, 11
 likelihood, 119, 120
 random field, 14
 realisation, 55
 smoothing, 13, 53
 statistic, 70
 units, 61
Gaussianity, 15
 -non, 42
general relativity, 3, 9, 31, 89
 weak field limit, 89
geometrical tests, 100
GRASP8, 63
-

Index

- gravitational
 - instability, 8
 - lensing, 7, 21, 22, 43
 - potential, 15, 17, 23, 89
 - waves, 1, 9, 43
- gravity, 3
- Gregorian system, 43
- growth
 - factor, 10, 96, 97, 105
 - function, 10
 - history, 96
 - linear, 8, 10
 - non-linear, 8
 - of structures, 17
 - suppression, 10, 12
- Haar wavelet transform, 52
- halo, *see* dark matter
 - concentration, 20
 - formalism, 101
- HealPix, 51–52, 55, 64, 65, 74
 - nested scheme, 52
 - ring scheme, 52
- Herschel, William, 21
- HFI, 44, 63
- Hipparch, 1
- homogeneity, 3
- horizon size, 8, 9, 12
- Hubble, Edwin
 - constant, 6
 - flow, 4
 - function, 5, 90
 - parameter, 8
 - time, 26
- hydrogen, 13, 102
 - fraction, 28
- hydrostatic equilibrium, 19, 26, 48, 102
- ICM, 22, 26, 29
- ideal gas, 19
- image, 23
- initial conditions, 33, 92
- instrumental noise, 57, 63–65, 70, 81, 114
- interstellar medium, 59
- intra-cluster medium, *see* ICM
- inverse power-law potential, 33, 103
- isoprobability, 120
- isothermal sphere, 19
- isothermality, 25, 28, 48, 50
- isotropy, 3, 81
- Joule-Thomson refrigerator, 45
- Jung, Carl Gustav, 3
- Kompaneets equation, 27
- Λ CDM cosmology, 31, 47, 51, 89, 94, 96, 97, 103, 106, 113, 114, 120
- L2, 41, 44, 45, 63
- Lagrangian
 - density, 32
 - multiplier, 73
- large-scale structure, 35, 43
- lens model, 23
- lensing, 99
 - caustic, 23
 - CMB, 14, 15, 43, 63
 - strong, 22, 23
- LevelS, 56, 64, 66, 69, 110
- LFI, 44, 63
- light deflection, *see* lensing
- likelihood, 119
- Limber's approximation, 55, 56, 109
- line-of-sight, 25, 27, 51, 54, 56, 109
- magnitude, 22
- map making, 56, 82, 109, 113
- mass function, 20–21, 48, 96, 102, 105
 - Jenkins, 21
 - Press-Schechter, 20, 97
 - Sheth and Tormen, 21
- matter-dominated era, 6, 10, 34
- MAXIMA, 14

- mean molecular weight, 19
 Melville, Herman, 47
 Messier, Charles, 1, 21
 microwaves, 26, 42
 modified-gravity, 92, 98, 110
 multimod, 65
 multipole, 15, 42, 104, 107, 116
 Murrow, Edward R., 41

 $1/f$ -noise, 64
 Newtonian
 hydrodynamics, 89, 100
 theory, 9
 noise
 equivalent power, 63
 temperature, 63
 non-linear mass scale, 21
 number counts, 97, 99, 114, 116, 118
 numerical simulations, 8, 19–21, 47,
 56, 102

 observations, 3
 Oppenheimer, Julius R., 89
 Ostriker-Vishniac effect, 14
 overdensity, 18, 89, 96
 initial, 93
 parameter, 92, 94
 threshold, 96

 paraboloid, 44
 parametrisation, 34
 Parnas, Dave, 17
 Peirce, Charles Sanders, 109
 perfect fluid, 4, 89
 perturbations, 10, 12, 14
 linear, 8
 non-linear, 8
 scalar-type, 9
 tensor-type, 9
 vector-type, 9
 phantom model, 40, 103, 104
 phase space, 27
 pixelisation, 51

 PLANCK, 14, 51, 109, 114, 122
 beam, 62, 65, 110
 high-frequency channel, 43
 mission, 41–45
 pipeline, 55, 63
 scan strategy, 63, 81, 110
 simulations, 57, 69
 thermal design, 45
 Planck, Max, 41
 Planckian spectrum, 13, 27
 Rayleigh-Jeans regime, 27
 Wien regime, 27
 plasma, 23, 60
 point source contamination, 61
 Poisson
 distribution, 48, 55
 equation (relativistic), 90
 process, 118
 statistics, 63
 polarisation, *see* CMB
 power spectrum, 11, 15, 109
 angular, 15, 53, 55, 109
 CMB, 13, 14, 42, 43, 45, 65
 dark matter, 53
 noise, 64, 73
 SZ, 2, 101–103, 106, 110, 116
 pressure, 5, 89, 102
 projection-operator, 90
 proper time, 7
 Ptolemeaeus, 1

 quintessence, 32–38
 coupled, 92, 98, 110

 radial velocity, 18
 radiation-dominated era, 6, 10, 12
 ram-pressure stripping, 17
 redshift, 4, 22, 29, 31, 47
 Rees-Sciama effect, 14, 43
 reionisation, 43
 relativistic fluid, 89
 relaxation processes, 17
 rest-frame, 29

Index

- Ricci
 - scalar, 4, 32
 - tensor, 4
- rms-fluctuations, 63
- Robertson-Walker metric, 4, 32
- ROSAT All-Sky Survey, 88
- rotation curves, 19

- σ_8 , 12, 21, 53, 87, 98, 116
- Sachs-Wolfe effect, 14
 - integrated, 14, 43
- scalar field, 32
 - equation of motion, 32
 - self-interacting, 32
- scale factor, 4, 35, 91, 94
- scale radius, 20, 102
- scaling fields, 33
- Second Lagrangian point, *see* L2
- selection function, 47, 84
- Sherlock, Holmes, 57
- signal-to-noise, 70, 114
 - ratio, 74
- Silk damping, 14, 42
- simmission, 65
- sMFMF, 72, 78, 84, 85, 110
- SNe, *see* supernovae
- solar eclipse, 22
- Solar System, 1, 43, 57
- solid angle, 48, 53
- sorption cooler, 45
- sound horizon, 14
- space time
 - curvature, 9
 - curved, 7
 - homogenous, 4
 - isotropic, 4
 - non-stationary, 7
- spectral
 - break, 59
 - index, 6, 60
 - signature, 27
 - slope, 59
- speed of light, 8

- spherical collapse, 2, 17–19, 35, 38, 89–99, 110
- spherical coordinates, 4, 14
- spherical harmonic, 14, 52, 54, 64, 70
 - coefficients, 15, 55, 65, 71, 73
 - transform, 52
- spherical multi-frequency matched filter, *see* sMFMF
- SPT, 120
- Standard Template Library, *see* STL
- star formation, 22, 62
- statistical information, 15
- STL, 75
- string theory, 38
- structure formation, 7–14, 31, 36, 38, 92, 99, 100, 105, 110
- submillimetric, 62
- SUGRA, 103
- Sunyaev-Zel'dovich effect, 14, 27, 53, 101, 103
 - kinetic, 29
 - thermal, 1, 26, 28, 43, 47, 57, 70, 73, 99
- super-horizon modes, 10
- supergravity, *see* SUGRA
- supernovae, 6, 35, 40
- surface-brightness, 25, 50
- synalm, 55, 65
- SZ, *see* Sunyaev-Zel'dovich effect
- SZ power spectrum, *see* power spectrum

- tensor
 - energy-momentum, 4
 - rotation, 91
 - shear, 91, 92
 - stress-energy, 9, 89, 98
 - symmetric traceless, 91
- tesselation, 51
- Thales of Miletus, 1
- thermal equilibrium, 13, 26
- thermodynamics, 5

-
- Thompson cross section, 27
Thoreau, Henry David, 69
time ordered data, 64
TOD, *see* time ordered data
top-hat, 13, 18, 53
topological defects, 40, 42, 94, 103
topology, 39
totalconvolve, 65
tracker fields, 33
turnaround, 18, 94
- velocity dispersion, 19, 21, 24
virial
 - equilibrium, 17, 18
 - overdensity, 94, 96
 - radius, 18
 - temperature, 18
 - theorem, 19, 48
- volume
 - comoving, 5
 - effects, 96, 97
 - element, 96
 - proper, 5
- wave number, 102, 103
weak field limit, *see* general relativity
white noise, 64, 67
window function, 53, 55
WMAP, 6, 42, 45, 51
- X-rays, 23, 103
 - emission, 23
 - luminosity, 23, 25
 - observations, 21, 25
 - surface brightness, 25
 - survey, 43
- Zwicky, Fritz, 21